



# Synthesis and characterization of avocado pit activated carbon-incorporated chitosan composite beads for harnessing methylene blue adsorption: DFT insights and box-behnken design optimization

Soukaina El Bourachdi <sup>a,\*</sup>, Abdelhay El Amri <sup>b</sup>, Ali Raza Ayub <sup>c</sup>, Fatima Moussaoui <sup>a</sup>, Yassine Rakcho <sup>d,\*</sup>, Faïçal El Ouadrhiri <sup>a</sup>, Abderrazzak Adachi <sup>a</sup>, Taoufiq Bouzid <sup>e</sup>, José Alberto Herrera-Melián <sup>f</sup>, Amal Lahkimi <sup>a</sup>

<sup>a</sup> Laboratory of Engineering, Electrochemistry, Modelling and Environment, Faculty of Sciences Dhar El Mehraz, Sidi Mohamed Ben Abdellah University, Fez, Morocco

<sup>b</sup> Laboratory of Advanced Materials and Process Engineering (LAMPE), Faculty of Sciences, Ibn Tofail University, B.P. 133, 14000 Kenitra, Morocco

<sup>c</sup> Key Laboratory of Clusters Science of Ministry of Education, School of Chemistry and Chemical Engineering, Beijing Institute of Technology, Beijing 100081, China

<sup>d</sup> Laboratory Materials, Processes, Environment and Quality, National School of Applied Sciences, Cadi Ayyad University (UCA), Route Sidi Bouzid BP 63, 46000 Safi, Morocco

<sup>e</sup> Laboratoire de chimie analytique et moléculaire, Université de Cadi Ayyad, faculté polydisciplinaire, Safi, Morocco

<sup>f</sup> University Institute of Environmental Studies and Natural Resources (i-UNAT), Universidad de Las Palmas de Gran Canaria, 35017 Las Palmas de Gran Canaria, Spain

## ARTICLE INFO

### Keywords:

Adsorption  
Avocado pits  
Chitosan@activated carbon  
DFT  
Methylene blue

## ABSTRACT

**Background:** Methylene blue (MB), a toxic dye in industrial wastewater, requires efficient removal methods due to its environmental and health risks. This study uses activated carbon derived from avocado pits, modified with chitosan to form the CS@ACAP composite, to enhance adsorption. The research focuses on optimizing the synthesis, evaluating adsorption efficiency, and exploring the adsorption mechanisms through experimental and theoretical analyses.

**Methods:** Activated carbon was synthesized and optimized using the Box-Behnken design, considering key parameters such as sulfuric acid concentration, activation time, and temperature. The material was then modified with chitosan to create the CS@ACAP composite. Both materials were characterized using FTIR, SEM, XRD, BET, pHpzc, and EDS analyses. Adsorption experiments were performed under varying conditions pH (2–10), contact time (10–180 min), adsorbent mass (0.02–0.14 g) to determine the maximum adsorption capacity (q<sub>max</sub>). Isotherm and thermodynamic models, along with DFT simulations, were used to analyze the adsorption behavior and provide molecular-level insights into methylene blue interactions with the materials.

**Significant Findings:** The CS@ACAP composite exhibited a higher adsorption capacity (81.0 mg/g) compared to activated carbon (40.2 mg/g). Activated carbon achieved optimal adsorption at pH 10, with 160 min and 0.12 g of adsorbent, while CS@ACAP required only 110 min and 0.08 g. Both materials followed the Langmuir model in isotherm studies. Thermodynamic analysis showed exothermic adsorption on activated carbon and endothermic adsorption on CS@ACAP. DFT simulations confirmed stronger MB interactions with CS@ACAP, underscoring its potential as an efficient adsorbent. These findings position CS@ACAP as a promising, eco-friendly material for wastewater treatment.

## 1. Introduction

Water pollution caused by synthetic dyes has emerged as a critical environmental and public health challenge, drawing increasing attention from researchers, policymakers, and industries over the past few decades [1]. The widespread use of synthetic dyes across various

industrial sectors, such as textiles [2], leather, paper, and plastics, has contributed to their ubiquity in the environment [3]. These dyes are valued for their ability to impart vibrant, long-lasting colors to consumer products, which enhances their aesthetic and commercial appeal [4]. However, this very property, combined with their complex chemical compositions, poses severe environmental risks, especially when these

\* Corresponding authors.

E-mail addresses: [soukaina.elbourachdi@usmba.ac.ma](mailto:soukaina.elbourachdi@usmba.ac.ma) (S.E. Bourachdi), [yassine.rakcho@ced.uca.ma](mailto:yassine.rakcho@ced.uca.ma) (Y. Rakcho).

<https://doi.org/10.1016/j.jtice.2025.106142>

Received 29 December 2024; Received in revised form 31 March 2025; Accepted 10 April 2025

Available online 30 April 2025

1876-1070/© 2025 Taiwan Institute of Chemical Engineers. Published by Elsevier B.V. All rights are reserved, including those for text and data mining, AI training, and similar technologies.

dyes are discharged into natural water systems without adequate treatment [5]. The unchecked release of dye-contaminated wastewater not only degrades aquatic ecosystems but also jeopardizes human health, making the development of effective remediation strategies an urgent global priority [6].

Among the wide array of synthetic dyes, Methylene Blue (MB) stands out as a compound of particular concern due to its extensive use and the unique challenges it presents in wastewater management [7]. Methylene Blue (MB) is a synthetic cationic dye that has been widely used across various industries, including textiles, paper, and as a biological stain in laboratories. Despite its broad applications, MB poses significant environmental and health risks, primarily due to its persistence in the environment. The dye is characterized by a complex aromatic ring structure, which contributes to its chemical stability and resistance to natural degradation processes. As a result, MB can accumulate in water bodies, causing long-term pollution that is challenging to mitigate [8]. It is widely used as a biological stain in laboratories, a medical treatment for conditions like methemoglobinemia, and a dye in the textile and paper industries [9]. The environmental impact of MB is profound. In aquatic ecosystems, MB disrupts the natural balance by inhibiting photosynthesis in aquatic plants and algae, which is essential for the survival of these organisms. The dye's presence can lead to reduced oxygen levels, harming aquatic life and altering the food chain. Moreover, MB has been shown to be toxic to a variety of organisms, including fish and invertebrates, and poses risks to human health as well, particularly when it contaminates drinking water sources. Another concerning aspect of MB contamination is its potential for genotoxicity and carcinogenicity [10]. Prolonged exposure to MB has been associated with genetic damage and increased cancer risk in both aquatic organisms and humans. This makes the need for effective and sustainable methods of removing MB from wastewater crucial [11]. Its chemical structure, characterized by a complex aromatic ring system, contributes to its remarkable stability and resistance to natural degradation processes [12]. Furthermore, human health risks associated with MB contamination in water are a major concern. When MB enters the food chain, it can affect humans through the consumption of contaminated water or aquatic organisms. The potential carcinogenic and genotoxic effects of MB exposure are a subject of ongoing research. Studies have indicated that chronic exposure to MB may lead to health issues such as skin irritation, respiratory problems, and even more severe conditions like genetic mutations or cancer [13].

The environmental consequences of Methylene Blue contamination are profound and multifaceted [14]. In aquatic ecosystems, the dye disrupts the delicate balance necessary for the survival of aquatic organisms [15]. One of the most immediate effects of Methylene Blue is its interference with photosynthetic processes in aquatic plants and algae [16]. Moreover, the long-term effects of Methylene Blue exposure remain a topic of active investigation [17]. Emerging studies have raised concerns about its potential carcinogenicity and genotoxicity [18], further emphasizing the need for stringent control measures to limit its presence in the environment. The cumulative health risks associated with this dye make its remediation from wastewater an essential aspect of public health protection [19].

The challenges posed by Methylene Blue contamination have prompted extensive research into effective removal methods. Traditional wastewater treatment techniques, including physical methods such as filtration [20], membrane filtration [21], chemical processes like advanced oxidation [22,23], and coagulation-flocculation [24], as well as biological processes including activated sludge, trickling filters [25], and biofiltration, have been employed to address this issue [26]. However, these methods often have limitations [27], such as high operational costs, incomplete dye removal, and secondary pollution [28]. Among the available strategies, adsorption has gained prominence as a highly effective and versatile approach for dye removal [29].

Adsorption operates on the principle of transferring dye molecules from the aqueous phase onto the surface of an adsorbent material [30],

thereby purifying the water [31]. This method is favored for its simplicity and several other advantages [32]. One of the primary benefits of adsorption is its ability to efficiently remove a wide range of contaminants. It is particularly effective for removing dyes from wastewater, as dyes often have strong molecular structures that can easily interact with adsorbents [33]. The process is straightforward and does not require complex equipment or processes, making it cost-effective and easy to implement [34]. The adsorption capacity is influenced by various factors such as pH, temperature, contact time, and the concentration of the adsorbate. For example, an increase in contact time provides more opportunities for adsorption, while pH can influence the charge and structure of both the adsorbate and the adsorbent, altering the process's efficiency [35]. While conventional adsorbents like activated carbon are widely used due to their high surface area and porosity, the production of activated carbon from traditional sources such as coal, wood, and coconut shells is associated with environmental and economic challenges [36].

Previous studies have explored various methods for the removal of Methylene Blue (MB) from wastewater, with activated carbon emerging as one of the most widely used adsorbents due to its high surface area, porous structure, and excellent adsorption capacity. One significant finding from these studies is the investigation of biomass-sourced activated carbon, such as sugarcane bagasse activated carbon (SCBAC) and espresso coffee waste activated carbon (ECWAC), for MB removal. The research demonstrated that SCBAC was more effective than ECWAC in removing Methylene Blue, with removal efficiencies reaching up to 100 % [37]. Another study investigated the activation of cotton-derived activated carbon (AC) using KOH, achieving a maximum adsorption capacity ( $Q_m$ ) of 31.9 mg/g [38]. A study explored the conversion of waste cigarette butts into activated carbon using  $ZnCl_2$  as a chemical activator. The resulting activated carbon demonstrated a high adsorption capacity for Methylene Blue dye, with a value of 285.7 mg/g at 25 °C [39]. A study evaluated the use of *Spathodea Campanulata*-derived activated carbon for removing Methylene Blue (MB) from wastewater. Prepared through chemical impregnation with  $H_3PO_4$  and thermal activation, the activated carbon achieved a 99.95 % removal efficiency [40]. A study explored the production of low-cost activated carbons from acacia biomass for wastewater treatment. The process involved a one-step carbonization and chemical activation with phosphoric acid at 500 °C. The activated carbon showed a maximum adsorption capacity ( $q_m$ ) of 95.42 mg/g for methylene blue [41].

Activated carbon has long been regarded as one of the most effective adsorbents for environmental remediation, particularly in wastewater treatment. Its ability to remove a wide array of contaminants from dyes and heavy metals to organic compounds can be attributed to its high surface area, porous structure, and chemical reactivity [42]. These features allow activated carbon to adsorb pollutants via both physical and chemical interactions, making it a versatile material for addressing water pollution. Its non-toxic, environmentally friendly nature further enhances its appeal, as it is safe to use and does not release harmful byproducts during its application. Activated carbon can also be regenerated, which means that after its adsorptive capacity is exhausted, it can be thermally treated and reused multiple times, thereby reducing costs associated with disposal and replenishment. This regeneration ability is one of the key reasons activated carbon remains a popular choice in water treatment processes, particularly in industries where large volumes of wastewater need to be treated [43]. However, the widespread use of activated carbon does not come without its challenges. The conventional methods of producing activated carbon especially from coal, wood, and coconut shells pose several environmental and economic concerns [44]. The extraction of these raw materials can be harmful to the environment, often involving deforestation, habitat destruction, and the depletion of non-renewable resources. Additionally, the production process itself is energy-intensive, requiring high temperatures to activate the carbon, which leads to increased carbon emissions. This not only contributes to global warming but also adds to

the overall environmental footprint of the material. The cost of producing activated carbon from these traditional sources can also be high, making it an expensive solution for large-scale applications or in regions with limited financial resources [45]. In response to these issues, there has been growing interest in developing sustainable alternatives to traditional activated carbon. Agricultural byproducts, such as avocado pits, have emerged as promising precursors for producing activated carbon. These byproducts are abundant, renewable, and low-cost, making them an ideal alternative to traditional raw materials. The production of activated carbon from agricultural waste offers numerous advantages. For one, it helps address the growing problem of agricultural waste disposal, converting it into a valuable product instead of allowing it to go to waste [46]. By using these waste materials, the production of activated carbon can contribute to a more sustainable circular economy. Moreover, bio-based activated carbon produced from materials like avocado pits often exhibits similar, if not superior, adsorption capacities compared to traditional activated carbon, making it just as effective for removing pollutants from wastewater [47]. In addition to its environmental benefits, using agricultural waste for activated carbon production helps reduce the economic burden associated with raw material acquisition. The use of low-cost waste materials lowers production expenses and makes the material more accessible for industries and regions where the cost of conventional activated carbon might otherwise be prohibitive. Furthermore, as research continues to evolve, it is becoming clear that bio-based activated carbons can be tailored to meet specific needs, enhancing their adsorption efficiency for various contaminants. For instance, the modification of bio-based carbons with other materials, such as chitosan or other polymers, has shown promise in increasing their performance, expanding their potential applications even further [48].

Similarly, chitosan, a biopolymer derived from chitin, has emerged as a highly effective adsorbent for dye removal [49]. Extracted from crustacean shells, chitosan is not only biodegradable and non-toxic but also possesses unique structural features that enhance its adsorption capacity [50]. The molecular structure of chitosan contains both amino and hydroxyl groups, which serve as active sites for the adsorption of various pollutants [51], particularly dye molecules [52]. These functional groups facilitate strong interactions with cationic dyes, such as Methylene Blue, through electrostatic attraction and hydrogen bonding, thus enhancing the adsorption efficiency [53]. In addition to its natural adsorption capacity, chitosan's structure can be modified to further improve its performance [54].

Chitosan@activated carbon beads represent a powerful and sustainable solution for water treatment applications, combining the unique advantages of chitosan and activated carbon into a versatile composite material. These beads exhibit enhanced adsorption efficiency due to the synergistic effects of chitosan's functional amino and hydroxyl groups and activated carbon's high surface area and porosity [55]. The bead format ensures mechanical stability and ease of handling, making them suitable for dynamic systems without significant material loss. Derived from renewable resources like crustacean shells and agricultural byproducts, chitosan@activated carbon beads are environmentally friendly, biodegradable, and cost-effective. Additionally, their ability to be regenerated and reused further enhances their practicality for large-scale wastewater treatment.

The objective of this study was to develop and optimize an efficient method for the removal of Methylene Blue (MB) from aqueous solutions. To achieve this, activated carbon was synthesized from avocado pits and its preparation was systematically optimized using the Box-Behnken design, focusing on three key parameters: sulfuric acid ( $\text{H}_2\text{SO}_4$ ) concentration, activation time, and activation temperature. The optimized activated carbon was further modified by incorporating chitosan to synthesize a composite material, Chitosan@Activated Carbon Avocado Pits (CS@ACAP). A primary goal of the study was to evaluate and compare the adsorption performance of the activated carbon and the chitosan-modified composite under various experimental conditions.

This included optimizing parameters such as pH, contact time, adsorbent mass, and initial dye concentration to maximize adsorption efficiency. Both materials were characterized using advanced techniques, including FTIR, SEM, XRD, BET, and EDS analyses, to assess their structural, morphological, and surface properties. Furthermore, the study aimed to elucidate the adsorption mechanisms by conducting isotherm modeling and thermodynamic analyses. The Langmuir and Freundlich models were applied to determine the adsorption behavior and surface characteristics of the materials. Thermodynamic parameters, such as changes in enthalpy ( $\Delta\text{H}^\circ$ ), entropy ( $\Delta\text{S}^\circ$ ), and Gibbs free energy ( $\Delta\text{G}^\circ$ ), were analyzed to understand the nature of the adsorption processes. To complement the experimental findings, density functional theory (DFT) simulations were conducted to examine the molecular interactions between MB and the two adsorbent materials. These simulations provided deeper insights into the binding affinities, surface heterogeneities, and energy changes associated with MB adsorption.

By integrating experimental optimization, advanced characterization, and theoretical modeling, this study sought to establish the chitosan-modified activated carbon as a highly efficient and sustainable material for MB removal.

## 2. Materials and methods

### 2.1. Chemical and reagents

The materials used in this study include hydrochloric acid (HCl) and sodium hydroxide (NaOH), both purchased from Sigma-Aldrich. Distilled water was used as the solvent throughout the experimental procedures. Methylene Blue ( $\text{C}_{16}\text{H}_{18}\text{ClN}_3\text{S}$ ), a commonly used synthetic dye with a molecular weight of 319.85 g/mol, was utilized in the adsorption experiments. The dye's maximum absorbance ( $\lambda_{\text{max}}$ ) is typically observed at 664 nm, which is used for its quantification [56].

### 2.2. Preparation of chitosan@activated carbon avocado pits beads

The preparation of CS@ACAP beads involves a series of well-defined steps, including the activation of carbon and the processing of extraction of chitosan to create an effective composite material.

#### 2.2.1. Activation of carbon

The process begins with the preparation of activated carbon from avocado pits. Initially, the pits are thoroughly cleaned and cut into small pieces to facilitate the subsequent processing steps. The pieces then dried in an oven to eliminate moisture content. Once dried, the pits fragments are ground into a fine powder, which serves as the precursor material for the activation process [57]. This ground material is subsequently activated by treating it with sulfuric acid ( $\text{H}_2\text{SO}_4$ ) at concentrations of 3 N, 6 N, and 9 N. The activation process is carried out with continuous agitation for varying time durations of 4, 14, and 24 h [58].

After the activation step, the activated carbon is thoroughly rinsed with distilled water to remove any residual sulfuric acid. The rinsing process continues until a neutral pH of 7 is achieved, ensuring that the material is free from excess acidity and ready for subsequent use in the composite preparation [59]. The rinsed carbon is then subjected to thermal treatment in a furnace at temperatures of 200 °C, 350 °C, and 500 °C for 1 hour. This step is crucial for further enhancing the porosity and surface area of the material, resulting in the final activated carbon product [60]. Fig. 1 illustrates the method of preparation of activated carbon from avocado pits.

#### 2.2.2. Extraction of chitosan

The extraction of chitosan involves a series of chemical treatments. Initially, deprotonation is carried out using 2 N sodium hydroxide (NaOH) to remove any protonated groups [61]. Following the deprotonation step, demineralization is performed using 1 N hydrochloric acid (HCl) to remove mineral impurities, ensuring the purity of the

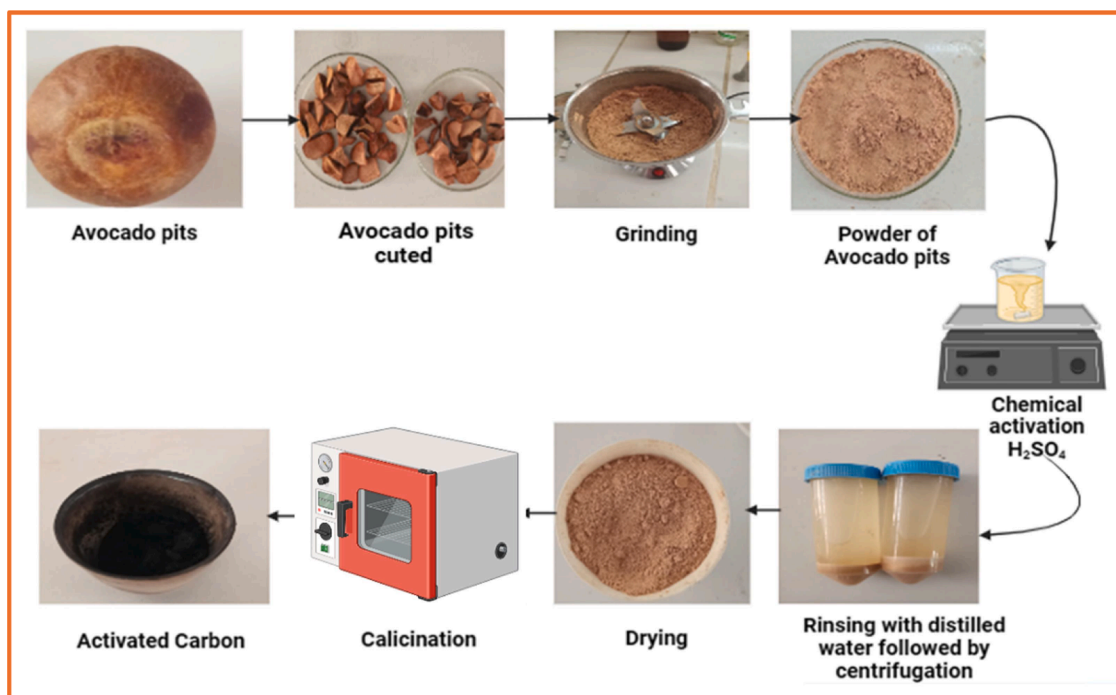


Fig. 1. Representation of the Activated carbon from avocado pits.

chitosan. Finally, deacetylation is carried out using 45 % sodium hydroxide (NaOH), which facilitates the conversion of chitin into chitosan by removing acetyl groups, a critical step in obtaining the desired chitosan material for the composite preparation [62].

### 2.2.3. Preparation of chitosan@Activated carbon avocado pits (CS@ACAP) beads

For the preparation of CS@ACAP beads, chitosan is first dissolved in a 2 % acetic acid solution to obtain a homogeneous chitosan solution [63]. Activated carbon is subsequently added to the chitosan solution

and the mixture is agitated for 24 h to ensure thorough dispersion of the carbon within the chitosan matrix [64]. This extended agitation period facilitates the uniform distribution of activated carbon. To form the beads, the chitosan@Activated carbon mixture is extruded using a syringe into a 2 N NaOH solution [65]. This step causes the chitosan to gel and solidify around the activated carbon particles, forming uniform beads. The beads are thoroughly washed with distilled water to remove any residual chemicals and impurities. Fig. 2 illustrates the method of preparation of CS@ACAP beads.

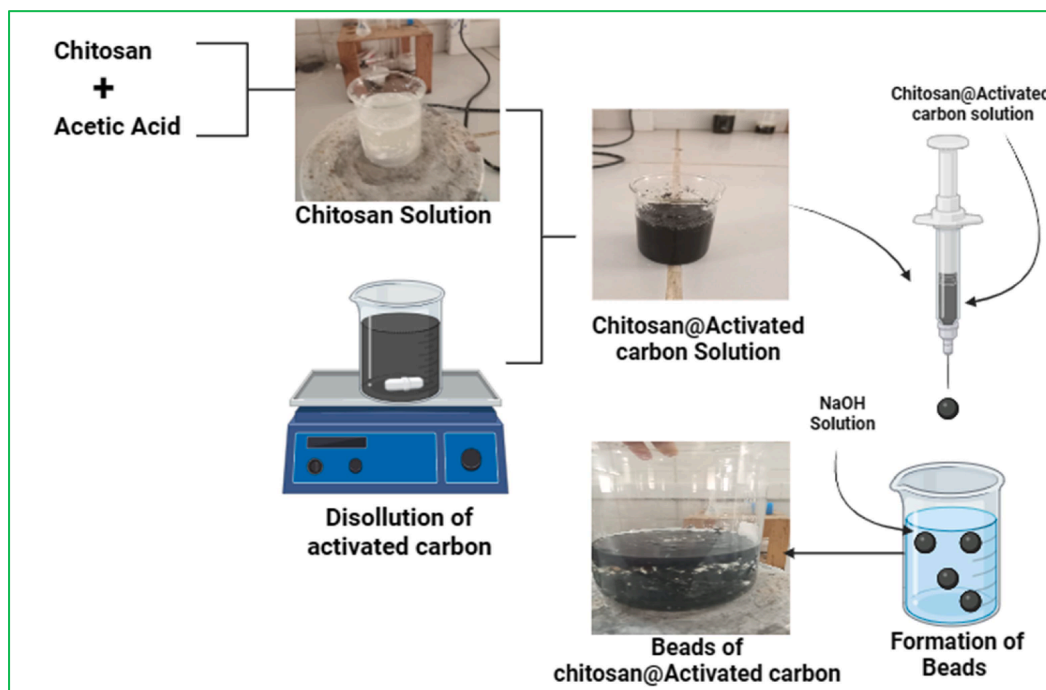


Fig. 2. Representation of Beads Formation Process of CS@ACAP beads.

### 2.3. Instruments for characterization

The characterization of ACAP and chitosan@ACAP involves several key analytical techniques. Infrared Spectroscopy (IR) is used to identify functional groups and interactions between chitosan and activated carbon. X-ray Diffraction (XRD) is used to assess the crystalline structure of the material [66]. Brunauer-Emmett-Teller (BET) analysis is used to measure the specific surface area and pore size distribution, which are crucial for understanding adsorption capacity [67]. Scanning Electron Microscopy (SEM) provides detailed images of surface morphology, allowing for the visualization of the distribution and dispersion of activated carbon particles within the chitosan matrix [68]. Spectroscopy (EDX) is employed to determine the elemental composition of the materials, confirming the presence of key elements such as carbon, oxygen, and other components relevant to the composite structure [69].

#### 2.3.1. Surface charge zero charge point

The point of zero charge ( $pH_{PZC}$ ) of avocado pits before and after activation, as well as the composite CS@ACAP beads, is a critical parameter. It indicates the pH at which the surface of these materials exhibits no net electrical charge [70]. To determine the pH at the point of zero charge ( $pH_{PZC}$ ), 0.1 g of avocado pits, both before and after activation, as well as the composite CS@ACAP, are each immersed in a series of 20 mL aqueous solutions with varying initial pH values, typically ranging from 3 to 12 [71]. After equilibration, the final pH of each solution is measured. The  $pH_{PZC}$  is determined as the point where the plot of initial pH versus final pH intersects the line representing equality between initial and final pH [72]. This intersection represents the pH at which the material's surface carries no net electrical charge, which is a key factor in predicting the adsorption behavior of the materials across different pH environments.

### 3. Box-Behnken design concept

The Box-Behnken design (BBD) is a statistical tool commonly employed within response surface methodology (RSM) to optimize complex processes involving multiple variables, particularly when experimental resources are limited or when the system being studied is complex and nonlinear in nature [6]. This design is favored for its ability to provide valuable insights into the relationships between input factors while minimizing the number of experimental runs required. One of the most significant advantages of BBD over other experimental designs, such as full factorial or central composite designs, lies in its efficiency. The BBD design allows for the exploration of a broad range of interactions between variables using fewer experiments, which is particularly important when working with limited time or resources [73]. By focusing on a central, more manageable set of factor levels, the design eliminates the need for testing extreme combinations of factors, which might be impractical or lead to errors in other design approaches. This feature makes BBD a more manageable and cost-effective choice, especially in studies where minimizing experimental effort is a key consideration. Furthermore, the BBD design offers the added benefit of not requiring the study of combinations of factor levels that might result in undesirable or impossible experimental conditions, reducing the risk of outliers that could skew results [74]. Another key advantage of BBD is its ability to assess the nonlinear relationships and interaction effects between multiple variables with relative ease [75]. This is of particular importance in studies involving complex materials and processes, such as the synthesis of activated carbon from avocado pits, where the factors being studied (sulfuric acid concentration, activation time, and calcination temperature) interact in ways that cannot be easily predicted or assessed using traditional single-variable methods. While other experimental designs, such as full factorial designs, require significantly more trials to evaluate multiple factors at different levels, BBD allows for a more efficient and precise determination of optimal factor levels without the need for a prohibitive number of experiments [76]. This efficiency is

critical for studies that aim to balance resource use with experimental rigor. In the context of this study, BBD was chosen specifically for its ability to optimize the synthesis of activated carbon from avocado pits, focusing on three critical factors. The selection of these parameters was based on their significant impact on the physical and chemical properties of the activated carbon, and consequently, its adsorption capabilities. Sulfuric acid concentration, for example, influences the extent of activation and the development of the carbon's surface area and porosity [77]. Activation time affects the duration over which these surface properties are enhanced [78], while calcination temperature plays a critical role in stabilizing the activated carbon structure and further refining its porosity [79]. These factors are known to play pivotal roles in influencing the physical and chemical properties of the activated carbon, including its surface area, porosity, and ultimately, its efficiency in removing pollutants such as Methylene Blue dye from wastewater. The optimization of these three factors, therefore, is essential in achieving an activated carbon material with enhanced adsorption capacity for Methylene Blue, which is the response variable of interest in our study. The reason for selecting BBD over other methodologies stems from its ability to comprehensively assess the interactions between these three critical factors while minimizing the number of experimental trials [80,81]. Ultimately, the use of the Box-Behnken design in this study is critical to addressing the research question of optimizing the activated carbon synthesis process for maximum dye removal efficiency. By minimizing the number of experimental runs required, BBD not only ensures that we can efficiently explore the parameter space but also helps reduce experimental errors that might arise from impractical factor combinations [82]. Moreover, it facilitates a deeper understanding of the interactions between the factors involved, which will ultimately lead to the identification of optimal conditions for the production of activated carbon with superior adsorption capacity [83,84].

Through the systematic variation of these parameters, as defined by the Box-Behnken Design (BBD), we were able to create a response surface that provided insights into the optimal conditions for maximum dye removal. The BBD enabled us to identify not only the best combination of sulfuric acid concentration, activation time, and calcination temperature but also to understand the interactions between these factors. Table 1 presents the key factors and their corresponding ranges used in the optimization. These factors were varied to study their interaction effects on Methylene Blue (MB) removal efficiency.

To achieve this optimization, BBD was employed, efficiently exploring the interactions between multiple variables while minimizing the number of experimental runs required [85]. The BBD framework is particularly well-suited for studies where the relationships between the factors are non-linear and where interactions between variables are expected to play a significant role in the outcome [86]. In this study, the model was constructed based on 17 carefully designed experiments, each representing a unique combination of the three key variables. The response of interest, the yield of Methylene Blue removal, was analyzed using a quadratic polynomial equation that incorporates linear, interaction, and quadratic effects of the independent variables [87]. This type of equation enables a detailed exploration of how each factor, both individually and in combination with others, affects the removal efficiency. The general form of Eq. (1) is as follows [88]:

$$Y_i = \beta_0 + \sum_{i=1}^n (\beta_i X_i) + \sum_{i=1}^n (\beta_{ii} X_i^2) + \sum_{i=1}^{n-1} \sum_{j=1}^n (\beta_{ij} X_i X_j) \quad (1)$$

In this equation,  $Y_i$  represents the measured response for each

**Table 1**  
Experimental design levels for various parameters.

Factor	Name	Units	Minimum	Maximum	Mean
A	H <sub>2</sub> SO <sub>4</sub>	N	3.00	9.00	6.00
B	Time of Activation	Hours	4.00	24.00	14.00
C	Temperature	°C	200.00	500.00	350.00

experiment iii, which in this case is the percentage of Methylene Blue removed. The coefficients  $\beta_0$ ,  $\beta_i$ ,  $\beta_{ii}$ , and  $\beta_{ij}$  correspond to the constant term, linear effects, quadratic effects, and interaction effects, respectively [89]. The variables  $X_i$  and  $X_j$  represent the coded levels of the independent variables, such as sulfuric acid concentration, activation time, and calcination temperature. By analyzing the results from these 17 experiments, the study was able to construct a response surface that illustrates how changes in the independent variables affect the yield of Methylene Blue removal. This response surface not only identifies the optimal conditions for maximizing dye removal but also provides insights into the nature of the interactions between the variables, highlighting which combinations of factors are most critical for achieving high removal efficiency [90]. Table 2 presents the experimental runs conducted to evaluate the effects of different parameters on the removal efficiency of methylene blue (MB) using activated carbon prepared from avocado pits.

As shown, the predicted and experimental values of methylene blue (BM) removal are in strong agreement, with the predicted values closely matching the experimental results across all experimental runs. The correlation between the predicted and experimental BM removal percentages indicates that the model effectively describes the adsorption behavior under varying conditions. For example, the experimental BM removal percentages ranged from 3.66 % to 86.26 %, while the predicted values varied between 3.78 % and 85.16 %, demonstrating a minimal discrepancy [91]. This high degree of consistency between the predicted and experimental results further supports the validity and reliability of the Box-Behnken model in optimizing the methylene blue removal process [92].

## 4. Adsorption

### 4.1. Adsorbate preparation

The preparation of Methylene Blue, the adsorbate, is a critical step in the adsorption experiments. A stock solution of Methylene Blue was prepared by dissolving 1 g of the dye in 1 L of distilled water, resulting in a concentration of 1000 mg/L. This concentration was chosen to provide a sufficiently high initial dye concentration for the adsorption experiments, thereby enabling a clear evaluation of the adsorptive capacity and efficiency of both activated carbon (ACAP) and the composite CS@ACAP. The stock solution was thoroughly mixed to ensure the complete dissolution of the Methylene Blue dye, resulting in a homogeneous solution with a consistent concentration throughout. This stock solution was then used to prepare various diluted solutions, tailored to different experimental conditions, including contact time, pH, and adsorbent mass.

**Table 2**  
Experimental design and response model.

Run	Concentration Of H <sub>2</sub> SO <sub>4</sub> (N)	Time of Activation Hours	Temperature °C	BM removal Experimental (%)	BM removal predite (%)
1	6	14	350	40.23	40.58
2	6	14	350	40.78	40.58
3	6	14	350	40.22	40.58
4	9	14	200	14.96	16.03
5	6	14	350	40.78	40.58
6	6	14	350	40.89	40.58
7	9	4	350	3.66	3.78
8	6	24	200	53.7	52.29
9	9	24	350	45.27	45.61
10	9	14	500	45.5	43.97
11	6	4	500	41.29	42.70
12	3	24	350	82.66	82.54
13	6	24	500	83.96	85.16
14	3	4	350	60.42	60.08
15	3	14	200	66.5	68.03
16	3	14	500	86.26	85.19
17	6	4	200	31.67	30.47

### 4.2. Study of methylene blue adsorption kinetics

#### 4.2.1. Effect of contact time

The effect of contact time on the adsorption of Methylene Blue was investigated using an initial dye concentration of 50 mg/L and an adsorbent mass of 0.1 g. Adsorption experiments were carried out over a time range from 10 to 180 min to determine the optimal contact time for maximum dye removal. At each time interval, samples were collected, centrifuged, and the residual Methylene Blue concentration was measured. The samples were then analyzed using a Shimadzu UV-Visible spectrophotometer ( $\lambda = 664$  nm) to determine the concentration of residual Methylene Blue. Quantities of dye adsorbed per unit mass ( $Q_e$ ) and percent elimination (R %) are calculated based on Eq. (2) and (3) [93]:

$$Q_e = (C_i - C_e) \times \frac{V}{m} \quad (2)$$

$$R \% = \left( \frac{C_i - C_e}{C_i} \right) \times 100 \quad (3)$$

Where:  $C_i$  (mg/L) is the initial concentration of Methylene Blue.  $C_e$  (mg/L) is the equilibrium concentration of Methylene Blue.  $V$  (L) is the volume of the Methylene Blue solution.  $w$  (g) is the mass of ACAP or CS@ACAP composite.

#### 4.2.2. Modeling the adsorption kinetics of methylene blue

To understand the kinetics of Methylene Blue adsorption onto ACAP and CS@ACAP, both pseudo-first-order and pseudo-second-order kinetic models were employed [94]. These models provide insights into the nature of the adsorption process, including the rate at which Methylene Blue is removed from the solution and the mechanism underlying the interaction between the dye and the adsorbent [95]. The pseudo-first-order model is frequently employed in dye adsorption studies due to its capability to describe adsorption kinetics in systems where the rate of adsorption is primarily governed by the difference between the equilibrium dye concentration and the amount adsorbed at any given time. This model offers valuable insights into the adsorption rate and the interaction mechanisms between Methylene Blue and the adsorbent, allowing for the prediction of system behavior over time. The model is represented by the following Eq. (4):

$$\ln(Q_e - Q_t) = \ln Q_e - k_1 t \quad (4)$$

Where:  $Q_t$  is the amount of dye adsorbed at time  $t$ ,  $Q_e$  is the equilibrium amount of dye adsorbed, and  $k_1$  is the rate constant of the pseudo-first-order adsorption. This model assumes that the rate of adsorption is proportional to the difference between the equilibrium concentration and the concentration at time  $t$  [96].

On the other hand, the pseudo-second-order model, proposed by Ho and McKay, is commonly utilized to describe adsorption processes in which the rate of adsorption is dependent on the square of the difference between the amount of dye adsorbed and the equilibrium adsorption capacity. This model is particularly useful for systems where the adsorption rate slows as the adsorption sites become occupied, and it offers a more accurate representation of the adsorption process at higher dye concentrations [97]. This model provides insights into the adsorption rate and the capacity of the adsorbent, and is given by Eq. (5):

$$\frac{t}{Q_t} = \frac{1}{k_2(Q_e)^2} + \frac{t}{Q_e} \quad (5)$$

where  $k_2$  is the rate constant of the pseudo-second-order adsorption. This model posits that the rate of adsorption is proportional to the square of the difference between the equilibrium concentration and the concentration at time  $t$  [98].

#### 4.3. Identification of optimum adsorption conditions for methylene blue

To determine the optimum conditions for the adsorption of Methylene Blue onto ACAP and CS@ACAP, a comprehensive analysis was conducted, considering several key variables: adsorbent mass, pH, dye concentration, and temperature. The adsorbent mass was varied between 0.02 g and 0.14 g to assess its impact on the removal efficiency. The pH was adjusted within the range of 2 to 10 to identify the optimal value for maximizing dye uptake, as pH can significantly affect the surface charge of the adsorbent and the ionization state of the dye. The initial Methylene Blue concentration was varied between 25 mg/L and 200 mg/L to explore how different dye concentrations influence the adsorption process, providing insights into the adsorbent's capacity and efficiency. Furthermore, the temperature was varied from 25 °C to 45 °C to evaluate its effect on the adsorption rate and equilibrium.

#### 4.4. Adsorption isotherm

##### 4.4.1. The langmuir models

The Langmuir adsorption isotherm is a fundamental model used to describe the adsorption of Methylene Blue onto ACAP and CS@ACAP beads. It assumes monolayer coverage of the adsorbate on a surface with a finite number of identical and non-interacting sites [99]. This model is particularly suitable for our study as it assumes that adsorption occurs at specific, homogeneous sites on ACAP and CS@ACAP, and once these sites are occupied by Methylene Blue molecules, no further adsorption can occur at those sites [100]. It is typically applied in cases where understanding the maximum adsorption capacity and the efficiency of adsorbents is essential. The Langmuir isotherm is expressed by Eq. (6):

$$\frac{C_e}{Q_e} = \frac{1}{K_L Q_m} + \frac{C_e}{Q_m} \quad (6)$$

where  $Q_e$  represents the amount of Methylene Blue adsorbed per unit mass of the onto ACAP and CS@ACAP beads at equilibrium,  $Q_m$  is the maximum adsorption capacity,  $K_L$  is the Langmuir constant reflecting the affinity of the adsorbent for the dye, and  $C_e$  is the equilibrium concentration of Methylene Blue.

##### 4.4.2. The Freundlich model

The Freundlich adsorption isotherm is another widely used model that describes the adsorption of substances onto heterogeneous surfaces [101]. The Freundlich model accommodates varying adsorption sites and capacities on a heterogeneous surface [102]. This model is particularly useful for describing adsorption processes where the adsorbent surface exhibits a range of affinities for the adsorbate, making it suitable for systems with non-uniform surface properties. The Freundlich isotherm is expressed by Eq. (7):

$$\ln(Q_e) = \ln(K_F) + \frac{1}{n_F} \ln(C_e) \quad (7)$$

where  $Q_e$  is the amount of adsorbate (Methylene Blue) adsorbed per unit mass of the adsorbent at equilibrium,  $C_e$  is the equilibrium concentration of the adsorbate,  $K_F$  is the Freundlich constant indicating the adsorption capacity, and  $1/n_F$  is a dimensionless constant that represents the adsorption intensity or surface heterogeneity.

#### 4.5. Adsorption thermodynamic

Adsorption thermodynamics provides insight into the energy changes and equilibrium behavior of adsorption processes, offering a deeper understanding of the interactions between adsorbate and adsorbents [103]. It involves the study of how temperature, enthalpy, and entropy affect the adsorption equilibrium and the spontaneity of the process [104]. Key thermodynamic parameters, such as the Gibbs free energy change ( $\Delta G^\circ$ ), enthalpy change ( $\Delta H^\circ$ ), and entropy change ( $\Delta S^\circ$ ), are crucial for evaluating the feasibility and nature of adsorption. Using Eq. (8),(9),(10), and a plot of  $\ln K_e$  versus  $1/T$ , essential thermodynamic parameters like entropy ( $\Delta S^\circ$ ), enthalpy ( $\Delta H^\circ$ ), and Gibbs free energy ( $\Delta G^\circ$ ) can be determined.

$$K_e = \frac{Q_e}{C_e} \quad (8)$$

$$\ln K_e = \frac{\Delta S^\circ}{R} - \frac{\Delta H^\circ}{RT} \quad (9)$$

$$\Delta G = \Delta H - T\Delta S \quad (10)$$

Where  $K_e$ : equilibrium distribution coefficient.  $Q_e$  (mg.g<sup>-1</sup>): Methylene blue adsorption on chitosan beads' surface.  $C_e$  (mg.L<sup>-1</sup>): equilibrium Methylene blue concentration.  $T$  (K): absolute temperature, and  $R$  (8.314 J.mol<sup>-1</sup>. K<sup>-1</sup>): the universal gas constant.

#### 5. Mechanism and calculations of density functional theory (DFT)

In our study, we performed a comprehensive quantum mechanical analysis using the Gaussian09W program and GaussView5.0.8 software [105]. The analysis was based on Density Functional Theory (DFT), a well-established and robust computational approach for investigating molecular systems. We employed the B3LYP hybrid functional, which is a widely used and highly reliable method in DFT calculations [106]. The B3LYP functional combines the Becke's three-parameter exchange functional with the Lee-Yang-Parr correlation functional, and is known for its accuracy in predicting molecular structures, electronic properties, and reaction mechanisms. This functional was chosen for its proven ability to provide accurate results for systems similar to the Methylene Blue molecule, particularly in terms of predicting binding interactions and stability in adsorption processes. To accurately model the molecular systems in this study, we employed the 6-31G(d,p) basis set, a split-valence set enhanced with polarization functions on heavier atoms and diffuse functions to accurately represent electron density, particularly in regions far from the nuclei. This choice was driven by its optimal balance between computational efficiency and reliability for the calculations performed, allowing us to gain detailed insights into the interactions and stability of Methylene Blue when adsorbed onto the surfaces of ACAP and CS@ACAP beads. The 6-31 G basis set, which includes six Gaussian functions for core electrons and three for valence electrons in the first shell, along with one for the second shell, offers an efficient yet accurate solution for systems involving light elements like carbon, nitrogen, and oxygen. For higher accuracy in certain calculations, we also utilized the 6-311G\* basis set, which augments 6-31 G with additional polarization functions to better capture electron distribution, making it particularly useful for studying transition states and

reaction mechanisms. By optimizing the molecular geometry and analyzing the electronic distribution of the Methylene Blue molecule, we gained valuable insights into the intricate interactions between the dye and the surfaces of the adsorbent materials, specifically the ACAP and CS@ACAP beads composite. The geometry optimization process, which involves refining the atomic positions to minimize the total energy of the system, allowed us to determine the most stable configurations of Methylene Blue when adsorbed onto the adsorbents surfaces. This step is crucial for understanding how the molecular structure of the dye changes upon adsorption and how these structural changes influence its binding affinity. In addition to the geometric optimization, the analysis of the electronic distribution provided detailed information about the electron density and how it is redistributed upon interaction with the adsorbents surfaces. This helps to identify key regions of the dye molecule that are involved in the adsorption process, such as areas with high electron density that might interact with the surface via  $\pi$ - $\pi$  stacking, hydrogen bonding, or electrostatic forces. By examining these electronic properties, we were able to uncover the nature of the binding forces and the overall stability of the adsorbed dye. The quantum chemical analysis not only helped in elucidating the fundamental adsorption mechanisms but also provided a deeper understanding of how the ACAP and CS@ACAP composite beads enhance the adsorption efficiency of Methylene Blue. By understanding the interactions at the molecular level, we can optimize the design of the adsorbent materials to maximize their effectiveness in capturing the dye. This analysis is particularly significant for advancing the development of adsorbent materials with tailored properties, allowing for better control over the adsorption capacity and selectivity. Furthermore, the insights gained from the quantum chemical calculations contribute to the rational design of novel adsorbent materials with improved performance in practical applications such as wastewater treatment and environmental remediation [107]. In our quantum chemical analysis, several key quantum parameters were computed for the optimized structures of Methylene Blue to provide a deeper understanding of the electronic properties and reactivity of the molecule. These parameters are crucial for evaluating the molecule's behavior in the adsorption process and its interaction with the ACAP and CS@ACAP bead surfaces. Specifically, we calculated the energy of the Highest Occupied Molecular Orbital (HOMO), the energy of the Lowest Unoccupied Molecular Orbital (LUMO), and the energy gap ( $\Delta E_{\text{gap}}$ ) between these orbitals. The HOMO represents the highest energy electron that is still bound to the molecule, while the LUMO represents the lowest energy orbital that is unoccupied and available for interactions with other molecules. The energy gap ( $\Delta E_{\text{gap}}$ ) between these orbitals is a critical parameter, as it indicates the molecule's ability to donate or accept electrons during chemical reactions. A smaller  $\Delta E_{\text{gap}}$  generally suggests greater chemical reactivity, as the molecule is more easily excited from the HOMO to the LUMO, facilitating electron transfer processes [108]. The HOMO and LUMO energies are crucial for understanding the electron donation and acceptance capabilities of the molecules, while the energy gap ( $\Delta E_{\text{gap}}$ ) indicates the stability and reactivity of the molecule [109]. Additionally, we assessed several important molecular properties to further characterize the optimized structures of Methylene Blue, which provide a deeper understanding of its reactivity and potential interactions with the adsorbent surfaces. These properties include electrophilicity ( $\omega$ ), softness ( $\sigma$ ), hardness ( $\eta$ ), absolute electronegativity ( $\chi$ ), and dipole moment ( $\mu$ ), each of which plays a significant role in determining the molecule's chemical behavior and its potential for interaction in the adsorption process. Electrophilicity ( $\omega$ ) measures the molecule's ability to accept electrons, which is essential for understanding its interaction with electron-rich surfaces such as those found in the adsorbent materials. A higher electrophilicity indicates that the molecule is more likely to act as an electrophile, making it more reactive in adsorption processes. We closely monitored the change in total energy between successive iterations, with a convergence threshold typically set between  $10^{-6}$  and  $10^{-8}$  atomic units (a.u.). The calculation was considered converged once the

energy change fell below this threshold. Additionally, for molecular dynamics and structure optimization, the forces acting on atoms were minimized. The convergence criterion for force minimization involved comparing the magnitudes of atomic forces between iterations, achieving convergence when the forces fell below  $10^{-4}$  to  $10^{-5}$  a.u./Å. We also calculated the softness ( $\sigma$ ) and hardness ( $\eta$ ), which are key concepts in chemical reactivity. Softness refers to the molecule's tendency to undergo a chemical reaction, while hardness reflects the molecule's resistance to changes in its electron density. Soft molecules are typically more reactive and can easily interact with softer materials, while harder molecules are more stable and less reactive. The balance between softness and hardness of Methylene Blue can provide important clues about its reactivity with the ACAP and CS@ACAP beads, influencing the adsorption efficiency. The absolute electronegativity ( $\chi$ ) was also calculated, which gives an indication of the molecule's ability to attract electrons towards itself. A molecule with high electronegativity is more likely to form stronger interactions with electron-donating surfaces. Lastly, the dipole moment ( $\mu$ ) was computed to evaluate the polarity of the Methylene Blue molecule. The dipole moment is a measure of the separation of charge within the molecule, and molecules with higher dipole moments tend to exhibit stronger interactions with polar surfaces, such as those of the adsorbent materials. By analyzing these parameters, we were able to gain a comprehensive understanding of the molecule's electronic structure and its potential reactivity, which are critical for optimizing the adsorption process and enhancing the performance of the adsorbent material [110]. These parameters were calculated using Eq. (11), (12) and (13) to evaluate various aspects of chemical reactivity and electronic structure:

$$\Delta E_{\text{Gap}} = E_{\text{LUMO}} - E_{\text{HOMO}} \quad (11)$$

$$\eta = \frac{E_{\text{LUMO}} - E_{\text{HOMO}}}{2} \quad (12)$$

$$\chi = \frac{-(E_{\text{HOMO}} + E_{\text{LUMO}})}{2} \quad (13)$$

The overall softness ( $S$ ) is the inverse of the overall hardness according to Eq. (14):

$$S = \frac{1}{\eta} \quad (14)$$

The electrophilicity index ( $\omega$ ) is determined by applying Parr's concept according to the Eq. (15):

$$\omega = \frac{\chi^2}{2\eta} \quad (15)$$

## 6. Characterization

### 6.1. Fourier transform infrared spectroscopy (FTIR)

Fig. 3a and 3b present the FTIR spectra of both raw avocado pits and activated carbon derived from avocado pits, highlighting the chemical transformations induced by the activation process. In Fig. 3a, the spectrum of raw avocado pits exhibits a broad absorption band at  $3298 \text{ cm}^{-1}$ , corresponding to O–H stretching vibrations, which suggests the presence of hydroxyl groups likely from moisture or cellulose-based components [111]. The distinct peaks at  $2935 \text{ cm}^{-1}$  and  $2850 \text{ cm}^{-1}$  correspond to C–H stretching vibrations of aliphatic hydrocarbons, indicating the presence of long-chain organic compounds. Additionally, the peak at  $1623 \text{ cm}^{-1}$  is attributed to C = O stretching, suggesting the presence of carbonyl groups, such as aldehydes or ketones [112]. The peaks at  $1445 \text{ cm}^{-1}$  and  $1272 \text{ cm}^{-1}$  correspond to C–H bending and C–O stretching, respectively, which are characteristic of lignocellulosic materials [113]. Additional peaks at  $1154 \text{ cm}^{-1}$  and  $1078 \text{ cm}^{-1}$  further confirm the presence of polysaccharides, such as cellulose and hemicellulose [114]. After

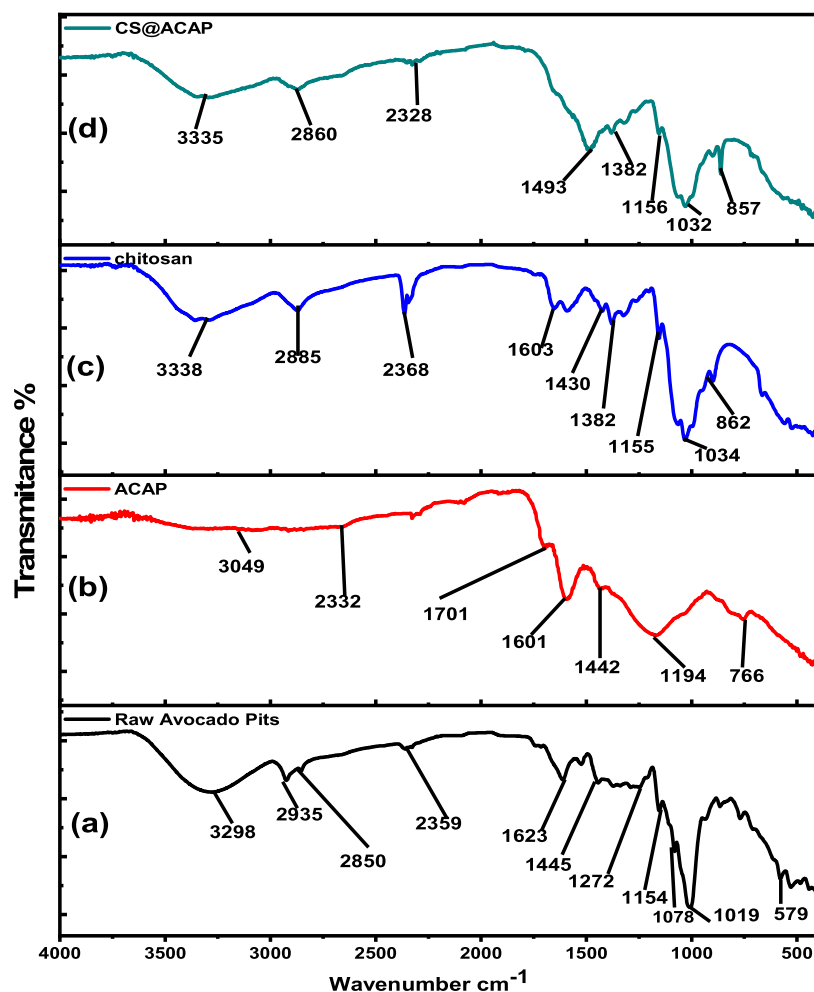


Fig. 3. Infrared Spectra of a) Avocado pits, b) ACAP, c) Chitosan, d) CS@ACAP composite.

activation, Fig. 3b presents the FTIR spectrum of the activated carbon, revealing significant changes. New peaks appear at  $3049\text{ cm}^{-1}$  and  $1701\text{ cm}^{-1}$ , indicating the formation of carbonyl functional groups [115]. The appearance of a peak at  $766\text{ cm}^{-1}$  corresponds to aromatic skeletal vibrations, suggesting the development of a more ordered, carbon-rich structure. Additionally, the reduced intensity of the O–H and C–H peaks, along with the appearance of new functional groups, confirms that the activation process has successfully transformed the raw material into activated carbon [116]. The spectra in Fig. 3c and 3d of pure chitosan and CS@ACAP reveal distinct differences, highlighting changes in functional groups during composite formation. In the spectrum of pure chitosan (Fig. 3c), a broad peak at  $3338\text{ cm}^{-1}$  corresponds to O–H and N–H stretching vibrations, which are characteristic of hydroxyl and amine groups [117]. The peak at  $2885\text{ cm}^{-1}$  corresponds to C–H stretching from aliphatic chains, while the peaks at  $1660\text{ cm}^{-1}$  and  $1603\text{ cm}^{-1}$  are attributed to C = O stretching (amide I) and N–H bending (amide II), respectively, confirming the amide structure of the polymer [118]. Additional peaks at  $1430\text{ cm}^{-1}$ ,  $1382\text{ cm}^{-1}$ , and  $1155\text{ cm}^{-1}$  are associated with C–H bending,  $\text{CH}_3$  symmetric deformation, and C–O stretching, typical of chitosan's saccharide backbone. The peak at  $1034\text{ cm}^{-1}$  suggests C–O–C stretching vibrations, characteristic of the glycosidic linkages in chitosan, while the peak at  $862\text{ cm}^{-1}$  is attributed to skeletal vibrations of the  $\beta$ -glycosidic bond [119]. In the CS@ACAP composite (Fig. 3d), significant changes are observed in the spectrum. The broad O–H/N–H stretching band at  $3335\text{ cm}^{-1}$  remains, albeit with reduced intensity, suggesting an interaction between chitosan and the activated carbon. The C–H stretching peaks are still visible at  $2860\text{ cm}^{-1}$

and  $2328\text{ cm}^{-1}$  are still detectable, indicating the persistence of the aliphatic nature, albeit at lower transmittance values. Additionally, the carbonyl-related peak at  $1493\text{ cm}^{-1}$  implies an interaction between the amide groups of chitosan and the carbonyl groups of activated carbon, confirming the formation of the composite. The peak at  $1382\text{ cm}^{-1}$  shows a shift, indicating changes in the vibrational modes of  $\text{CH}_3$  groups, while the strong peak at  $1156\text{ cm}^{-1}$  is related to C–O stretching, like the original chitosan structure but possibly influenced by the activated carbon.

## 6.2. Scanning electron microscopy (SEM)

The scanning electron microscopy (SEM) images offer a detailed view of the surface morphologies and structural changes observed in four different materials: chitosan, avocado pits, ACAP, and a CS@ACAP composite. The SEM images of pure chitosan Fig. 4(a, b, c) reveal a smooth, uniform surface morphology with minimal porosity, characteristic of the biopolymer's natural structure. In Fig. 4(a), chitosan exhibits a layered structure with flat surfaces, showing no significant voids or roughness. The material appears compact and well-formed, with minimal internal porosity or surface irregularities. Fig. 4(b) also reveals a similarly smooth surface but with some visible cracks or fractures, suggesting a certain degree of brittleness or vulnerability to structural damage. Despite these imperfections, the surface remains relatively flat and solid. In Fig. 4(c), chitosan exhibits slight folding, imparting a fibrous or layered appearance while still maintaining the smoothness observed in the previous images [120]. The SEM images of raw avocado

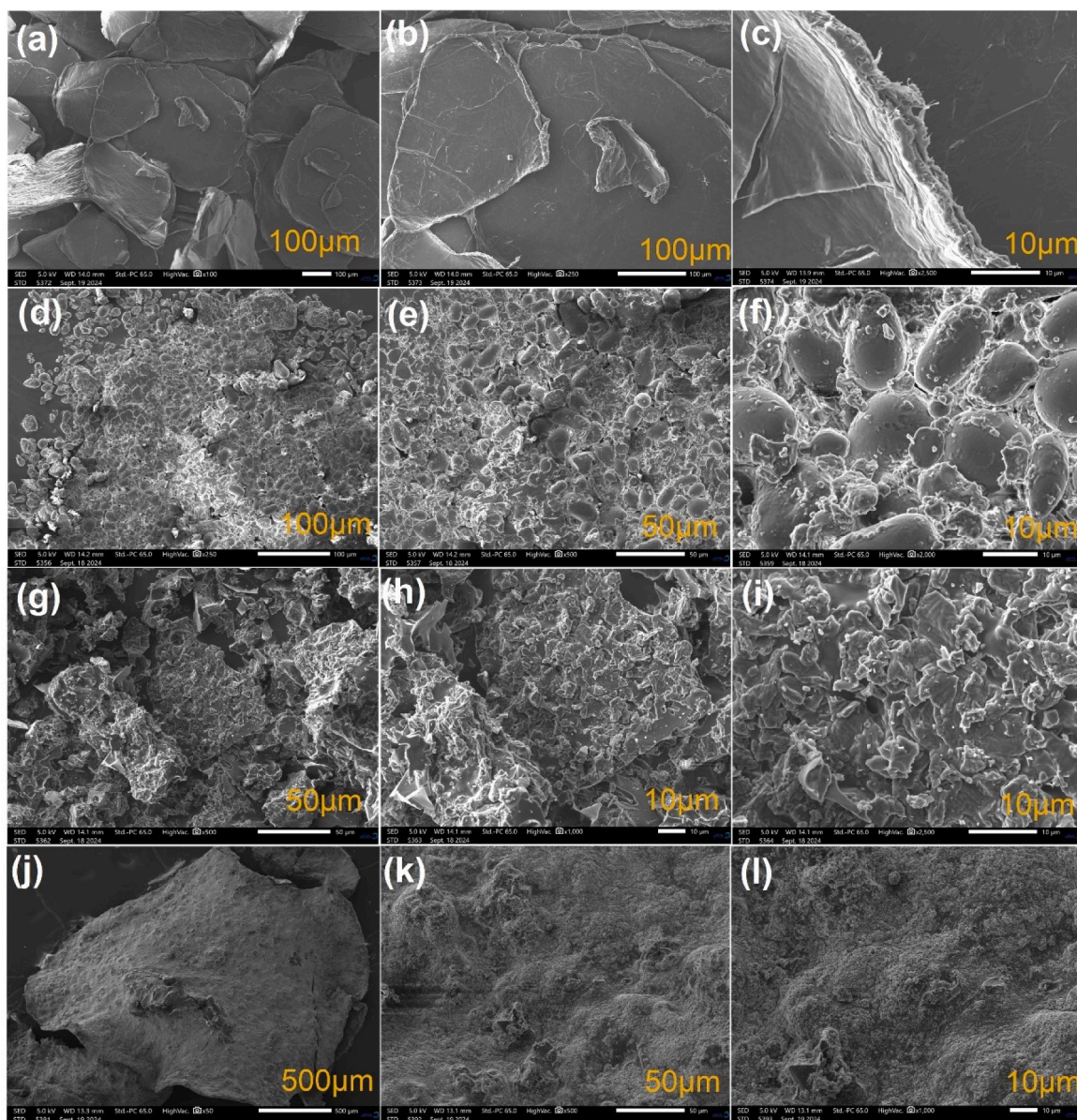


Fig. 4. SEM images of a, b,c)Chitosan, d,e,f ) Avocado pits, g,h,i) ACAP, j,k,l) CS@ACAP.

pits (Fig. 4d, e, F) reveal a rough, irregular surface morphology with visible fibrous textures, emphasizing the natural composition of the material. In Fig. 4(d), the avocado pits display a relatively dense structure, with irregular surface bumps and slight roughness, characteristic of the fibrous and cellular nature of the material. The surface texture does not display significant porosity, but there are regions where the material appears less compact, which could serve as potential sites for further processing or modification. Fig. 4(e), the avocado pits' structure shows more complexity, with some areas appearing slightly porous or granulated, suggesting a more intricate internal structure that might not be fully visible at lower magnifications. The surface remains predominantly rough and uneven, with minimal void spaces. Fig. 4(f) reveals larger cavities or voids in the material, indicating a more porous region. The SEM images of activated carbon derived from avocado pits Fig. 4 (g, h, i) show a dramatic transformation in surface morphology compared to the raw material. Fig. 4(g) presents a rough and fractured surface, with significant texture and heterogeneity, indicating the effect of the activation process [121]. This fracturing is a result of the thermal or chemical treatment used to create activated carbon, which increases the surface area and develops a more porous structure [122]. The once

compact structure of the raw avocado pits has been broken down, and voids have started to appear, signaling the creation of micro- and mesopores essential for enhancing the material's surface characteristics. In Fig. 4(h), the surface appears even more porous, with a highly irregular and complex texture that suggests a significant increase in surface area. The rough, granular appearance indicates the formation of small channels or void spaces. Fig. 4 (i) reveals a network of well-defined pores and cavities, showcasing the success of the activation process in creating a material with a high surface area and extensive pore structure. The SEM images of the CS@ACAP composite Fig. 4 (j, k, l) illustrate the successful integration of the two materials, resulting in a complex and synergistic surface morphology. Fig. 4(j), the composite shows a more compact structure than the activated carbon alone, with the smoothness of chitosan binding the activated carbon particles together. The surface still maintains some roughness, but the chitosan appears to fill in some of the voids or cracks, creating a more cohesive material. Fig. 4(k) further reveals a rough, porous texture, like the activated carbon, but with fewer large pores than in the pure activated carbon; The presence of chitosan appears to smooth out some of the larger voids, creating a more uniform surface while still allowing for the retention of smaller pores essential for

the composite's function. Finally, Fig. 4(i) displays a highly interconnected structure, where the smooth, fibrous nature of chitosan merges with the porous, granular texture of activated carbon. This composite material combines the structural integrity of chitosan with the high surface area of activated carbon, making it particularly well-suited for MB adsorption.

### 6.3. Energy dispersive X-ray spectroscopy

The Energy Dispersive X-ray Spectroscopy (EDS) analysis provides valuable insight into the elemental composition of the materials used in this study, namely chitosan, avocado pits, ACAP, and the CS@ACAP composite. The EDS spectrum of pure chitosan Fig.5(a) indicates a carbon content of 58.78 % by mass and 65.51 % by atom, with oxygen making up 41.22 % by mass and 34.49 % by atom, which is consistent with its polymeric structure rich in carbon and oxygen. For the raw avocado pits Fig.5(b), the carbon content significantly increases to 77.35 % by mass and 81.97 % by atom, while the oxygen content decreases to 22.65 % by mass and 18.03 % by atom, reflecting the natural lignocellulosic composition of the plant material. After the activation process Fig.5(c), the carbon content of the avocado pits further rises to 83.16 % by mass and 86.81 % by atom, while the oxygen content decreases to 16.84 % by mass and 13.19 % by atom, indicating the removal of volatile components and the enhancement of carbon content, a typical outcome of the carbon activation process. Finally, the composite material of chitosan with activated carbon from avocado pits Fig.5(d) shows a balanced elemental composition with 63.18 % carbon by mass and 69.56 % by atom, while oxygen increases slightly to 36.82 % by mass and 30.44 % by atom, compared to the activated carbon alone. This suggests successful integration of chitosan with the activated carbon.

### 6.4. Adsorption/desorption analysis with N<sub>2</sub> (BET)

The provided data offers a detailed comparison of the textural properties of activated carbon derived from avocado pits (ACAP) and the same material modified with chitosan (CS@ACAP), analyzed through nitrogen adsorption-desorption isotherms, pore size distribution, and BET analysis. The nitrogen adsorption-desorption isotherms (Fig. 6a) demonstrate the mesoporous nature of both materials, as they exhibit Type IV isotherms, which are typical of materials with a substantial number of mesopores (pore size range of 2–50 nm) [123]. ACAP, shows higher nitrogen adsorption capacity than CS@ACAP across the entire

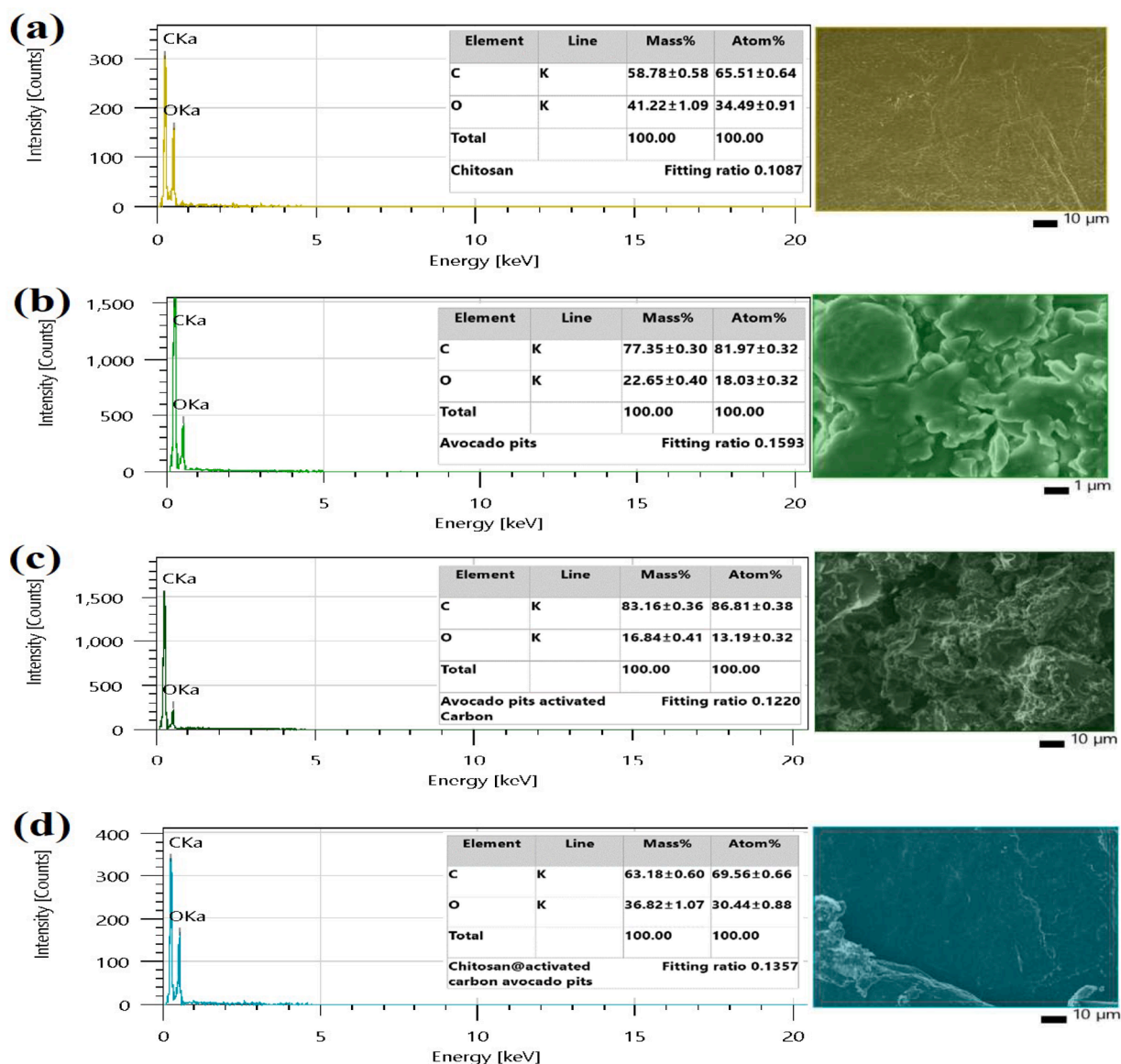


Fig. 5. EDS Spectra and Elemental Composition of: a) Chitosan, b) Avocado pits, c) ACAP, d) CS@ACAP.

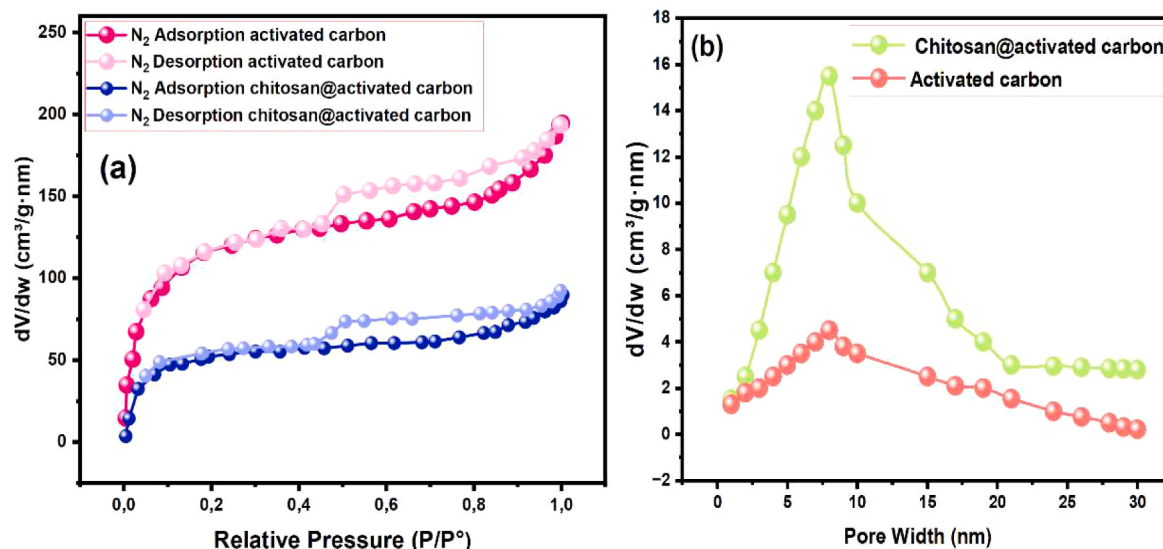


Fig. 6. a) Brunauer-Emmett-Teller (BET): nitrogen adsorption-desorption isotherms, b) pore distribution for ACAP, CS@ACAP.

range of relative pressures. This indicates that ACAP has more accessible pore volume, allowing for greater nitrogen uptake. At low relative pressures ( $P/P^\circ < 0.2$ ), the sharp rise in nitrogen adsorption for ACAP is associated with the filling of micropores, while the gradual increase at higher pressures reflects the adsorption in mesopores. The hysteresis loop seen in ACAP is more pronounced, suggesting the presence of larger mesopores where capillary condensation occurs. In contrast, CS@ACAP shows a lower nitrogen adsorption capacity, with a smaller hysteresis loop, implying that the chitosan modification reduces the volume of accessible pores, especially larger mesopores, possibly by partially blocking these pores.

The pore size distribution (Fig. 6b) provides further insights into the structural changes induced by the chitosan modification. ACAP displays a broader pore size distribution with a prominent peak around 8 nm, indicating the presence of a wide range of mesopores, including some larger mesopores beyond 10 nm. This broader distribution corresponds to the higher nitrogen uptake observed in the isotherms, confirming that ACAP contains a diverse set of pore sizes contributing to its larger pore volume.

In contrast, CS@ACAP exhibits a narrower pore size distribution, with a sharper and more pronounced peak around 8 nm. The reduction in the number of larger mesopores, coupled with the more uniform distribution of smaller mesopores, suggests that the chitosan coating alters the pore structure by eliminating or blocking larger mesopores and concentrating the remaining pores in the mesopore range. This structural modification results in a more uniform pore structure, which likely contributes to the reduced pore volume observed for CS@ACAP in the isotherms. However, despite the reduction in pore volume, the enhanced uniformity and specific pore characteristics of CS@ACAP may contribute to its superior adsorption capacity compared to ACAP.

Table 3 quantifies these observations, providing specific values for surface area, pore volume, and average pore size. CS@ACAP exhibits a significantly higher BET surface area ( $176.893 \text{ m}^2/\text{g}$ ) compared to ACAP ( $110.678 \text{ m}^2/\text{g}$ ). The increase in surface area after chitosan modification is likely due to the creation of additional surface-active sites or the exposure of previously inaccessible areas of carbon material. Despite the

**Table 3**  
Specific surface area and pore size distribution, ACAP, CS@ACAP.

Materials	BET Surface Area ( $\text{m}^2/\text{g}$ )	Pore Volume ( $\text{cm}^3/\text{g}$ )	Pore Size (nm)
ACAP	110.678	0.009012	5.98374
CS@ACAP	176.893	0.007012	4.992345

higher surface area, CS@ACAP shows a lower pore volume ( $0.007012 \text{ cm}^3/\text{g}$ ) compared to ACAP ( $0.009012 \text{ cm}^3/\text{g}$ ), which indicates that the chitosan modification reduces the overall pore capacity. This reduction in pore volume, coupled with the smaller average pore size (4.99 nm for CS@ACAP versus 5.98 nm for ACAP), suggests that the chitosan coating blocks some of the larger mesopores or narrows their openings, thus reducing the overall pore volume. The decrease in average pore size further supports the idea that chitosan primarily affects the mesopores, creating a more uniform but smaller pore structure.

### 6.5. X-ray diffraction (XRD)

The X-ray diffraction (XRD) analysis of chitosan, activated carbon from avocado pits (ACAP), and the CS@ACAP composite provides key structural insights. The XRD pattern of chitosan (Fig. 7a) displays two prominent peaks at  $9.83^\circ$  and  $21.39^\circ$ , indicating its semi-crystalline nature. The peak at  $9.83^\circ$  is attributed to the hydrated state of chitosan and intermolecular hydrogen bonding, while the peak at  $21.39^\circ$  corresponds to the amorphous regions of the polymer [124]. The

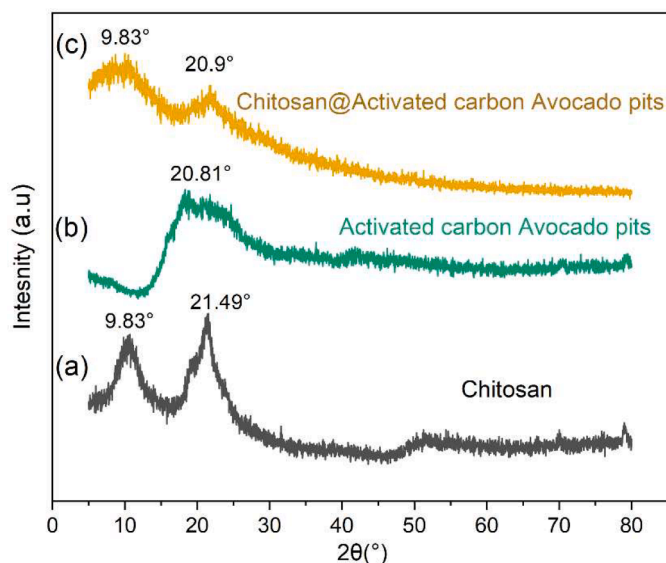


Fig. 7. XRD Spectra of a,) Chitosan CS, b) Activated carbon avocado pits ACAP, c) Chitosan@ Activated carbon avocado pits CS@ACAP.

**Table 4**  
ANOVA Analysis for Methylene Blue Removal (MB).

Source	Sum of Squares	Df	Mean Square	F-value	p-value
Model	8131.08	9	903.45	435.60	< 0.0001
A-H <sub>2</sub> SO <sub>4</sub>	4345.45	1	4345.45	2095.15	< 0.0001
B-Time of Activation	2065.64	1	2065.64	995.94	< 0.0001
C-Temperature	1016.55	1	1016.55	490.13	< 0.0001
AB	93.80	1	93.80	45.23	0.0003
AC	29.05	1	29.05	14.01	0.0072
BC	106.50	1	106.50	51.35	0.0002
A <sup>2</sup>	68.60	1	68.60	33.07	0.0007
B <sup>2</sup>	48.28	1	48.28	23.28	0.0019
C <sup>2</sup>	317.87	1	317.87	153.26	< 0.0001
Residual	14.52	7	2.07		
Lack of Fit	14.09	3	4.70	43.87	0.0016
Pure Error	0.4282	4	0.1071		
Cor Total	8145.60	16			

activated carbon from avocado pits (ACAP) (Fig. 7b) exhibits a broad diffraction peak around 20.81°, indicating its predominantly amorphous structure, typical of disordered carbon materials with weak graphitic ordering. In the CS@ACAP composite (Fig. 7c), the XRD pattern displays two broad peaks: one at 9.83°, similar to pure chitosan, and another at 20.90°, slightly shifted from the ACAP peak. This pattern confirms the successful coating of chitosan onto the carbon surface, with the peak shift suggesting a mild interaction between chitosan and the carbon matrix. The broadness of the peaks in the composite indicates that the structure remains primarily amorphous, with some contributions from the semi-crystalline regions of chitosan.

## 7. Optimization results

### 7.1. Analysis of variance (ANOVA)

The analysis of variance (ANOVA) results valuable insights into the influence of various factors on the response variable, demonstrating a statistically significant relationship between the independent variables and the outcome of interest. Table 4 shows that the model demonstrates a total sum of squares of 8145.60, with a remarkably low residual sum of squares of 14.52, suggesting that the model effectively captures a substantial portion of the variance in the data. The overall F-value of 435.60, accompanied by a p-value of <0.0001 [125], confirms the significance of the model itself, indicating that at least one of the factors or their interactions has a meaningful impact on the response variable. Focusing on the individual factors, sulfuric acid concentration (A) emerges as the most significant variable, with a sum of squares of 4345.45, an F-value of 2095.15, and a p-value of <0.0001. This finding underscores the critical role that sulfuric acid concentration plays in shaping the outcome, suggesting that variations in its level can lead to significant changes in the response variable. Similarly, activation time (B) shows a significant effect, with an F-value of 995.94 and a p-value of <0.0001. Temperature (C) also demonstrates a notable influence, with an F-value of 490.13 and a corresponding p-value of <0.0001. These results collectively highlight the importance of these factors in the overall process under investigation. Additionally, the interaction effects between these factors provide deeper insights into the system's

**Table 5**  
statistical parameters and model performance for the removal of Methylene Blue.

Std. Dev.	1.44	R <sup>2</sup>	0.9982
Mean	48.16	Adjusted R <sup>2</sup>	0.9959
C.V. %	2.99	Predicted R <sup>2</sup>	0.9722
		Adeq Precision	73.6985

complexity. Notably, the interaction between sulfuric acid concentration and activation time (AB) is significant, with an F-value of 45.23 and a p-value of 0.0003, suggesting that the combined effects of these two factors are crucial for understanding the response variable. Similarly, the interactions between sulfuric acid concentration and temperature (AC), and between activation time and temperature (BC), are significant, with F-values of 14.01 and 51.35, respectively, and p-values indicating strong interaction effects. The quadratic effects of these factors, represented by A<sup>2</sup>, B<sup>2</sup>, and C<sup>2</sup>, also make substantial contributions to the model, with p-values of <0.0001, 0.0019, and 0.0001, respectively. This suggests that not only do the linear effects of the factors influence the response variable, but their squared effects also play a critical role in determining the outcome, highlighting potential nonlinear relationships within the data. Additionally, the residual analysis reveals a lack of fit, with an F-value of 43.87 and a p-value of 0.0016, indicating that while the model is significant, there may be some unexplained variability.

The statistical summary, as illustrated in Table 5, indicates a strong fit to the data, as evidenced by the R<sup>2</sup> value of 0.9982. This high R<sup>2</sup> value suggests that approximately 99.82 % of the variability in the response variable can be explained by the independent variables and their interactions included in the model [89]. Additionally, the adjusted R<sup>2</sup> value of 0.9959 further reinforces the model's robustness by accounting for the number of predictors, indicating that the model remains reliable even with the inclusion of multiple factors. The mean of the response variable is 48.16, providing a central tendency around which the data points are clustered. The standard deviation of 1.44 reflects a relatively low variability within the dataset, which, in conjunction with a coefficient of variation (C.V. %) of 2.99, indicates that the data points are tightly grouped around the mean. This low C.V. further confirms the precision of the measurements, and the consistency of the data collected. The predicted R<sup>2</sup> value of 0.9722 suggests that the model has good predictive capabilities, meaning it can accurately predict responses for new observations not included in the model fitting [126]. Finally, the Adequate Precision value of 73.6985 indicates an excellent signal-to-noise ratio, demonstrating that the model is suitable for navigating the design space effectively.

Eq. (16) for methylene blue (MB) removal efficiency (%) demonstrates the influence of three key factors: H<sub>2</sub>SO<sub>4</sub> concentration (A), activation time (B), and activation temperature (C). The constant value of 40.58 represents the baseline MB removal when all variables are at zero. A negative coefficient for H<sub>2</sub>SO<sub>4</sub> concentration indicates that increasing acid concentration leads to a decrease in MB removal efficiency. In contrast, the positive coefficients for activation time and activation temperature suggest that both factors enhance MB removal. The interaction terms (AB, AC, BC) show that the combined effects of these variables also contribute to the overall removal, with positive values indicating synergies. Furthermore, the quadratic terms for each variable (A<sup>2</sup>, B<sup>2</sup>, C<sup>2</sup>) demonstrate nonlinear effects, particularly for temperature (C<sup>2</sup> = 8.69), which has the strongest positive influence on MB removal at higher levels.

$$\text{MBRemoval}(\%) = 40.58 + -23.3063A + 16.0687B + 11.2725C + 4.8425AB + 2.695AC + 5.16BC + 4.03625A^2 + 3.38625B^2 + 8.68875C^2 \quad (16)$$

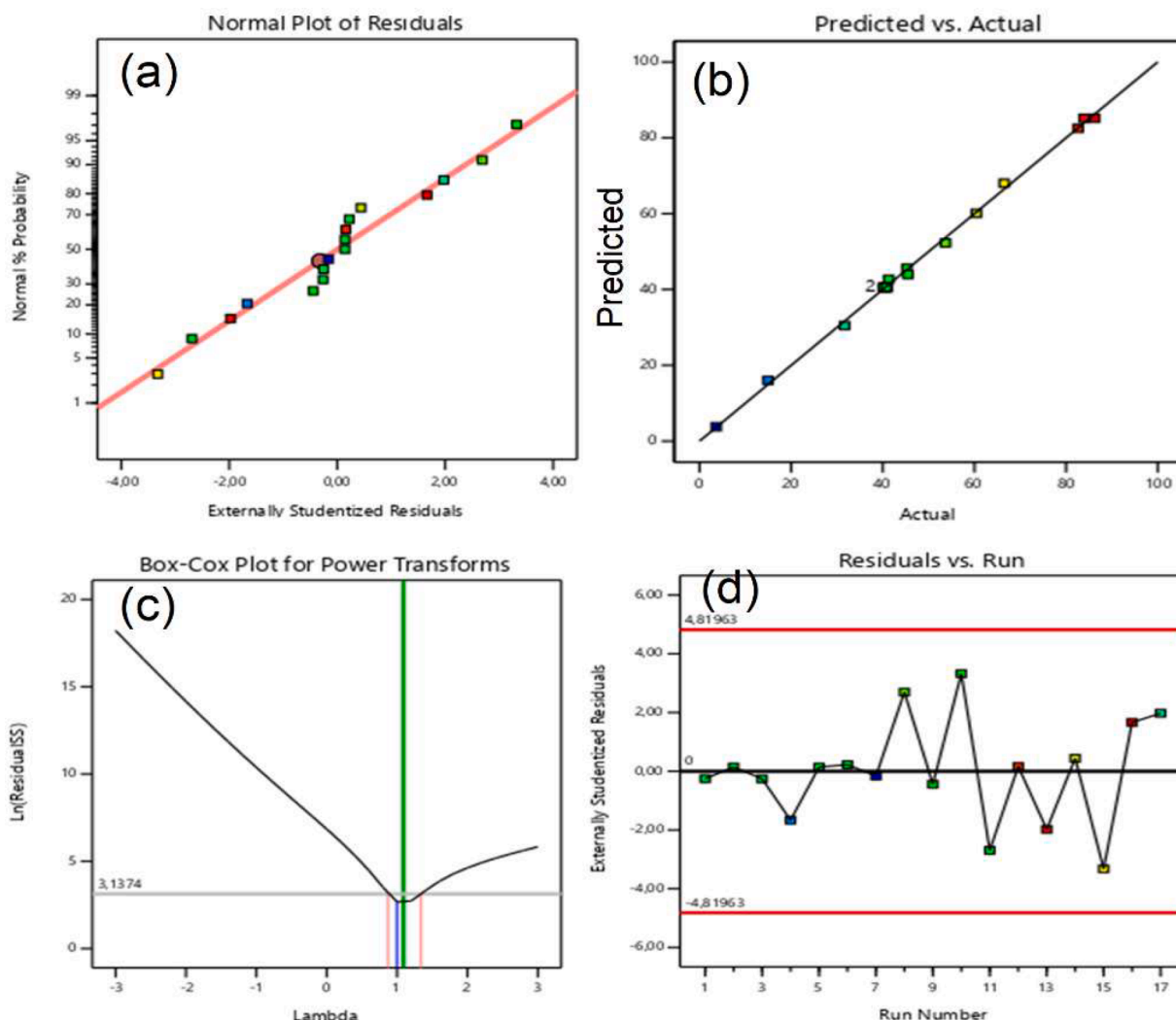


Fig. 8. a) Normal Plot of Residuals, b) Residuals vs. Run, c) Box-Cox Plot for Power Transforms, d) Predicted vs. Actual.

## 7.2. Normal probability plot of residuals

The analysis of the regression model's performance includes several diagnostic plots that assess the adequacy and reliability of the model. Fig. 8a The Normal Plot of Residuals shows that the residuals are approximately normally distributed, as indicated by their close alignment with the red diagonal line, a key assumption in regression analysis [127]. Fig. 8b The Residuals vs. Run plot indicates no systematic bias, with residuals fluctuating around zero and remaining within the acceptable limits, suggesting effective modeling without evidence of autocorrelation. Fig. 8c The Box-Cox plot aids in identifying the optimal power transformation to stabilize variance and enhance normality, revealing an optimal  $\lambda$  value of approximately 1.3174 for minimizing the residual sum of squares (RSS). Lastly, Fig. 8d the Predicted vs. Actual plot illustrates a strong correlation between predicted values and actual observations, with points closely clustered around the diagonal line, indicating the model effectively captures the underlying relationships in the data.

## 7.3. Response surface analysis and contour plot

The 3D surface plots illustrate the interaction effects of sulfuric acid

concentration ( $\text{H}_2\text{SO}_4$ ), activation time, and temperature on Methylene Blue (MB) removal, each exhibiting distinct trends. In Fig. 9(a), the interaction between sulfuric acid concentration (A) and activation time (B) demonstrates contrasting effects. As  $\text{H}_2\text{SO}_4$  concentration increases, MB removal decreases, suggesting that higher acid concentrations may negatively affect the adsorption capacity, potentially due to over-etching or surface damage at elevated acid levels. However, as activation time increases, MB removal improves significantly, indicating that longer activation times facilitate the development of surface properties conducive to MB adsorption. This trend is reinforced by the contour plot, which shows the highest MB removal occurring at lower acid concentrations combined with longer activation times.

Fig. 9(b) explores the interaction between  $\text{H}_2\text{SO}_4$  concentration (A) and activation temperature (C), revealing similar trends regarding the acid's negative effect on MB removal. As  $\text{H}_2\text{SO}_4$  concentration rises, MB removal decreases, indicating that excessive acid treatment may reduce the adsorbent's efficiency. Conversely, activation temperature exhibits a positive correlation with MB removal. As temperature increases, MB removal improves, suggesting that higher activation temperatures enhance the material's porosity or surface activity, facilitating better adsorption. The contour plot clearly demonstrates that higher temperatures favor MB removal, particularly when combined with lower acid concentrations.

Fig. 9(c) represents the interaction between activation time (B) and activation temperature (C), with both factors positively influencing MB

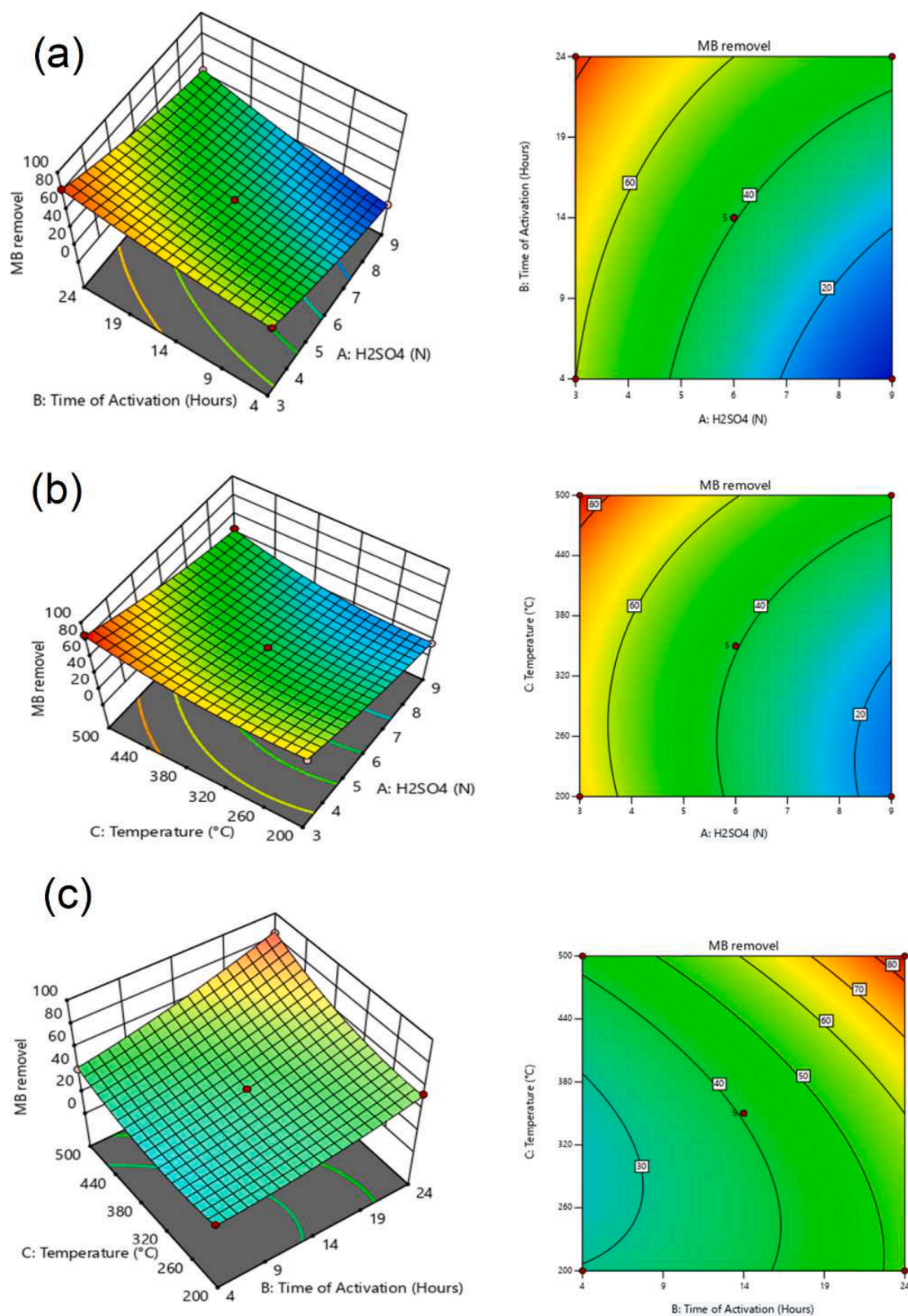


**Fig. 9.** 3D Surface Plots of Methylene Blue Removal (MB), (a) Influence of Activation Time and  $\text{H}_2\text{SO}_4$  Concentration on MB Removal, (b) Effect of Temperature and  $\text{H}_2\text{SO}_4$  Concentration on MB Removal, (c) Interaction Between Temperature and Activation Time for MB Removal.

removal. As activation time increases, MB removal efficiency improves, suggesting that prolonged activation enhances the adsorbent's properties. Similarly, increasing activation temperature further enhances MB removal, indicating that higher temperatures improve surface activation

and adsorption efficiency. The combined effect of longer activation times and higher temperatures results in the highest MB removal rates, as reflected in both the surface and contour plots.

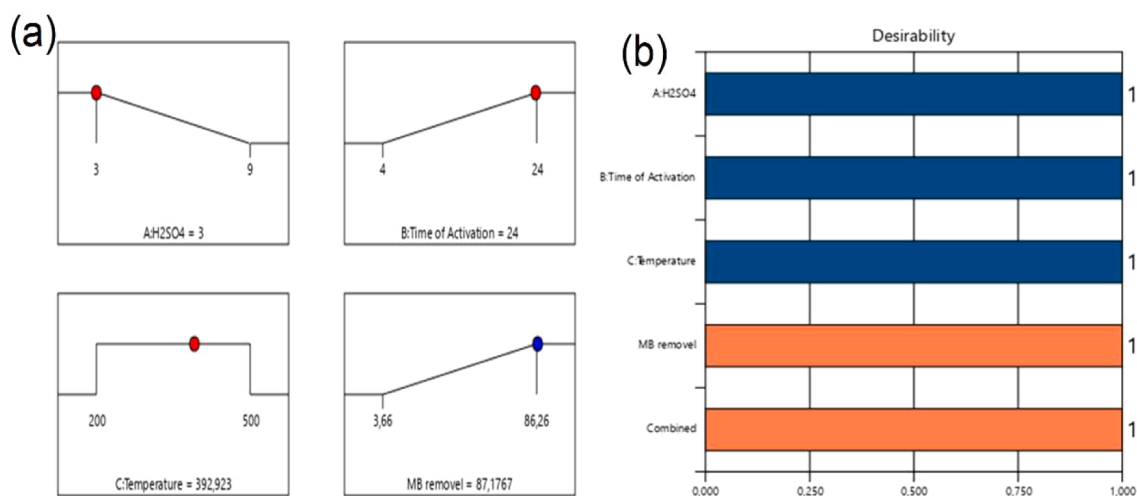


Fig. 10. (a) optimization of parameters ,(b)the desirability plot.

#### 7.4. Optimization desirability function

The figures Fig. 10(a,b), and Fig. 12 represent an integrated approach to optimizing methylene blue (MB) removal from a solution, utilizing the Box-Behnken Design (BBD) methodology with three critical factors: H<sub>2</sub>SO<sub>4</sub> concentration (A), activation time (B), and temperature (C). Each factor's effect is clearly illustrated in the response plots of Fig. 10(a), where the individual influence of these parameters on MB removal is visualized. The plots show that an H<sub>2</sub>SO<sub>4</sub> concentration of 3 (N), activation time of 24 h, and temperature of 392.923 °C are the most favorable conditions, resulting in an MB removal efficiency of 87.1767 %. The red dots pinpoint the optimal values for each factor, emphasizing how these conditions contribute to the effective removal of the dye. In Fig. 10(b), the desirability plot highlights the optimization's success, with each factor receiving a desirability score of 1. This perfect score indicates that the chosen levels of H<sub>2</sub>SO<sub>4</sub> concentration, activation time, and temperature combine to provide the best possible outcome for MB removal, maximizing the performance of the process. The combined desirability is also marked at 1, further confirming the effectiveness of these optimized parameters. Fig. 11 presents 3D cube plots, visually depicting both the desirability and the predicted MB removal outcomes. In the desirability cube, the optimal conditions are represented by a high desirability of 1 at the central region of the design space, showing how the parameter combination maximizes desirability. The MB removal cube demonstrates that under the same conditions, a predicted removal

efficiency of 87.1767 % is achieved. These visualizations reinforce that the optimization process was successful in identifying the best conditions for MB removal, with a strong agreement between the predicted results and the actual experimental desirability.

## 8. Adsorption study

### 8.1. Effect of contact time

Fig. 12 shows the Methylene Blue (MB) removal efficiency over time for both activated carbon from avocado pits (ACAP) and CS@ACAP. Initially, the adsorption rate for both materials is rapid, especially during the first 40 min. This can be attributed to the high availability of active sites on the surface of the adsorbents, which facilitates efficient MB adsorption [128]. During this phase, MB molecules readily bind to the free adsorption sites, leading to a sharp increase in removal efficiency. As time progresses, the adsorption rate slows for both materials as the active sites become increasingly occupied, and the system approaches equilibrium. For the CS@ACAP composite, this slowdown occurs after reaching nearly 100 % MB removal around 120 min, whereas for avocado pits activated carbon, the process continues more gradually, stabilizing at around 80 % MB removal after 180 min. This slower phase reflects the decreasing availability of active sites and the difficulty for MB molecules to access the remaining unoccupied sites [129].

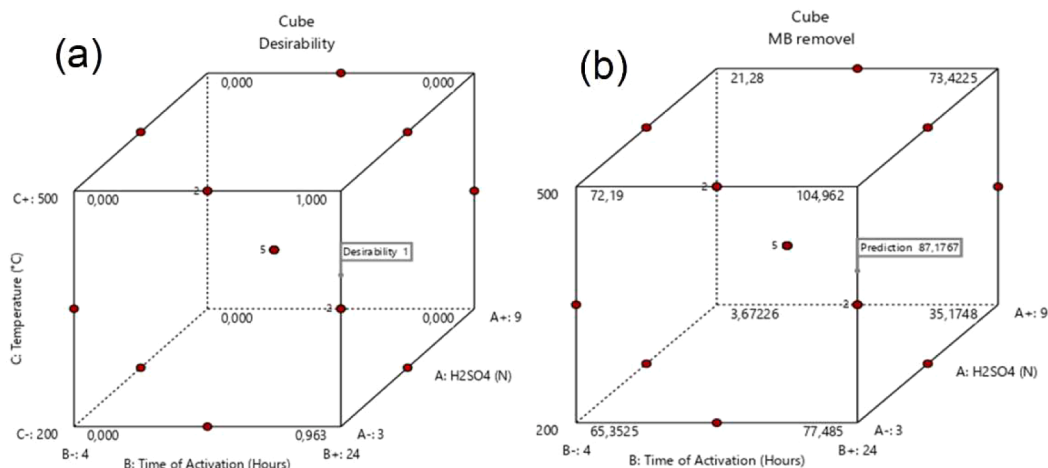


Fig. 11. 3D cube plots.

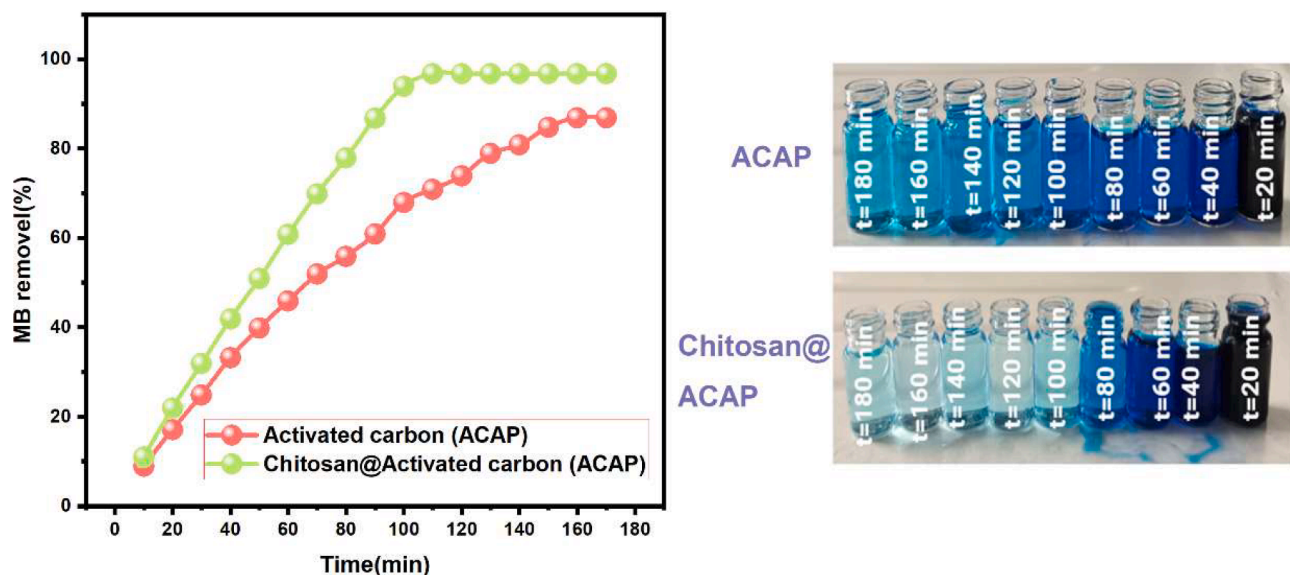


Fig. 12. Effect of Contact Time on MB Removal.

8.2. Modeling of adsorption kinetic

The adsorption kinetics of methylene blue (MB) onto activated carbon from avocado pits (ACAP) and the chitosan@activated carbon composite (CS@ACAP) were thoroughly examined using two prominent kinetic models: the pseudo-first-order and pseudo-second-order models. These models were chosen based on their ability to describe different types of adsorption mechanisms, and their application is crucial for understanding the nature of the adsorption process and the interactions between the adsorbate (MB) and the adsorbent (ACAP and CS@ACAP). As illustrated in Fig. 13 and summarized in Table 6, both models were applied to the experimental data, and their fitting results provided critical insights into the adsorption mechanisms, as well as the suitability of these models to describe the adsorption process. The pseudo-first-order kinetic model, developed by Lagergren, is commonly used to describe adsorption processes where the rate of adsorption is assumed to be proportional to the difference between the equilibrium adsorption capacity and the amount adsorbed at any given time. This model assumes that the adsorption sites are homogeneously distributed across

Table 6

Kinetic parameters for MB adsorption.

Kinetic Model	Pseudo-First-Ordre			Pseudo-Second-Ordre		
	$R^2$	$k_1$ ( $\text{min}^{-1}$ )	$q_{e,the}$ (mg/g)	$R^2$	$k_2$ (g/mg·min)	$q_{e,the}$ (mg/g)
ACAP	0.905	0.02175	66.87	0.964	0.0000421	106.5
CS@ACAP	0.8544	0.03222	87.54	0.983	00,000,668	289.9

the adsorbent surface and that the process is mainly driven by physical interactions between the adsorbate and the adsorbent. When applied to the adsorption of MB onto ACAP and CS@ACAP, the fitting results revealed important characteristics of the adsorption kinetics. For ACAP, the  $R^2$  value was found to be 0.905, indicating that the pseudo-first-order model could reasonably describe the adsorption kinetics, but with some limitations. On the other hand, for CS@ACAP, the  $R^2$  value was slightly lower at 0.8544, suggesting that while the pseudo-first-

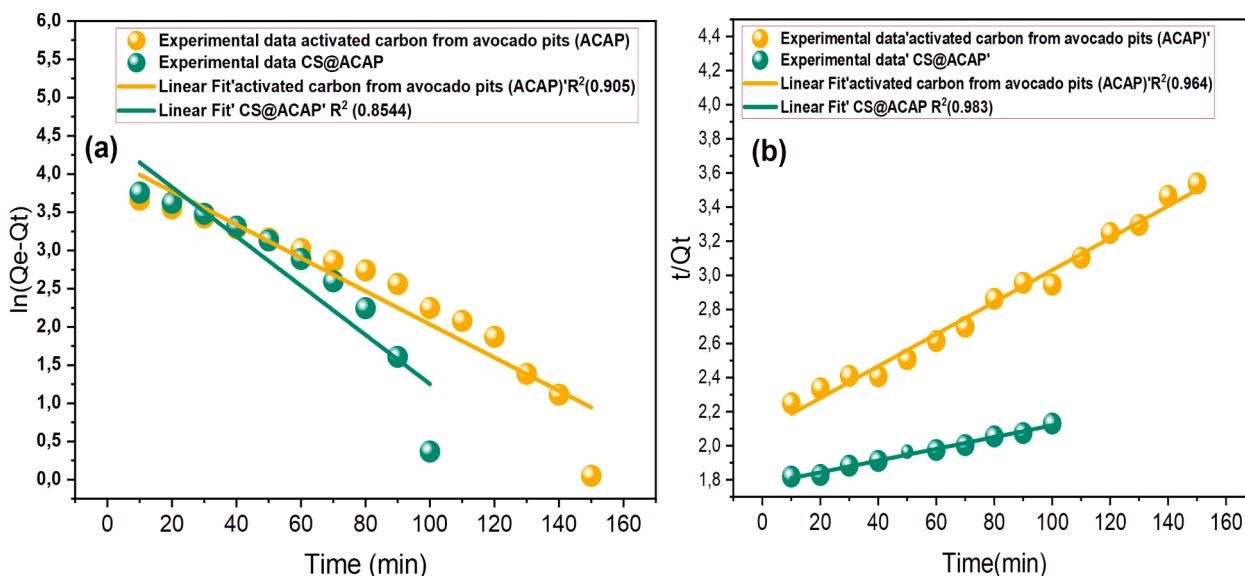


Fig. 13. (a) Pseudo-first-order model (b) Pseudo-second-order model for BM Removal.

order model captured the general trend of the adsorption process, it was less effective in accurately fitting the experimental data for the composite adsorbent. These relatively moderate  $R^2$  values point to the fact that the pseudo-first-order model is not the most suitable model for describing the adsorption of MB onto both ACAP and CS@ACAP, especially for the composite material, where additional interactions between the dye and functional groups on the chitosan surface may be influencing the adsorption process. Further analysis of the rate constant ( $k_1$ ) and equilibrium adsorption capacity ( $q_e$ ) values for the pseudo-first-order model, as presented in Table 6, provided additional information on the adsorption behavior of the two adsorbents. For ACAP, the  $q_e$  value was determined to be 66.87 mg/g, while for CS@ACAP, the  $q_e$  value was higher at 75.54 mg/g. These values indicate that the composite adsorbent (CS@ACAP) has a higher equilibrium adsorption capacity than ACAP, likely due to the enhanced surface area and functional groups introduced by the chitosan component. Additionally, the  $k_1$  values indicated that CS@ACAP exhibited a faster initial adsorption rate ( $0.03222 \text{ min}^{-1}$ ) compared to ACAP ( $0.02175 \text{ min}^{-1}$ ), suggesting that CS@ACAP may have a higher affinity for MB at the early stages of adsorption. However, the moderate  $R^2$  values and the deviation from the experimental data highlight that the pseudo-first-order model is less suitable for accurately modeling the adsorption kinetics, particularly for CS@ACAP. In contrast, the pseudo-second-order kinetic model, which is often employed to describe chemisorption processes where the rate of adsorption is governed by the chemical interaction between the adsorbate and adsorbent, provided a much better fit to the experimental data. The pseudo-second-order model assumes that the adsorption rate is proportional to the square of the difference between the equilibrium adsorption capacity and the amount adsorbed at any given time. This model is particularly effective when the adsorption involves chemisorption, such as electron sharing or transfer between the adsorbent and adsorbate, and is more applicable for systems where the adsorption capacity increases significantly with time. As shown in Fig. 13(b), the linear fits for both ACAP and CS@ACAP to the pseudo-second-order model exhibited much higher  $R^2$  values, with  $R^2 = 0.964$  for ACAP and  $R^2 = 0.983$  for CS@ACAP. These high  $R^2$  values suggest that the pseudo-second-order model provides an excellent description of the adsorption kinetics for both adsorbents, and it is a far superior fit compared to the pseudo-first-order model. This indicates that the adsorption of MB onto both ACAP and CS@ACAP is likely governed by chemisorption processes, where the interaction between the MB molecules and the adsorbent surface involves chemical bonds rather than purely physical forces. The superior fit of the pseudo-second-order model was further confirmed by the analysis of the equilibrium adsorption capacity ( $q_e$ ) and rate constant ( $k_2$ ) values, as shown in Table 6. For the pseudo-second-order model, the  $q_e$  value for CS@ACAP was significantly higher (289.9 mg/g) compared to ACAP (106.5 mg/g), indicating that CS@ACAP exhibits a much higher adsorption capacity for MB. This suggests that the composite adsorbent, likely due to its higher surface area and the presence of functional groups from chitosan, facilitates more efficient adsorption. Furthermore, the  $k_2$  values for the pseudo-second-order model were also higher for CS@ACAP ( $0.0000668 \text{ g/mg}\cdot\text{min}$ ) than for ACAP ( $0.0000421 \text{ g/mg}\cdot\text{min}$ ), indicating that the composite adsorbent also achieves faster adsorption rates, further supporting the notion that CS@ACAP is a more efficient adsorbent for MB removal. The improved fit of the pseudo-second-order model, along with the higher adsorption capacity and faster adsorption rate observed for CS@ACAP, suggests that the adsorption process is not only more efficient but also governed by a more complex mechanism, likely involving chemisorption, where electron transfer or sharing between the adsorbate and adsorbent plays a critical role. The choice of the pseudo-first-order and pseudo-second-order models is justified based on the nature of the adsorption process. The pseudo-first-order model was initially applied because it is widely used to describe adsorption processes where the adsorption rate is proportional to the difference between the equilibrium adsorption capacity and the amount adsorbed over time.

However, the pseudo-first-order model is generally more suited for physical adsorption processes and may not account for the complex interactions that occur in chemisorption. Given the higher  $R^2$  values obtained for the pseudo-second-order model and the substantial differences in adsorption capacities for ACAP and CS@ACAP, it is clear that the adsorption of MB onto both adsorbents is more accurately described by the pseudo-second-order model, which accounts for the chemical nature of the interactions involved. This suggests that the adsorption of MB onto both ACAP and CS@ACAP is governed by a chemisorption process, likely involving strong interactions between the dye molecules and the adsorbent surfaces, including electrostatic forces, hydrogen bonding, and potentially  $\pi$ - $\pi$  interactions. The better fit of the pseudo-second-order model and the higher adsorption capacities observed for CS@ACAP further emphasize the potential of this composite material as an effective adsorbent for MB removal in wastewater treatment applications, where enhanced adsorption performance is critical.

### 8.3. Effect of mass

Fig. 14 highlights the impact of adsorbent mass on the efficiency of methylene blue (MB) removal for both avocado pit-activated carbon (ACAP) and the chitosan-based composite CS@ACAP. The results indicate that increasing the adsorbent mass enhances the removal efficiency for both materials, though their optimal masses differ. Specifically, the CS@ACAP composite exhibits a steep increase in MB removal efficiency, achieving nearly complete removal ( $\approx 100\%$ ) at an optimal mass of 0.08 g. This behavior is attributed to the composite's improved surface characteristics and the presence of additional active sites contributed by chitosan. However, beyond this optimal mass, further increases in adsorbent mass yield diminishing returns, as the active sites become saturated, reducing the availability of binding sites for MB molecules [88]. Essentially, once the available binding sites are fully occupied, the addition of more adsorbent leads to a diminishing return on removal efficiency, as excess adsorbent cannot increase the number of available sites. In contrast, the avocado pits activated carbon (pink squares) shows a more gradual increase in MB removal efficiency. While its performance improves with increasing mass, the optimal removal is achieved at a higher mass of 0.12 g, where it also approaches maximum removal efficiency. This difference in optimal mass suggests that the activated carbon derived from avocado pits requires a larger quantity to reach similar removal efficiency as the composite. The CS@ACAP composite, due to its improved surface area and active sites, achieves optimal adsorption at a lower mass, indicating higher adsorption efficiency.

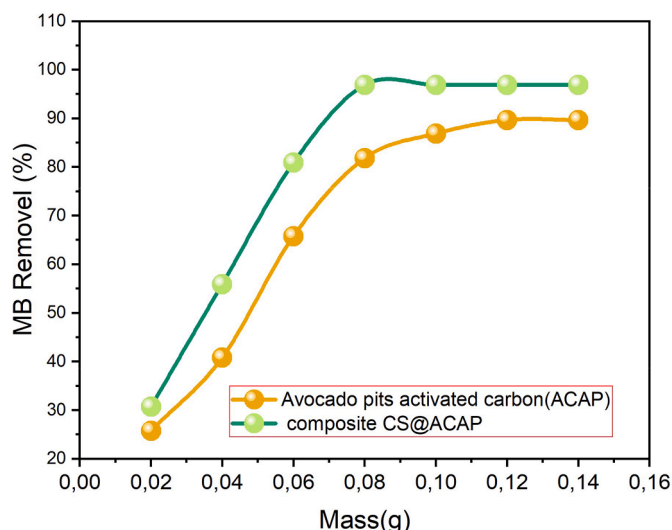


Fig. 14. Effect of Mass on MB Removal.

After the optimal mass for both materials is reached, the removal efficiency plateaus, signifying that most MB molecules have been adsorbed, and additional mass does not contribute significantly to further removal because the remaining unoccupied sites become fewer, and the likelihood of MB molecules finding these sites diminishes [130].

#### 8.4. Effect of pH and point of zero charge (pH<sub>pzc</sub>)

The adsorption behavior of Methylene Blue (MB) on activated carbon derived from avocado pits and the CS@ACAP composite was strongly influenced by the pH of the solution in relation to the point of zero charge (pH<sub>pzc</sub>) of each adsorbent [131]. The pH<sub>pzc</sub> is a critical parameter that determines whether the surface of the adsorbent will carry a positive or negative charge at a given pH, which, in turn, affects its ability to absorb charged molecules such as MB. Fig. 15(a) shows that the pH<sub>pzc</sub> of the material before activation was found to be 5.2, which served as a reference point, though its adsorption performance was not evaluated across different pH levels. The focus of the study was on the activated carbon (pH<sub>pzc</sub> = 3.96) and CS@ACAP composite (pH<sub>pzc</sub> = 5.4).

Fig. 15b shows that at pH values lower than the pH<sub>pzc</sub> of each material, the adsorbent surfaces are positively charged, leading to electrostatic repulsion between the positively charged MB molecules and the adsorbent surface. This reduces adsorption efficiency, as observed at lower pH values, where both activated carbon and CS@ACAP exhibit reduced MB removal. For instance, at pH 2, the removal efficiency was relatively low for both activated carbon ACAP (50.89 %) and CS@ACAP (61.78 %) due to the dominant positive charge on the adsorbent surfaces. As the pH increases and exceeds the pH<sub>pzc</sub>, the surface charge of the adsorbents becomes negative, allowing electrostatic attraction between the negatively charged adsorbent surface and the positively charged MB molecules [131]. This leads to a marked increase in adsorption efficiency. For activated carbon, this transition occurs at pH values above 3.96, while for CS@ACAP, it occurs above 5.4. The adsorption efficiency increases significantly as the pH rises, with the highest removal percentages achieved at pH 10, where CS@ACAP removed 98.78 % of MB, compared to 90.78 % for activated carbon. This enhanced performance of CS@ACAP can be attributed to the presence of additional functional groups, such as amino and hydroxyl groups from chitosan, which further contribute to the adsorption capacity by providing more active sites for interaction with MB. The behavior of the adsorbents across different pH values underscores the importance of surface charge in adsorption processes. At pH values below the pH<sub>pzc</sub>,

the adsorbents are less effective due to electrostatic repulsion, but at pH values above the pH<sub>pzc</sub>, adsorption efficiency is significantly improved due to electrostatic attraction.

#### 8.5. Effect of concentration

The influence of initial methylene blue (MB) concentration on removal efficiency was thoroughly investigated using both avocado pits activated carbon and CS@ACAP composite as illustrated in Fig. 16. At lower concentrations, specifically within the range of 25 to 50 mg/L, both adsorbents exhibited remarkable removal efficiencies, nearing 100 %. This high efficiency at lower concentrations suggests that the available adsorption sites on the surfaces of both materials were ample enough to accommodate most of the MB molecules present. However, as the initial concentration of MB increased, a noticeable decline in removal efficiency was observed for both adsorbents. The avocado pits activated carbon demonstrated a significant reduction in performance, with removal efficiency plummeting to approximately 35–40 % at an initial concentration of 200 mg/L. This decline indicates that the adsorption sites on the activated carbon surface became saturated and were unable to effectively capture MB molecules at elevated concentrations [132]. In contrast, the CS@ACAP composite exhibited superior performance throughout the concentration range, maintaining higher removal efficiencies compared to its pure counterpart. At an initial concentration of 100 mg/L, the composite achieved around 75 % removal efficiency, while the pure activated carbon only managed about 60 %. Even at the highest concentration tested (200 mg/L), the composite retained an efficiency of approximately 50 %, significantly outperforming the 30 % efficiency recorded for the activated carbon alone. The enhanced adsorption capacity of the CS@ACAP composite can be attributed to the presence of chitosan, which not only introduces additional functional groups but also provides more active adsorption sites, enabling the composite to effectively capture a greater number of MB molecules even as the concentration increases.

#### 8.6. Modeling of adsorption isotherms

The adsorption behavior of activated carbon derived from avocado pits (ACAP) and chitosan-modified activated carbon (CS@ACAP) was extensively studied using two well-known adsorption models: the Langmuir and Freundlich isotherms. These models provide a deeper understanding of the interaction between the adsorbents and methylene blue (MB) dye molecules in aqueous solutions. The experimental results,

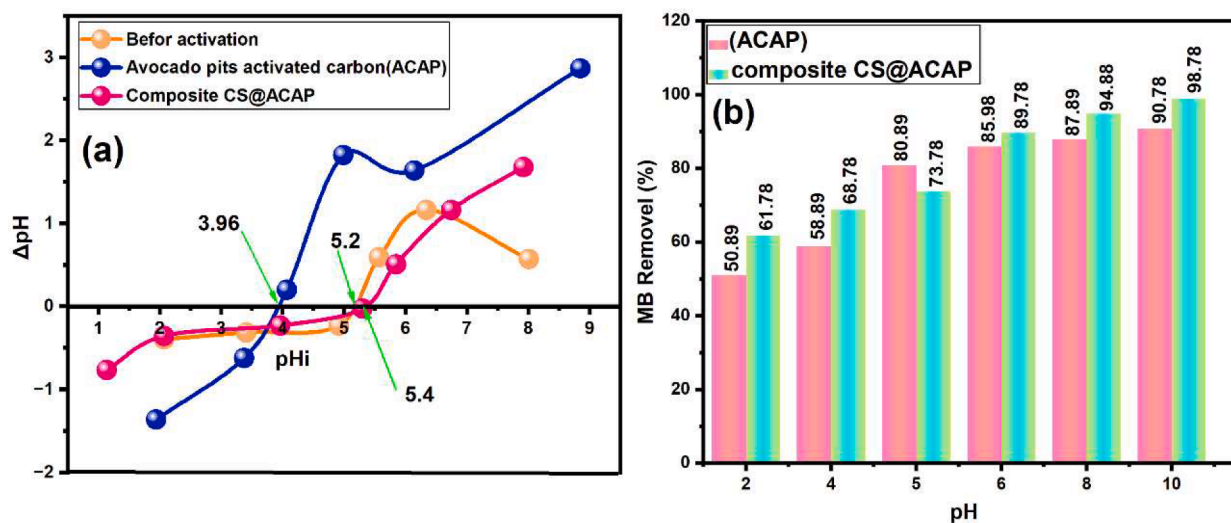


Fig. 15. a) Determination of the point of zero charge (pH<sub>pzc</sub>) for avocado pits before activation, activated carbon avocado pits (ACAP), chitosan@ activated carbon avocado pits (CS@ACAP), b) effect of pH.

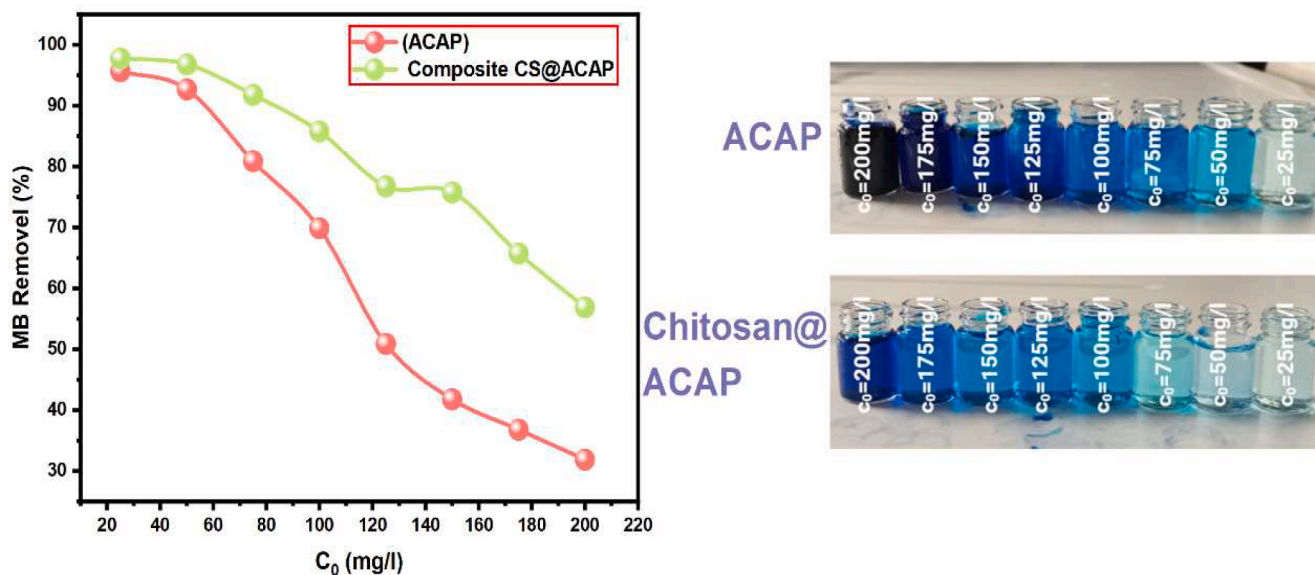


Fig. 16. Effect of concentration of MB.

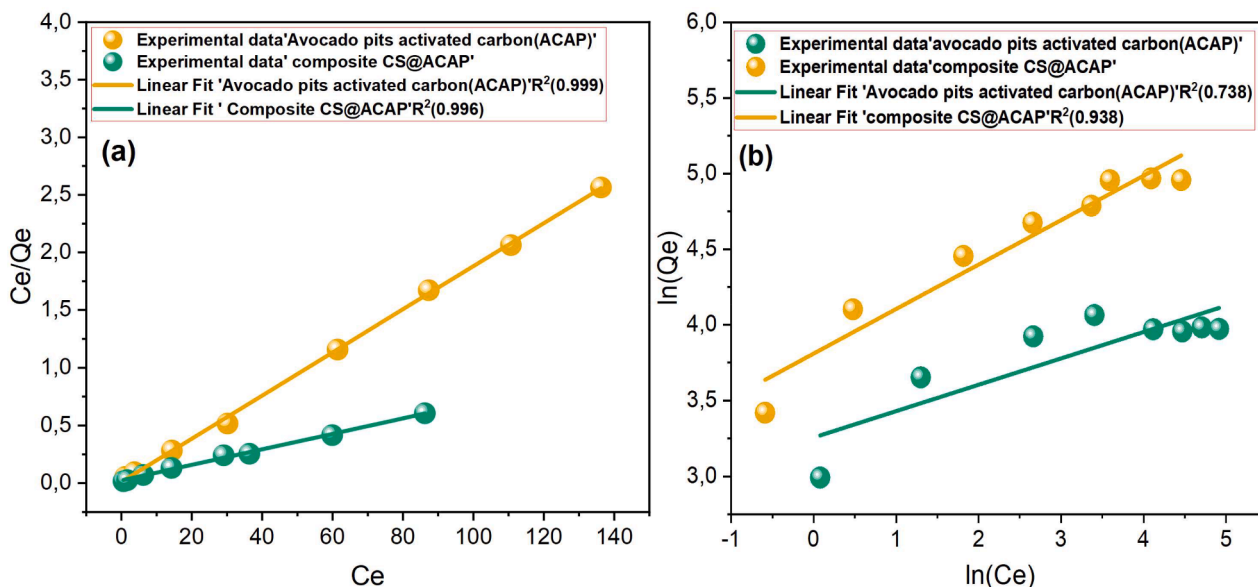


Fig. 17. a) Langmuir and b) Freundlich Isotherm Models for MB Adsorption.

**Table 7**  
Parameters for Langmuir and Freundlich Isotherm Models for MB Adsorption.

Adsorbents	Langmuir			Freundlich		
	Qm(mg/g)	K <sub>i</sub> (L/mg)	R <sup>2</sup>	K <sub>F</sub> (mg·g <sup>-1</sup> )	1/n <sub>F</sub>	R <sup>2</sup>
ACAP	40.2	3.71	0.999	25.98	0.1738	0.738
CS@ACAP	81.0	0.661	0.996	45.3	0.2939	0.938

as illustrated in Fig. 17a and b and summarized in Table 7, reveal critical insights into the efficiency, mechanisms, and characteristics of both adsorbents in removing MB from contaminated water. The Langmuir isotherm model assumes adsorption occurs on a surface that is energetically uniform, where each adsorption site is identical and capable of holding only one molecule of the adsorbate. Both ACAP and CS@ACAP show excellent fits to the Langmuir model, with R<sup>2</sup> values of 0.999 and 0.996, respectively. These high R<sup>2</sup> values suggest that the adsorption

process for both adsorbents is predominantly monolayer, with adsorption sites on both materials being uniformly distributed. The high R<sup>2</sup> values indicate minimal to no significant interaction between adsorbed molecules, which aligns with the assumption of independent adsorption sites in the Langmuir model. A key parameter for evaluating the performance of an adsorbent is the maximum adsorption capacity (Q<sub>m</sub>), which represents the amount of MB that can be adsorbed onto a unit mass of adsorbent at saturation. The Q<sub>m</sub> for CS@ACAP is 81.0 mg/g, which is more than double the Q<sub>m</sub> of ACAP, which is 40.2 mg/g. This stark difference suggests that the modification of activated carbon with chitosan significantly enhances its adsorption capacity. The increased Q<sub>m</sub> for CS@ACAP can be attributed to the additional functional groups introduced by chitosan, such as amino (-NH<sub>2</sub>) and hydroxyl (-OH) groups. These groups not only increase the number of active sites available for adsorption but also create favorable conditions for the interaction with MB molecules, thereby improving the overall efficiency of the adsorption process. Although CS@ACAP exhibits a superior

adsorption capacity, the Langmuir constant ( $K_L$ ), which quantifies the adsorption energy or affinity between the adsorbent and the adsorbate, is higher for ACAP (3.71 L/mg) than for CS@ACAP (0.661 L/mg). This discrepancy suggests that the unmodified activated carbon has a stronger affinity for MB molecules per site, implying that the adsorbent-material interaction is more intense at each individual site on ACAP compared to CS@ACAP. The lower  $K_L$  value for CS@ACAP may reflect that, while it can adsorb a larger quantity of MB, the strength of each interaction is somewhat weaker than the unmodified activated carbon, which might have a greater electrostatic attraction for MB molecules at each binding site. The Freundlich isotherm, on the other hand, assumes that adsorption occurs on a heterogeneous surface, where adsorption sites differ in energy, and the number of active sites increases with an increase in adsorbate concentration. The fit to the Freundlich model provides additional insights into the nature of the adsorbent surface. For ACAP, the fit to the Freundlich model is moderate, with an  $R^2$  value of 0.738, indicating a somewhat less pronounced heterogeneity in the adsorbent's surface. This is in contrast to CS@ACAP, which shows a significantly better fit to the Freundlich model ( $R^2 = 0.938$ ), suggesting that the introduction of chitosan has altered the surface properties of the activated carbon, making it more heterogeneous. The incorporation of chitosan likely introduces various functional groups that create distinct types of adsorption sites, contributing to a more complex and varied adsorption behavior. The Freundlich constant ( $K_F$ ) represents the adsorption capacity in the context of the Freundlich model, and a higher  $K_F$  indicates a stronger ability of the adsorbent to hold the adsorbate. The  $K_F$  for CS@ACAP (45.3 mg/g) is significantly higher than that for ACAP (25.98 mg/g), further supporting the conclusion that CS@ACAP has a superior adsorption capacity. This finding is consistent with the results obtained from the Langmuir analysis. Moreover, the adsorption intensity, denoted by the term  $1/nF$ , indicates the favorability of the adsorption process. A lower value of  $1/nF$  corresponds to stronger adsorption, while a higher value indicates weaker adsorption. For CS@ACAP,  $1/nF$  is 0.2939, which is notably higher than that of ACAP (0.1738), suggesting that adsorption is more favorable on CS@ACAP. This higher value reflects the greater heterogeneity of the surface due to chitosan, which allows for better interactions with the MB molecules. These models of both the Langmuir and Freundlich isotherms reveals that CS@ACAP, with its significantly higher maximum adsorption capacity and superior fit to both models, is a more efficient adsorbent compared to ACAP. The enhanced adsorption capacity of CS@ACAP can be attributed to the modification with chitosan, which not only increases the number of active adsorption sites but also introduces additional functional groups that improve the adsorbent's ability to interact with and adsorb MB molecules. The higher  $K_F$  value and the better fit to the Freundlich model further emphasize the advantages of CS@ACAP, suggesting that its heterogeneous surface with diverse adsorption sites plays a critical role in enhancing the efficiency of MB removal. While the Langmuir constant ( $K_L$ ) for ACAP is higher, indicating a stronger per-site affinity, the overall performance, as indicated by the higher  $Q_m$ , is far superior for CS@ACAP.

The adsorption performance of materials is significantly influenced by their structural characteristics, such as surface area, pore volume, and pore size distribution. In this study, we compared the adsorption capacities of activated carbon (ACAP) and the chitosan-modified composite (CS@ACAP) to evaluate how modifications in their structure affect their ability to adsorb pollutants. The BET surface area of CS@ACAP (176.893 m<sup>2</sup>/g) is significantly higher than that of ACAP (110.678 m<sup>2</sup>/g), indicating a larger number of available adsorption sites. A higher surface area allows for increased interaction with pollutants, leading to enhanced adsorption. Additionally, although ACAP has a higher pore volume (0.009012 cm<sup>3</sup>/g) than CS@ACAP (0.007012 cm<sup>3</sup>/g), the smaller pore size of CS@ACAP (4.99 nm) compared to ACAP (5.98 nm) is a crucial factor in improving adsorption. Smaller pores in CS@ACAP help facilitate more controlled diffusion of the adsorbate molecules, leading to more efficient adsorption within the material.

Moreover, the presence of functional groups introduced by chitosan modification, such as amine and hydroxyl groups, further enhances the composite's ability to adsorb pollutants. These structural modifications improve the adsorption kinetics and increase the material's affinity for the adsorbate, resulting in a higher maximum adsorption capacity ( $Q_m$ ) for CS@ACAP (81.0 mg/g) compared to ACAP (40.2 mg/g). Thus, the combination of a larger surface area, optimized pore structure, and additional functional groups contributes to the superior adsorption capacity of CS@ACAP.

### 8.7. Temperature effect

Fig. 18 shows the influence of temperature on Methylene Blue (MB) removal efficiency using activated carbon derived from avocado pits (ACAP) and its composite with chitosan (C@ACAP). For ACAP, the MB removal decreases as the temperature rises, dropping from 95.67 % at 25 °C to 90.78 % at 55 °C, suggesting an exothermic adsorption process where higher temperatures weaken physical interactions such as van der Waals forces [133]. Conversely, the C@ACAP composite shows an increase in removal efficiency, improving from 97.89 % at 25 °C to 99.89 % at 55 °C, indicating a likely endothermic process or enhanced binding site activity at elevated temperatures.

### 8.8. Thermodynamic study

The Van't Hoff plot (Fig. 19) for methylene blue (MB) adsorption onto avocado pits carbon and CS@ACAP reveals distinct thermodynamic behaviors for both materials. The linear fit for avocado pits carbon ( $R^2 = 0.994$ ) in Table 8 indicates an exothermic adsorption process with a calculated enthalpy change ( $\Delta H^\circ$ ) of  $-22.1$  kJ/mol. The negative entropy change ( $\Delta S^\circ = -50.23$  J/mol.K) implies that the adsorption decreases system disorder [134], typical for physical adsorption. The Gibbs free energy ( $\Delta G^\circ$ ) values are negative at all tested temperatures, confirming that the process is spontaneous, becoming more favorable as temperature increases [135]. In contrast, the adsorption onto CS@ACAP shows a less pronounced linear fit ( $R^2 = 0.895$ ) with an endothermic enthalpy change ( $\Delta H^\circ = 78.14$  kJ/mol). The positive entropy change ( $\Delta S^\circ = 292.58$  J/mol.K) suggests a more disordered system, likely due to the complex interactions between MB and the composite material [136]. Despite the endothermic nature, the process remains spontaneous at all tested temperatures, with  $\Delta G^\circ$  becoming increasingly negative as temperature rises, reflecting the enhanced favorability of MB adsorption

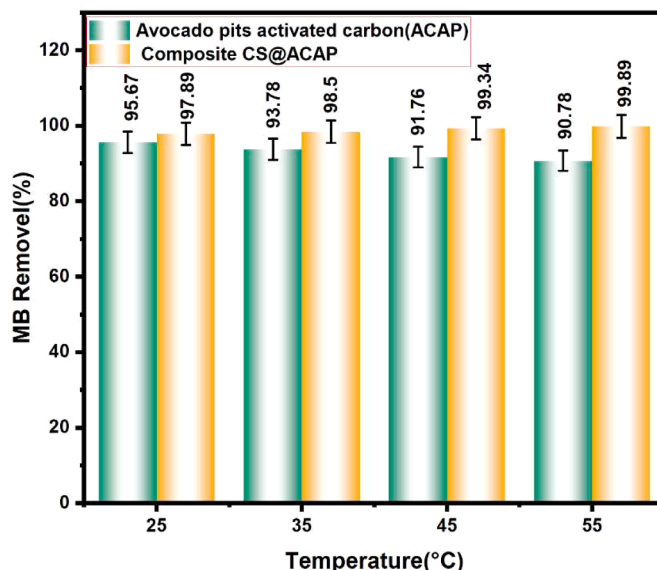


Fig. 18. Effect of Temperature on the Removal Efficiency of MB.

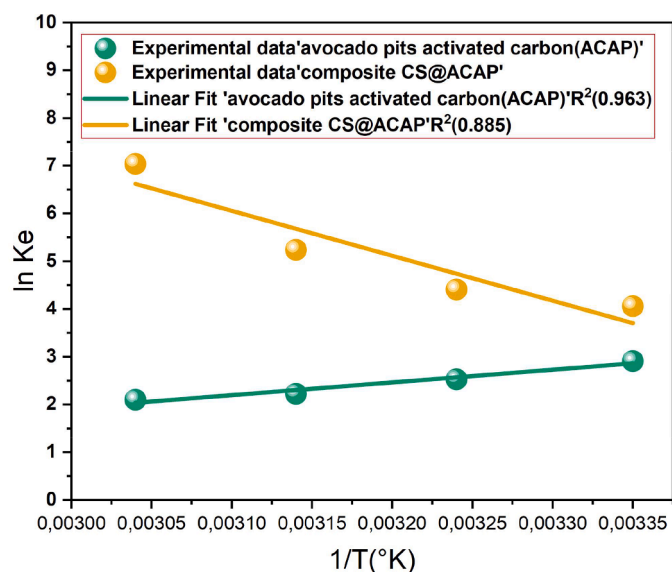


Fig. 19. Van't Hoff Plot for the Adsorption of MB.

Table 8  
Thermodynamic Parameters for the Adsorption of MB.

$\Delta H^\circ$ (kJ mol <sup>-1</sup> )	$\Delta S^\circ$ (J mol <sup>-1</sup> K <sup>-1</sup> )	$\Delta G^\circ$ (kJ mol <sup>-1</sup> )		
		298 K	308 K	318 K
-22.1	-50.23	-7.13	-6.63	-6.13
78.14	292.58	-9.05	-11.97	-14.90

onto the composite at higher temperatures [137].

## 9. DFT analysis

### 9.1. Global reactivity descriptions

The Density Functional Theory (DFT) calculations provide critical insights into the electronic properties of the studied adsorbents and their interactions with methylene blue (MB), particularly through the analysis of the Highest Occupied Molecular Orbital (HOMO) and the Lowest Unoccupied Molecular Orbital (LUMO) energies. The energy gap ( $E_g$ ), which is the difference between HOMO and LUMO energies, is a key parameter that determines the reactivity, stability, and adsorption potential of the materials. A larger  $E_g$  signifies higher stability and lower reactivity, while a smaller  $E_g$  indicates enhanced electronic interactions, making the material more suitable for adsorption processes. Chitosan, with a relatively wide energy gap of 5.28 eV, demonstrates significant stability and resistance to electronic deformation, which makes it structurally robust but less reactive on its own for MB adsorption indicating strong molecular stability and weak electronic reactivity [138]. This stability, however, is advantageous when combined with more reactive materials. The highly negative HOMO energy (-5.98 eV) suggests that chitosan has a limited ability to donate electrons, while its relatively high LUMO energy (-0.70 eV) means it is not highly favorable for electron acceptance either. This explains why chitosan alone does not exhibit significant electronic interactions in adsorption. However, its functional groups, such as hydroxyl (-OH) and amino (-NH<sub>2</sub>) groups, contribute to adsorption through hydrogen bonding and electrostatic interactions rather than electron transfer mechanisms [139]. Activated carbon (ACAP) presents the smallest energy gap ( $E_g = 0.66$  eV), which suggests exceptional electronic reactivity. The HOMO at -4.76 eV and LUMO at -4.10 eV imply that ACAP is highly efficient in electron transfer processes, facilitating strong charge-transfer interactions with pollutants like MB. The  $\pi$ -conjugated system of ACAP allows for  $\pi$ -

stacking interactions with aromatic molecules, further enhancing its adsorption capabilities. However, the small energy gap also means that ACAP is less chemically stable compared to chitosan, making it more prone to electronic fluctuations [140], which is crucial for binding Methylene Blue molecules through mechanisms such as  $\pi$ - $\pi$  stacking interactions and electrostatic attraction. The synergy between these materials becomes most apparent in the composite systems.

Methylene blue (MB), a cationic dye, demonstrates a much smaller energy gap ( $E_g = 1.15$  eV), with a HOMO energy of -4.37 eV and a LUMO energy of -3.22 eV. The small energy gap signifies that MB is highly reactive and can readily participate in electron transfer processes. The relatively high HOMO energy means MB can easily donate electrons, while the LUMO value indicates its ability to accept electrons, making it an excellent candidate for adsorption through charge transfer interactions with suitable adsorbents.

For instance, The CS@ACAP composite exhibits an increased energy gap ( $E_g = 1.00$  eV) compared to ACAP alone, indicating that the introduction of chitosan enhances stability while slightly reducing reactivity. The HOMO (-4.76 eV) and LUMO (-3.76 eV) values suggest that while the composite retains ACAP's strong electron transfer capabilities, chitosan's functional groups contribute additional adsorption mechanisms, such as hydrogen bonding and electrostatic interactions [141]. The CS@MB composite has a significantly higher energy gap ( $E_g = 2.17$  eV) than MB alone, indicating enhanced stability but reduced electronic reactivity. The HOMO energy (-5.57 eV) suggests weaker electron-donating ability, while the LUMO energy (-3.40 eV) means MB's electron-accepting capacity is slightly diminished. This demonstrates that chitosan incorporation stabilizes the system but does not significantly hinder MB's adsorption efficiency, as alternative mechanisms like hydrogen bonding still contribute [142]. The ACAP@MB system exhibits a small energy gap ( $E_g = 1.10$  eV), slightly higher than MB alone but still indicative of high reactivity. The HOMO (-4.74 eV) and LUMO (-3.64 eV) values suggest that ACAP effectively interacts with MB via charge transfer and  $\pi$ - $\pi$  stacking interactions, maintaining strong adsorption efficiency. Finally, the CS@ACAP@MB composite has the same energy gap as MB ( $E_g = 1.15$  eV), showing that while the composite retains MB's electronic properties, it benefits from the structural and functional enhancements provided by chitosan and ACAP. The HOMO (-4.37 eV) and LUMO (-3.22 eV) values confirm that the material remains highly reactive and well-suited for adsorption applications.

Fig. 20, Table 9

### 9.2. Characteristics of global reactivity

Table 10 presents key quantum chemical parameters that provide deep insights into the reactivity, electronic properties, and adsorption potential of the studied materials, including chitosan (CS), methylene blue (MB), activated carbon derived from avocado pits (ACAP), and their various composites. These parameters hardness ( $\eta$ ), softness ( $S$ ), chemical potential ( $\mu$ ), electronegativity ( $\chi$ ), electrophilicity ( $\omega$ ), and total charge transfer capacity ( $\Delta N_{max}$ ) are essential in understanding the interactions that govern the adsorption of MB onto the synthesized adsorbents. Hardness ( $\eta$ ) and softness ( $S$ ) are inversely related properties that describe the material's resistance to deformation and its chemical reactivity, respectively. A high hardness value indicates a rigid and less reactive structure, whereas higher softness implies greater flexibility and higher reactivity, which is often favorable for adsorption. Among the studied materials, chitosan exhibits a relatively high hardness (2.64) and low softness (0.38), suggesting that it is structurally stable but less reactive compared to other materials in the study. Its chemical potential (-3.34) and electronegativity (3.34) indicate a moderate ability to accept electrons, while its electrophilicity (14.73) is relatively high, suggesting that it can interact with electron donors such as MB. However, the total charge transfer ( $\Delta N_{max}$ ) value for chitosan (1.27) is comparatively low, indicating that while chitosan can adsorb MB, the

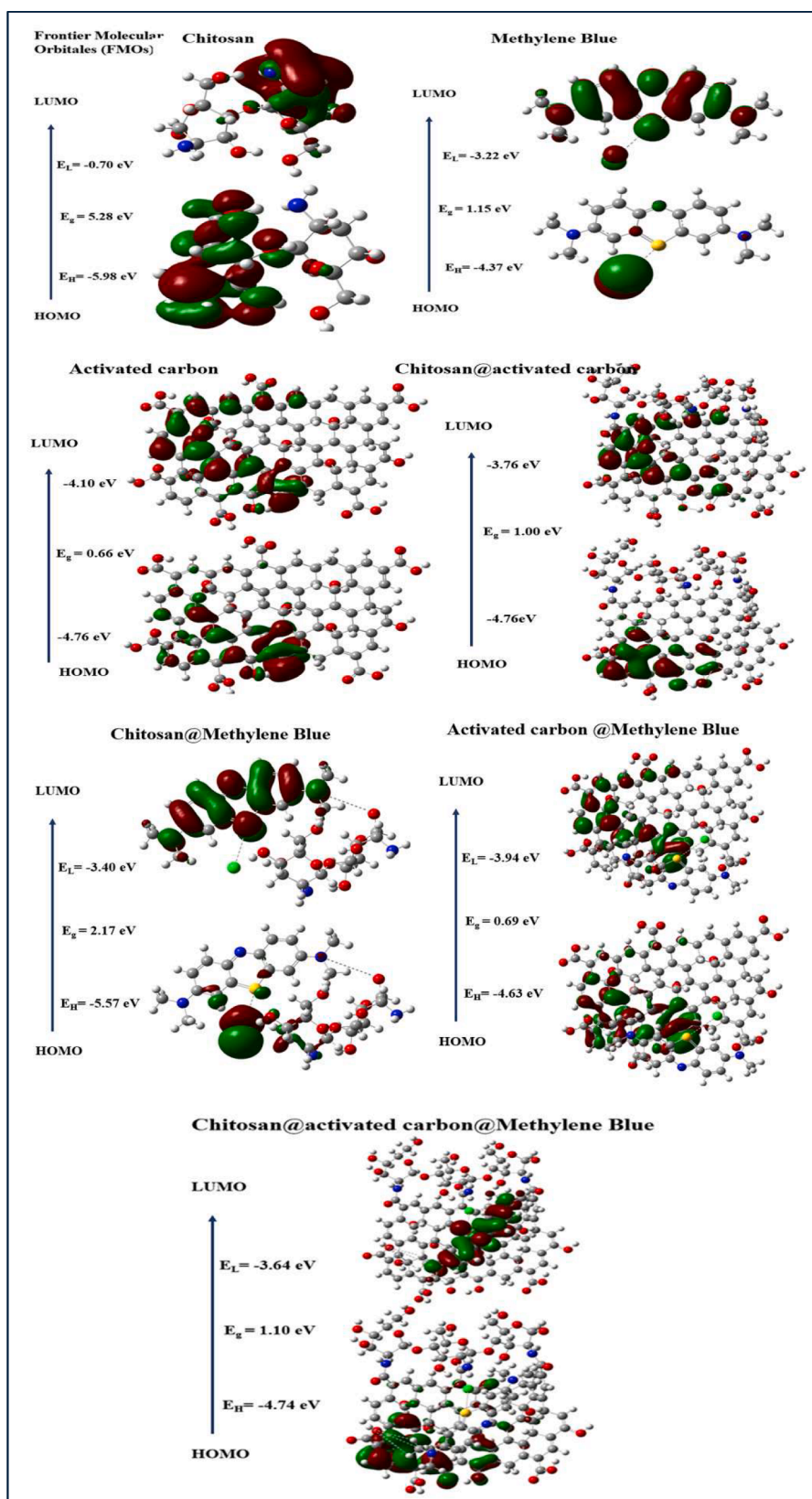


**Fig. 20.** Energy Profile and HOMO-LUMO Analysis of Chitosan (CS), Methylene Blue (MB), activated carbon (ACAP), chitosan@activated carbon (CS@ACAP), chitosan@Methylene blue (CS@MB), Activated carbon@Methylene blue (ACAP@MB), chitosan@activated carbon@Methylene Blue (CS@ACAP@MB).

**Table 9**

Electronic Properties and Energy Gap Values CS, MB, ACAP, CS@ACAP, CS@MB, ACAP @MB, CS@ACAP@MB.

Name of the Molecules	HOMO (eV)	LUMO (eV)	Eg (eV)
CS	-5.98	-0.70	5.28
MB	-4.37	-3.22	1.15
	-4.76	-4.10	0.66
CS@ACAP	-4.76	-3.76	1.00
CS@MB	-5.57	-3.40	2.17
ACAP @MB	-4.74	-3.64	1.10
CS@ACAP@MB	-4.37	-3.22	1.15

extent of electron exchange during the interaction is modest [143]. In contrast, MB itself exhibits significantly lower hardness (0.575) and higher softness (1.74), reflecting a more flexible and reactive molecular structure [144]. Its more negative chemical potential (-3.79) suggests a greater tendency to donate electrons, while its electronegativity (3.79) and moderate electrophilicity (4.14) support its ability to establish strong interactions with electron-accepting adsorbents [145]. Activated carbon derived from avocado pits (ACAP) stands out as an exceptionally effective adsorbent, with remarkably low hardness (0.33) and high softness (3.03), indicating superior reactivity. Its chemical potential (-4.43) highlights its strong electron-donating ability, and its high electronegativity (4.43) further confirms its strong interaction potential with MB molecules. Furthermore, ACAP's large total charge transfer capacity (13.42) suggests that it engages in extensive charge exchange with MB, reinforcing its effectiveness as an adsorbent. The combination of chitosan and activated carbon in the CS@ACAP composite results in a material with intermediate hardness (0.5) and increased softness (2), indicating a synergistic effect where the structural stability of chitosan is maintained while enhancing the reactivity contributed by activated carbon. The chemical potential (-4.26) and higher electrophilicity (4.54) indicate that CS@ACAP has a strong tendency to accept electrons, thereby improving its adsorption capabilities. Its total charge transfer capacity (8.52) is significantly higher than that of pure chitosan, supporting its enhanced adsorption efficiency. The CS@MB composite, formed by the interaction of chitosan with MB, exhibits increased hardness (1.085) and reduced softness (0.92), reflecting a balanced structure that retains some stability while allowing reactivity. Notably, its higher electrophilicity (10.91) suggests a strong ability to accept electrons from MB molecules, and its total charge transfer capacity (4.13) supports effective adsorption, likely facilitated through electrostatic interactions and hydrogen bonding between chitosan's functional groups and MB. Similarly, the ACAP@MB composite demonstrates a hardness of 0.55 and softness of 1.82, reflecting a structure that optimally balances stability and reactivity for effective MB adsorption. Its chemical potential (-4.19) and total charge transfer capacity (7.62) suggest that it can efficiently facilitate electron exchange with MB, contributing to enhanced adsorption efficiency. Finally, the CS@ACAP@MB composite integrates the properties of chitosan, activated carbon, and MB, resulting in a material with intermediate hardness (0.575) and softness (1.743), offering a structure that is stable yet highly reactive. Its chemical potential (-3.79) and electronegativity (3.79) confirm its ability to interact effectively with MB, while the total charge transfer capacity (6.6) suggests substantial electron exchange,

**Table 10**

Calculate the physical characteristics of CS, MB, ACAP, CS@ACAP, CS@MB, ACAP @MB, CS@ACAP@MB.

Name of the Molecules	$\eta$ (hardness)	S (softness)	$\mu$ (chemical potential)	$\chi$ (electronegativity)	$\omega$ (electrophilicity)	$\Delta N_{max}$ (total charge transfer)
CS	2.64	0.38	-3.34	3.34	14.73	1.27
MB	0.575	1.74	-3.79	3.79	4.14	6.6
ACAP	0.33	3.03	-4.43	4.43	3.24	13.42
CS@ACAP	0.5	2	-4.26	4.26	4.54	8.52
CS@MB	1.085	0.92	-4.49	4.49	10.91	4.13
ACAP @MB	0.55	1.82	-4.19	4.19	4.83	7.62
CS@ACAP@MB	0.575	1.743	-3.79	3.79	4.14	6.6

reinforcing its capability for efficient MB adsorption. These collectively indicate that the electronic properties of the studied materials play a crucial role in governing the adsorption mechanism of MB, with softer and more reactive materials generally exhibiting stronger adsorption potentials. The incorporation of activated carbon into the composite materials significantly enhances their reactivity and charge transfer capacity, thereby optimizing the adsorption process. By analyzing these quantum parameters, a more comprehensive understanding of the adsorption mechanism is achieved, demonstrating how electronic structure influences the efficiency of dye removal from aqueous solutions.

### 9.3. MEP geometries

Fig.21 provides a detailed comparison of the optimized molecular structures and Molecular Electrostatic Potential (MEP) maps for Chitosan, Methylene Blue, Activated Carbon, and their combinations, specifically in the adsorption of Methylene Blue. The first row presents Chitosan, a naturally occurring biopolymer known for its biocompatibility and high adsorption capacity. Its optimized structure shows the presence of multiple hydroxyl and amine groups, which are potential active sites for adsorption [146]. The corresponding MEP map for Chitosan reveals negatively charged regions, particularly around the oxygen and nitrogen atoms, indicating areas that are likely to interact with positively charged species like Methylene Blue [147].

In the second row, Methylene Blue is depicted with its planar structure, which is common for aromatic dyes. Its MEP map highlights regions of positive electrostatic potential, making it prone to interaction with negatively charged adsorbent surfaces [148]. This is crucial, as it helps explain how Methylene Blue can be adsorbed onto materials like Chitosan and Activated Carbon due to its charge distribution. Activated Carbon, is a highly porous material known for its exceptional surface area and adsorption efficiency [149]. Its optimized structure shows a stable carbon network, while the MEP map indicates a widespread distribution of negative charge, confirming its ability to attract and adsorb positively charged Methylene Blue molecules.

In the fourth row, the composite material Chitosan@Activated Carbon is analyzed, showing the combined structural features of both Chitosan and Activated Carbon. The MEP map for this composite indicates a balanced distribution of both negative and neutral charge regions, suggesting enhanced adsorption properties compared to the individual materials. This combination leverages the high surface area of Activated Carbon and the functional groups of Chitosan, creating a more effective adsorbent for Methylene Blue. The final row presents Chitosan@Methylene Blue, showing the interaction between Chitosan and Methylene Blue directly. The MEP map for this system reveals complex charge distributions, where the positive regions of Methylene Blue are likely interacting with the negative sites on Chitosan. This implies that Chitosan can serve as an effective adsorbent for Methylene Blue due to strong electrostatic attractions.

Additionally, the combination of Activated Carbon Methylene Blue and Chitosan@Activated Carbon@Methylene Blue is shown. These combinations further highlight how Methylene Blue's positive electrostatic potential is effectively neutralized by the negative charge regions on the adsorbents, emphasizing the synergetic effects of combining

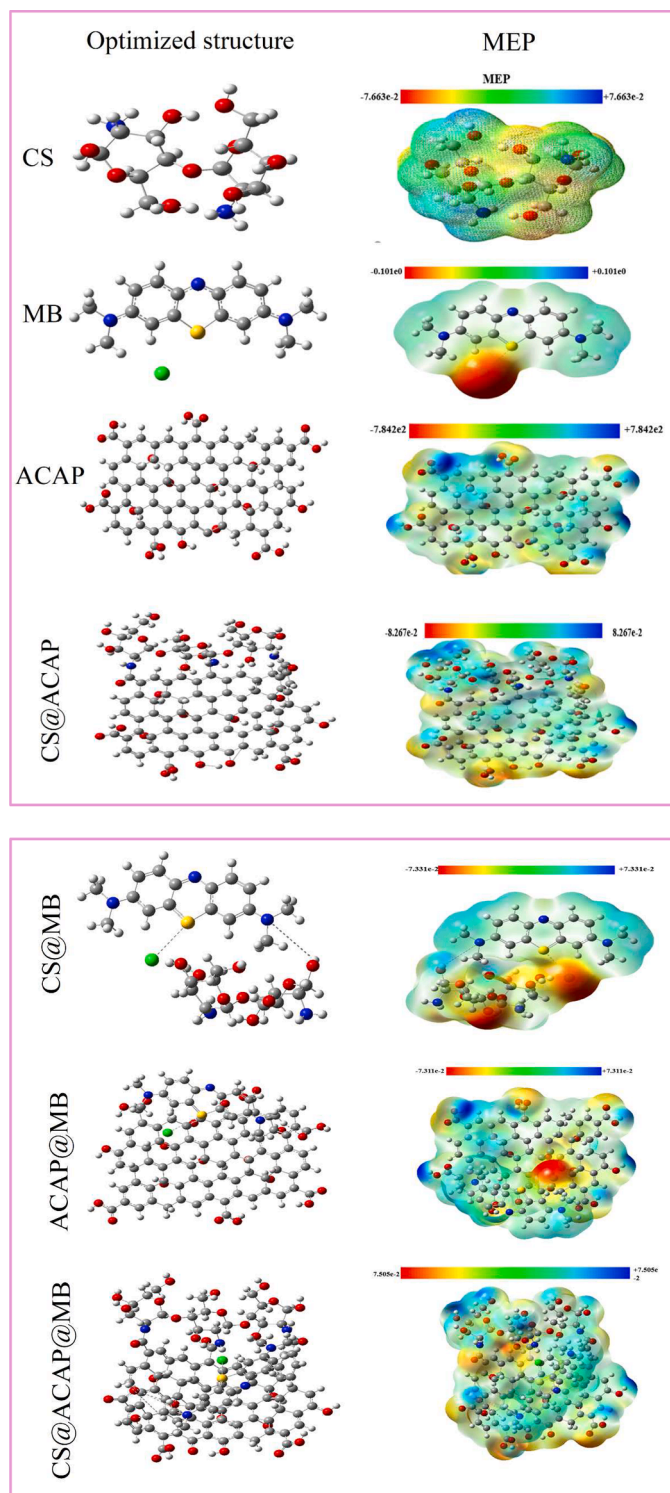


Fig. 21. Optimized structure and MEP Geometry of CS, MB, ACAP, CS@ACAP, CS@MB, ACAP @MB, CS@ACAP@MB.

Chitosan and Activated Carbon for better adsorption performance. The results shown in the Fig.21 demonstrate that the combination of Chitosan and Activated Carbon creates a composite material with improved adsorption efficiency for Methylene Blue.

#### 9.4. Mechanism of adsorption for MB

The adsorption mechanism of methylene blue (MB) onto the

chitosan@activated carbon (CS@ACAP) composite is governed by a combination of electrostatic interactions,  $\pi$ - $\pi$  stacking,  $\pi$ -n interactions, hydrogen bonding, and surface functional group interactions as shown at (Fig. 22), all of which play a crucial role in enhancing the adsorption efficiency and capacity of the composite material. Activated carbon, known for its extensive surface area and highly porous structure, provides an ideal platform for dye adsorption due to its  $\pi$ -conjugated system, which enables strong  $\pi$ - $\pi$  interactions with aromatic compounds of MB. The presence of hydroxyl (-OH) and oxygen-containing functional groups on activated carbon further enhances its adsorption capabilities by forming hydrogen bonds with MB molecules, thereby improving the stability of the adsorbed species. However, despite its high surface area and chemical reactivity, the adsorption capacity of activated carbon alone is limited ( $Q_m = 40.2$  mg/g), necessitating the incorporation of chitosan to improve its performance. Chitosan, introduces additional functional groups such as amine (-NH<sub>2</sub>) and hydroxyl (-OH), which significantly enhance electrostatic interactions between the positively charged MB molecules and the protonated amine groups (-NH<sub>3</sub><sup>+</sup>) of chitosan, leading to a higher adsorption capacity ( $Q_m = 81.0$  mg/g). The representation of the adsorption mechanism illustrates the crucial role played by these electrostatic interactions, as the positively charged MB molecules are strongly attracted to the negatively charged adsorption sites on the composite. Moreover, the  $\pi$ - $\pi$  interactions between MB and the graphitic structure of activated carbon facilitate strong binding, further stabilizing the adsorbed molecules. Additionally,  $\pi$ -n interactions, which involve the lone-pair electrons of oxygen in MB interacting with the  $\pi$ -electron system of the composite, provide another layer of adsorption stability, reinforcing the overall binding strength. Theoretical calculations further support these interactions, demonstrating that the highest occupied molecular orbital (HOMO) and lowest unoccupied molecular orbital (LUMO) energy levels of the composite facilitate efficient electron transfer, thereby promoting  $\pi$ - $\pi$  stacking interactions and increasing the overall adsorption efficiency. The integration of chitosan not only improves the electronic properties of the composite but also modifies the surface chemistry, creating additional active sites for MB adsorption. This is evident in the increase in the energy gap from 0.66 eV (for activated carbon alone) to 1.00 eV (for CS@ACAP), which indicates a more stable electronic structure conducive to effective dye adsorption. Furthermore, the presence of hydroxyl and amine functional groups enhances the hydrophilicity of the composite, improving its interaction with aqueous dye solutions and ensuring a higher affinity for MB molecules. The combination of these interactions results in a synergistic effect, wherein electrostatic attraction,  $\pi$ - $\pi$  stacking, and  $\pi$ -n interactions work in tandem to maximize MB adsorption efficiency. This synergistic behavior is further corroborated by experimental findings, which show that the CS@ACAP composite exhibits a significantly higher adsorption capacity compared to activated carbon alone, demonstrating the effectiveness of chitosan in enhancing adsorption performance. The adsorption mechanism is consistent with these findings, reinforcing the understanding that multiple intermolecular forces contribute to the superior adsorption capabilities of the composite. Moreover, the ability of chitosan to modify the electronic properties and surface functionalities of the composite further supports its role in optimizing adsorption efficiency, making it a highly promising material for wastewater treatment applications. The superior performance of CS@ACAP can also be attributed to its ability to facilitate multi-site adsorption, wherein MB molecules interact simultaneously with multiple functional groups on the composite surface, leading to enhanced stability and retention of dye molecules. This multi-site adsorption mechanism is crucial for maximizing the adsorption capacity and ensuring efficient dye removal from aqueous solutions. Furthermore, the enhanced adsorption capacity of the composite can be linked to the improved surface chemistry resulting from the integration of chitosan, which introduces additional binding sites and increases the probability of effective MB adsorption. The adsorption mechanism confirms that the combination of electrostatic interactions,  $\pi$ - $\pi$  stacking,

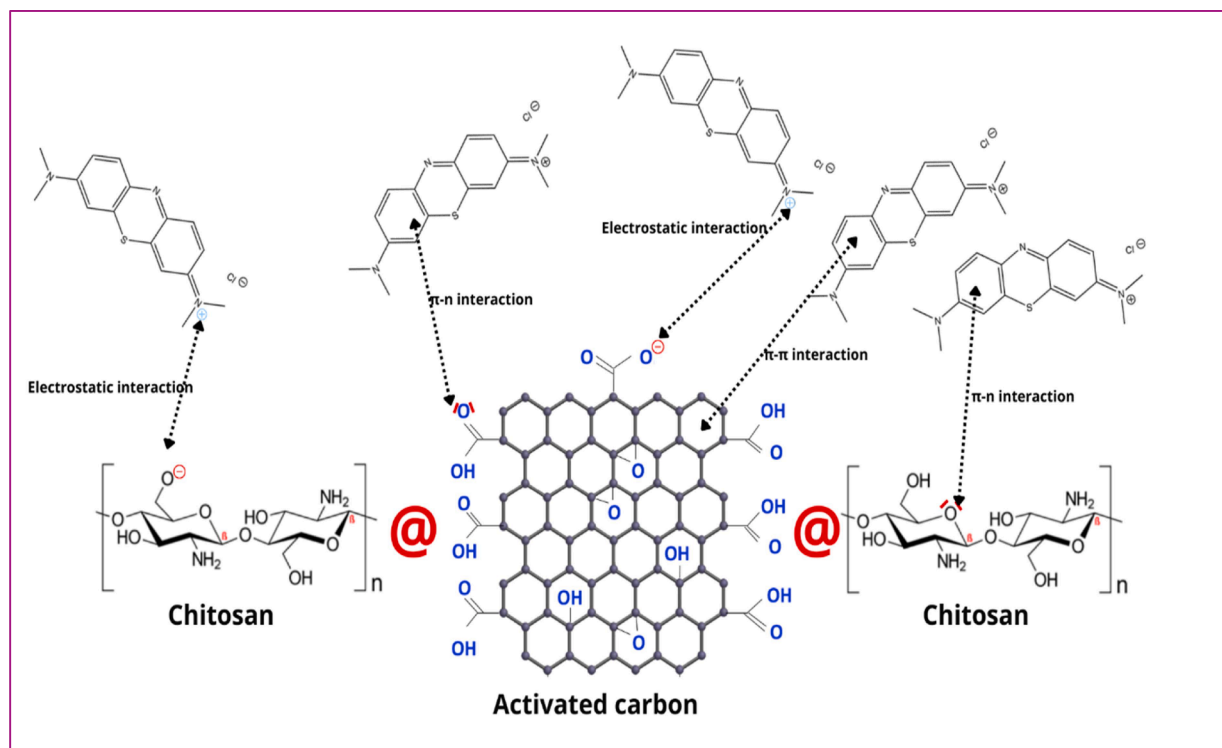


Fig. 22. Mechanism of adsorption of Methylene blue.

$\pi$ - $n$  interactions, and hydrogen bonding is responsible for the remarkable adsorption performance of the CS@ACAP composite. The integration of experimental and theoretical insights provides a comprehensive understanding of the adsorption mechanism, highlighting the key role played by functional group interactions and electronic properties in enhancing dye removal efficiency. By leveraging the unique properties of both activated carbon and chitosan, the CS@ACAP composite offers a highly efficient and sustainable solution for MB removal from contaminated water. The adsorption kinetics of MB onto CS@ACAP follow a pseudo-second-order model, suggesting that chemisorption plays a dominant role in the adsorption process, wherein MB molecules form strong chemical bonds with the functional groups on the composite surface. This chemisorption mechanism is further supported by thermodynamic studies, which indicate that the adsorption process is spontaneous and endothermic, meaning that higher temperatures favor increased dye uptake. The integration of chitosan into the activated carbon matrix not only improves the structural stability of the composite but also enhances its mechanical properties, making it a more robust and durable adsorbent for practical wastewater treatment applications. The adsorption mechanism depicted in the schematic aligns with these findings, confirming that the combination of  $\pi$ - $\pi$  stacking, electrostatic interactions,  $\pi$ - $n$  interactions, and hydrogen bonding is responsible for the exceptional adsorption performance of CS@ACAP. The ability of the composite to effectively remove MB from aqueous solutions demonstrates its potential as a highly efficient and sustainable adsorbent material for environmental remediation [150,151].

#### 9.5. Adsorbent's comparison of adsorption capacities of BM

The adsorption performance of the synthesized chitosan@activated carbon avocado pits (CS@ACAP) and activated carbon from avocado pits (ACAP) was evaluated in comparison with various activated carbon, natural, and chitosan-based adsorbents reported in the literature. Table 11 indicate that CS@ACAP exhibits the highest adsorption capacity (81.0 mg/g), significantly surpassing ACAP alone (40.2 mg/g). This substantial improvement highlights the synergistic effect of

Table 11

comparison of the methylene blue adsorption capacity of Chitosan and chitosan@activated carbon with other adsorbents.

Adsorbents	$q_{\max}$ (mg/g)	References
Activated Carbon-Based Adsorbents		
Activated carbon derived Almond shell	1.3	[152]
Activated carbon derived Indonesian Rice Husk	7.2	[153]
Activated carbon derived Hungarian Rice Husk	8.3	[153]
Activated carbon derived Coconut coir dust	14.3	[154]
Activated carbon nanofibers nonwoven flat sheet	24.7	[155]
Activated carbon avocado pits (ACAP)	40.2	This work
Natural Adsorbents		
Chamaerops humilis fibers	9.422	[156]
modified bagasse fly ash	15.5	[157]
Moroccan natural clay	32.5	[158]
golden mussel ( <i>Limnoperna fortunei</i> ) shell	26.4	[159]
Modified & Chitosan-Based Adsorbents		
Cross-linked chitosan/sepiolite	40.986	[160]
CuMn2O4/chitosan micro/nanocomposite	54.05	[161]
Chitosan-clay	70.00	[162]
Chitosan-modified cellulose	75.76	[163]
nano-TiO <sub>2</sub> /MWCNT/Chitosan	80.65	[164]
chitosan@activated carbon avocado pits (CS@ACAP)	81.0	This Work

chitosan modification, which enhances surface functionality by introducing additional active sites for adsorption. Compared to conventional activated carbon-based adsorbents, which show adsorption capacities ranging from 1.3 to 40.2 mg/g, and natural adsorbents with a maximum of 32.5 mg/g, the ACAP itself already demonstrates competitive adsorption performance, confirming the efficiency of avocado pit-derived activated carbon as a sustainable adsorbent. However, with chitosan modification, the adsorption capacity nearly doubles, reaching levels comparable to the most efficient chitosan-based composites reported, such as nano-TiO<sub>2</sub>/MWCNT/chitosan (80.65 mg/g).

## 10. Conclusion

In this study, we successfully prepared activated carbon from

avocado pits and optimized its methylene blue (MB) adsorption using a Box-Behnken design, considering key parameters such as sulfuric acid concentration, activation time, and temperature. The incorporation of chitosan into the activated carbon to form a CS@ACAP composite resulted in a significant enhancement of the adsorption capacity, with the composite achieving a maximum capacity ( $q_{max}$ ) of 81.0 mg/g, compared to 40.2 mg/g for the plain activated carbon. Characterization techniques including FTIR, SEM, XRD, BET, and EDX confirmed the structural modifications introduced by chitosan and the increased surface area, which contributed to the improved adsorption performance. Thermodynamic analysis revealed that the adsorption onto activated carbon was exothermic and spontaneous, while adsorption onto the composite was endothermic but became more favorable at higher temperatures. The isotherm studies highlighted the heterogeneity of the chitosan-modified surface, which provided additional adsorption sites, leading to superior performance. In conclusion, the chitosan@activated carbon composite offers a highly effective solution for the removal of MB from aqueous solutions, demonstrating improved adsorption capacity, especially at higher pH levels. The results of this study underscore the potential of natural, cost-effective adsorbents like avocado pits, particularly when combined with chitosan, in environmental applications. Furthermore, the insights gained from thermodynamic and DFT analyses pave the way for future research into the molecular interactions that govern adsorption processes, enhancing the development of even more efficient adsorbent materials.

#### CRedit authorship contribution statement

**Soukaina El Bourachdi:** Writing – original draft, Formal analysis, Data curation, Conceptualization. **Abdelhay El Amri:** Software, Methodology, Formal analysis, Data curation. **Ali Raza Ayub:** Software, Methodology, Formal analysis, Data curation. **Fatima Moussaoui:** Software, Methodology, Formal analysis, Data curation. **Yassine Rakcho:** Visualization, Resources, Methodology, Conceptualization. **Faïçal El Ouadrhiri:** Software, Methodology, Formal analysis, Data curation. **Abderrazzak Adachi:** Visualization, Resources, Methodology, Formal analysis. **Taoufiq Bouzid:** Methodology, Formal analysis, Data curation, Conceptualization. **José Alberto Herrera-Melián:** Visualization, Validation, Supervision, Methodology. **Amal Lakhimi:** Writing – review & editing, Visualization, Validation, Supervision.

#### Declaration of competing interest

The authors declare that they have no known competing financial interests or personal relationships that could have appeared to influence the work reported in this paper.

#### References

- [1] Pooresmaeil M, Zarehzadeh AJ, Namazi H. Design and preparation of ZnCo bimetallic metal-organic framework decorated on cellulose nanocrystals/magnetic graphene oxide for amoxicillin removal from aqueous solution. *J Taiwan Inst Chem Eng* 2025;170:105999. <https://doi.org/10.1016/j.jtice.2025.105999>.
- [2] Li R, Li X, Tian D, Liu X, Wu Z. Amino-functionalized MOF immobilized laccase for enhancing enzyme activity stability and degrading Congo red. *J Taiwan Inst Chem Eng* 2023;143:104647. <https://doi.org/10.1016/j.jtice.2022.104647>.
- [3] Ben Amor I, Hemmami H, Laouini SE, Zeghoud S, Benzina M, Achour S, et al. Use of Insect-Derived Chitosan for the Removal of Methylene Blue Dye from Wastewater: Process Optimization Using a Central Composite Design. *Materials (Basel)* 2023;16. <https://doi.org/10.3390/ma16145049>.
- [4] Khandelwal D, Rana I, Mishra V, Ranjan KR, Singh P. Unveiling the impact of dyes on aquatic ecosystems through zebrafish – A comprehensive review. *Environ Res* 2024;261:119684. <https://doi.org/10.1016/j.envres.2024.119684>.
- [5] Zabithi M, Motavalizadehkakhky A. PbS/ZIF-67 nanocomposite: novel material for photocatalytic degradation of basic yellow 28 and direct blue 199 dyes. *J Taiwan Inst Chem Eng* 2022;140:104572. <https://doi.org/10.1016/j.jtice.2022.104572>.
- [6] Ahadi N, Bakhtiari O. Preparation and optimization of nanocomposite membranes for ethanol dehydration via pervaporation by using response surface methodology. *J Taiwan Inst Chem Eng* 2024;165:105790. <https://doi.org/10.1016/j.jtice.2024.105790>.
- [7] Wang B, Wang T, Su H. A dye-methylene blue (MB)-degraded by hydrodynamic cavitation (HC) and combined with other oxidants. *J Environ Chem Eng* 2022;10:107877. <https://doi.org/10.1016/j.jece.2022.107877>.
- [8] Kumari S, Singh S, Lo SL, Sharma P, Agarwal S, Garg MC. Machine learning and modelling approach for removing methylene blue from aqueous solutions: Optimization, kinetics and thermodynamics studies. *J Taiwan Inst Chem Eng* 2024;166:105361. <https://doi.org/10.1016/j.jtice.2024.105361>.
- [9] Sarkar Phyllis A.K., Tortora G., Johnson I. Photodegradation. *Fairchild Books Dict Text* 2022. <https://doi.org/10.5040/9781501365072.12105>.
- [10] Blue M., Media A., Mokhtar E., Hassani S., Duarte H., Brás J., et al. On the Valorization of Olive Oil Pomace : a Sustainable Approach for On the Valorization of Olive Oil Pomace : a Sustainable Approach for Methylene Blue Removal from Aqueous Media 2024. <https://doi.org/10.3390/polym16213055>.
- [11] Muzammal S, Ahmad A, Sheraz M, Kim J, Ali S, Hanif MB, et al. Polymer-supported nanomaterials for photodegradation: Unraveling the methylene blue menace. *Energy Convers Manag X* 2024;22:100547. <https://doi.org/10.1016/j.ecmx.2024.100547>.
- [12] Majeed A, Ibrahim AH, SS Al-Rawi, Iqbal MA, Kashif M, Yousif M, et al. Green Organo-Photooxidative Method for the Degradation of Methylene Blue Dye. *ACS Omega* 2024;9:12069–83. <https://doi.org/10.1021/acsomega.3c09989>.
- [13] Zhou X, Guo X, Dong L, Zhou W, Li X. Dual functional Ag<sub>2</sub>MoO<sub>4</sub>/thickness-controlled g-C<sub>3</sub>N<sub>4</sub> composites for enhanced photocatalytic and adsorption activity. *J Taiwan Inst Chem Eng* 2025;167:105863. <https://doi.org/10.1016/j.jtice.2024.105863>.
- [14] Bih NL, Rwiza MJ, Ripanda AS, Mahamat AA, Machunda RL, Choi JW. Adsorption of phenol and methylene blue contaminants onto high-performance catalytic activated carbon from biomass residues. *Heliyon* 2025;11:e41150. <https://doi.org/10.1016/j.heliyon.2024.e41150>.
- [15] Al-Tohamy R, Ali SS, Li F, Okasha KM, Mahmoud YAG, Elsamahy T, et al. A critical review on the treatment of dye-containing wastewater: Ecotoxicological and health concerns of textile dyes and possible remediation approaches for environmental safety. *Ecotoxicol Environ Saf* 2022;231. <https://doi.org/10.1016/J.ECOENV.2021.113160>.
- [16] Li R, Zhang W, Yan S, Zhang D, Xu W. Degradation of Methylene blue in water using x-PMoV@MnCo<sub>2</sub>O<sub>4</sub>-NH<sub>2</sub>: Synergistic action with peroxymonosulfate and mechanistic insights. *Sep Purif Technol* 2025;354:129038. <https://doi.org/10.1016/j.seppur.2024.129038>.
- [17] Li S, Cui Y, Wen M, Ji G. Toxic Effects of Methylene Blue on the Growth, Reproduction and Physiology of *Daphnia magna*. *Toxics* 2023;11. <https://doi.org/10.3390/toxics11070594>.
- [18] Auerbach SS, Bristol DW, Peckham JC, Travlos GS, Hébert CD, Chhabra RS. Toxicity and carcinogenicity studies of methylene blue trihydrate in F344N rats and B6C3F1 mice. *Food Chem Toxicol* 2010;48:169–77. <https://doi.org/10.1016/j.fct.2009.09.034>.
- [19] Periyasamy AP. Recent Advances in the Remediation of Textile-Dye-Containing Wastewater: Prioritizing Human Health and Sustainable Wastewater Treatment. *Sustain* 2024;16. <https://doi.org/10.3390/su16020495>.
- [20] Amna R, Alzard RH, Faheem AF, Abdellah M. Journal of the Taiwan Institute of Chemical Engineers Computational and Kinetics analysis of lead ions removal from industrial wastewater through natural bone powder. *J Taiwan Inst Chem Eng* 2025;170:106016. <https://doi.org/10.1016/j.jtice.2025.106016>.
- [21] Rakcho Y, Mouiya M, Bouazizi A, Abouliatim Y, Sehaqui H, Mansouri S, et al. Treatment of seawater and wastewater using a novel low-cost ceramic membrane fabricated with red clay and tea waste. *Arab J Chem* 2023;16:105277. <https://doi.org/10.1016/j.arabjc.2023.105277>.
- [22] Gharibian S, Sajedi F, Hazrati H, Rostamizadeh M. Journal of the Taiwan Institute of Chemical Engineers Homogenous Electro-Fenton degradation of phenazopyridine in wastewater using a 3D Printed filter-press flowcell : Optimization via response surface methodology. *J Taiwan Inst Chem Eng* 2025;170:106026. <https://doi.org/10.1016/j.jtice.2025.106026>.
- [23] Alrozi R, Zubir NA, Bakar NFA, Ladewig BP, Motuzas J, Bakar NHHA, et al. Functional role of B-site substitution on the reactivity of CaMFeO<sub>3</sub> (M = Cu, Mo, Co) perovskite catalysts in heterogeneous Fenton-like degradation of organic pollutant. *J Taiwan Inst Chem Eng* 2023;143. <https://doi.org/10.1016/j.jtice.2023.104675>.
- [24] Choudhary M, Ray MB, Neogi S. Evaluation of the potential application of cactus (*Opuntia ficus-indica*) as a bio-coagulant for pre-treatment of oil sands process-affected water. *Sep Purif Technol* 2019;209:714–24. <https://doi.org/10.1016/j.seppur.2018.09.033>.
- [25] Kanwar RMA, Khan ZM, Farid HU. Fate of biofilm activity in cascade aerating trickling filter for wastewater treatment: Comparison of two types of indigenous support media. *Biochem Eng J* 2023;194:108875. <https://doi.org/10.1016/j.bej.2023.108875>.
- [26] Chahal M, Kumari S, Bhattacharya A, Garg MC. Evaluating sustainable agricultural waste biomass for methylene blue adsorption in wastewater treatment: a state-of-the-art review. *Bioresour Technol Reports* 2024;28:101983. <https://doi.org/10.1016/j.biteb.2024.101983>.
- [27] M Nanoparticle-assisted removal of EBT dye from textile waNarayanan, Salmen SH, Chinnathambi A, Suresh K, Ramesh, Barathi S, et al. steward: Towards sustainable green gram seedling cultivation. *J Taiwan Inst Chem Eng* 2023;166:105258. <https://doi.org/10.1016/j.jtice.2023.105258>.
- [28] Jaber L, Backer SN, Laoui T, Abumadi F, Koujan MMS, Khalil KA, et al. Recent trends in surface impregnation techniques on activated carbon for efficient

- pollutant removal from wastewater. *Desalin Water Treat* 2024;319:100562. <https://doi.org/10.1016/j.dwt.2024.100562>.
- [29] Shiferaw BT, Mengesha DN, Kim H. Enhanced adsorption capacity of phosphoric acid-modified montmorillonite clay and ground coffee waste-derived carbon-based functional composite beads for the effective removal of methylene blue. *Colloids Surfaces A Physicochem Eng Asp* 2024;695:134243. <https://doi.org/10.1016/j.colsurfa.2024.134243>.
- [30] Bo C, Jia Z, Liu B, Dai X, Ma G, Li Y. Copolymer-type magnetic graphene oxide with dual-function for adsorption of variety of dyes. *J Taiwan Inst Chem Eng* 2022;138:104499. <https://doi.org/10.1016/j.jtice.2022.104499>.
- [31] Khan AA, Naqvi SR, Ali I, Farooq W, Anjum MW, AlMohamadi H, et al. Algal biochar: a natural solution for the removal of Congo red dye from textile wastewater. *J Taiwan Inst Chem Eng* 2024. <https://doi.org/10.1016/j.jtice.2023.105312>.
- [32] Moussaoui F, El Ouadrhiri F, Saleh EAM, El Bourachdi S, Althomali RH, Kassem AF, et al. Enhancing hydrochar production and properties from biogenic waste: Merging response surface methodology and machine learning for organic pollutant remediation. *J Saudi Chem Soc* 2024;28:101920. <https://doi.org/10.1016/j.jscs.2024.101920>.
- [33] El S, Ali B., Ayub R., Rakcho Y., El A., Fatima A. Optimization of the degree of deacetylation of chitosan beads for efficient anionic dye adsorption : kinetics , thermodynamics , mechanistic insights via DFT analysis , and regeneration performance 2025.
- [34] El Bourachdi S, El Amri A, Ayub AR, Moussaoui F, Rakcho Y, El Ouadrhiri F, et al. Development of a novel low-cost adsorbent Chitosan@EDTA@Cellulose composite to effectively remove Methyl Orange dye from wastewater: Experimental and theoretical investigation. *Int J Biol Macromol* 2025;305. <https://doi.org/10.1016/j.ijbiomac.2025.141030>.
- [35] Tran ML, Van Tran TT, Juang RS, Nguyen CH. Graphene oxide crosslinked chitosan composites for enhanced adsorption of cationic dye from aqueous solutions. *J Taiwan Inst Chem Eng* 2023;142. <https://doi.org/10.1016/j.jtice.2023.104678>.
- [36] Vilén A, Laurell P, Vahala R. Comparative life cycle assessment of activated carbon production from various raw materials. *J Environ Manage* 2022;324. <https://doi.org/10.1016/j.jenvman.2022.116356>.
- [37] Salatein NM, Shaaban M, Fahim IS. Comparing low-cost activated carbon derived from coffee waste and bagasse to remove heavy metals and Methylene blue dye . Activated Carbon as an Adsorbent. *Results Chem* 2024;13:102020. <https://doi.org/10.1016/j.rechem.2025.102020>.
- [38] Choudhry Q, Fan M, Sun K, Li B, Zhang S, Kousar S, et al. Chemical activation of cotton fibers with varied reagents induces distinct morphology of activated carbon and adsorption capacity of methylene blue. *Int J Biol Macromol* 2025;295:139657. <https://doi.org/10.1016/j.ijbiomac.2025.139657>.
- [39] DALMAZ A, SÍVRİKAYA ÖZAK S. Methylene blue dye efficient removal using activated carbon developed from waste cigarette butts: Adsorption, thermodynamic and kinetics. *Fuel* 2024;372. <https://doi.org/10.1016/j.fuel.2024.132151>.
- [40] Dimbo D, Abewaa M, Adino E, Mengistu A, Takele T, Oro A, et al. Methylene blue adsorption from aqueous solution using activated carbon of spathodea campanulata. *Results Eng* 2024;21:101910. <https://doi.org/10.1016/j.rineng.2024.101910>.
- [41] Daniel LS, Rahman A, Hamushembe MN, Kapolo P, Uahengo V, Jonnalagadda SB. The production of activated carbon from *Acacia erioloba* seedpods via phosphoric acid activation method for the removal of methylene blue from water. *Bioresour Technol Reports* 2023;23:101568. <https://doi.org/10.1016/j.biteb.2023.101568>.
- [42] Njewa JB, VO Shikuku. Recent advances and issues in the application of activated carbon for water treatment in Africa: a systematic review (2007–2022). *Appl Surf Sci Adv* 2023;18:100501. <https://doi.org/10.1016/j.apsadv.2023.100501>.
- [43] Satyam S, Patra S. Innovations and challenges in adsorption-based wastewater remediation: a comprehensive review. *Heliyon* 2024;10:e29573. <https://doi.org/10.1016/j.heliyon.2024.e29573>.
- [44] Benamar K, El Bourachdi S, Lahkimi A, Ibsouda S, Fikri-benbrahim K. Remediation of the cationic dye Crystal Violet using *Olea oleaster* leaf biomass. *Int J Phytoremediation* 2025;0:1–16. <https://doi.org/10.1080/15226514.2025.2476092>.
- [45] Larasati A, Fowler GD, Graham NJD. Insights into chemical regeneration of activated carbon for water treatment. *J Environ Chem Eng* 2021;9:105555. <https://doi.org/10.1016/j.jece.2021.105555>.
- [46] Lewoyehu M. Comprehensive review on synthesis and application of activated carbon from agricultural residues for the remediation of venomous pollutants in wastewater. *J Anal Appl Pyrolysis* 2021;159:105279. <https://doi.org/10.1016/j.jaap.2021.105279>.
- [47] Azeez MO, Ganiyu SA. Review of biomass derived-activated carbon for production of clean fuels by adsorptive desulfurization: Insights into processes, modifications, properties, and performances. *Arab J Chem* 2023;16:105182. <https://doi.org/10.1016/j.arabjc.2023.105182>.
- [48] Ahmad T, Danish M. A review of avocado waste-derived adsorbents: Characterizations, adsorption characteristics, and surface mechanism. *Chemosphere* 2022;296:134036. <https://doi.org/10.1016/j.chemosphere.2022.134036>.
- [49] Kurniawan TA, Batool F, Mohyuddin A, Goh HH, Othman MHD, Aziz F, et al. Chitosan-coated coconut shell composite: a solution for treatment of Cr(III)-contaminated tannery wastewater. *J Taiwan Inst Chem Eng* 2024;166:105478. <https://doi.org/10.1016/j.jtice.2024.105478>.
- [50] Doyo AN, Kumar R, Barakat MA. Chitosan, and alginate based biopolymeric composites for adsorption of heavy metals from wastewaterRecent advances in cellulose. *J Taiwan Inst Chem Eng* 2023;151:105095. <https://doi.org/10.1016/j.jtice.2023.105095>.
- [51] Al-Hazmi GH, Albedair LA, Alatawi RAS, Alsuhaibani AM, Bukhari AAH, El-Bindary AA. Effective synthesis and characterization of citric acid cross-linking of modified ferrous metal-organic framework and chitosan nanocomposite sponge for Th(IV) elimination: Adsorption isotherms, kinetic analysis, and optimization by Box-Behnken design. *Int J Biol Macromol* 2024;281. <https://doi.org/10.1016/j.ijbiomac.2024.136194>.
- [52] Siddiq HA, Madkhali MMM, Ghubayra R, Alaghaz ANMA, El-Desouky MG, El-Bindary MA, et al. Efficient removal of tetracycline by VCo-layered double hydroxide encapsulated with chitosan: Optimization via Box-Behnken design, and thermodynamics. *Int J Biol Macromol* 2025;296. <https://doi.org/10.1016/j.ijbiomac.2025.139565>.
- [53] Al-Hazmi GAAM, Elsayed NH, Alnawmisi JS, Alomari KB, Alessa AH, Alshareef SA, et al. Elimination of Ni(II) from wastewater using metal-organic frameworks and activated algae encapsulated in chitosan/carboxymethyl cellulose hydrogel beads: Adsorption isotherm, kinetic, and optimizing via Box-Behnken design optimization. *Int J Biol Macromol* 2025;299:140019. <https://doi.org/10.1016/j.ijbiomac.2025.140019>.
- [54] Hevira L, Ighalo JO, Sondari D. Chitosan-based polysaccharides for effective synthetic dye adsorption. *J Mol Liq* 2024;393:123604. <https://doi.org/10.1016/j.molliq.2023.123604>.
- [55] Shen J, Gu Y, Yang Y, He J, Zhao C, Sun Y, et al. Polydopamine modified cerium-based MOFs/chitosan aerogel beads for the efficient phosphate removal. *Chemosphere* 2023;345:140421. <https://doi.org/10.1016/j.chemosphere.2023.140421>.
- [56] Tichapondwa SM, Newman JP, Kubheka O. Effect of TiO2 phase on the photocatalytic degradation of methylene blue dye. *Phys Chem Earth* 2020;118–9. <https://doi.org/10.1016/j.pce.2020.102900>.
- [57] Raja KS, Taip FS, Azmi MMZ, Shishir MRI. Effect of pre-treatment and different drying methods on the physicochemical properties of *Carica papaya* L. leaf powder. *J Saudi Soc Agric Sci* 2019;18:150–6. <https://doi.org/10.1016/j.jssas.2017.04.001>.
- [58] Pak SH, Jeon MJ, Jeon YW. Study of sulfuric acid treatment of activated carbon used to enhance mixed VOC removal. *Int Biodeterior Biodegrad* 2016;113:195–200. <https://doi.org/10.1016/j.ibiod.2016.04.019>.
- [59] Badawi AK, Hassan R, Alghamdi AM, Ismail B, Osman RM, Salama RS. Advancing cobalt ferrite-supported activated carbon from orange peels for real pulp and paper mill wastewater treatment. *Desalin Water Treat* 2024;318:100331. <https://doi.org/10.1016/j.dwt.2024.100331>.
- [60] Tsarpali M, Kuhn JN, Philippidis GP. Activated carbon production from algal biochar: Chemical activation and feasibility analysis. *Fuel Commun* 2024;19:100115. <https://doi.org/10.1016/j.fucom.2024.100115>.
- [61] Kozma M, Acharya B, Bissessur R. Chitin, Chitosan, and Nanochitin: Extraction, Synthesis, and Applications 2022:1–28.
- [62] Al-Hazmi GAAM, Alayyafi AAA, El-Desouky MG, El-Bindary AA. Chitosan-nano CuO composite for removal of mercury (II): box-Behnken design optimization and adsorption mechanism. *Int J Biol Macromol* 2024;261. <https://doi.org/10.1016/j.ijbiomac.2024.129769>.
- [63] Blanco L, Martínez-Rico O, Domínguez Á, González B. Removal of Acid Blue 80 from aqueous solutions using chitosan-based beads modified with choline chloride:urea Deep Eutectic Solvent and FeO. *Water Resour Ind* 2023;29. <https://doi.org/10.1016/j.wri.2022.100195>.
- [64] de Freitas FP, Carvalho AMML, Carneiro A de CO, de Magalhães MA, Xisto MF, Canal WD. Adsorption of neutral red dye by chitosan and activated carbon composite films. *Heliyon* 2021;7. <https://doi.org/10.1016/j.heliyon.2021.e07629>.
- [65] Chen X, Liu H, Yang Y, Li P, Wang X, Zhang K, et al. Chitosan-based emulsion gel beads developed on the multiple-unit floating delivery system for gastric sustained release of proanthocyanidins. *Food Hydrocolloid* 2025;159:110704. <https://doi.org/10.1016/j.foodhyd.2024.110704>.
- [66] Tuntun SM, Sahadat Hossain M, Akter S, Bahadur NM, Alam MS, Ahmed S. Synthesis of nano crystallite cellulose and chitosan from waste natural source for the adsorption of cationic and anionic dyes in aqueous medium. *Hybrid Adv* 2024;6:100270. <https://doi.org/10.1016/j.hybadv.2024.100270>.
- [67] Mohammed IA, Malek NNA, Jawad AH, Mastuli MS, AlOthman ZA. Box-Behnken Design for Optimizing Synthesis and Adsorption Conditions of Covalently Crosslinked Chitosan/Coal Fly Ash Composite for Reactive Red 120 Dye Removal. *J Polym Environ* 2022;30:3447–62. <https://doi.org/10.1007/s10924-022-02443-z>.
- [68] Atanda SA, Shaibu RO, Agunbiade FO. Eco-friendly synthesis and antibacterial potential of chitosan crosslinked-EDTA silver nanocomposite (CCESN). *J Mater Sci Mater Eng* 2024;19. <https://doi.org/10.1186/s40712-024-00164-w>.
- [69] Abomuti MA, Danish EY, Firoz A, Hasan N, Malik MA. Green synthesis of zinc oxide nanoparticles using salvia officinalis leaf extract and their photocatalytic and antifungal activities. *Biology (Basel)* 2021;10. <https://doi.org/10.3390/BIOLOGY10111075>.
- [70] Asmae B., Ahmed B., Benaouda B., Saleh Y., Saleh G., Benderdouche N., et al. Journal of the Taiwan Institute of Chemical Engineers Selected pharmaceutical pollutant recovery from wastewater by an agro-byproduct *Laurus nobilis* -based adsorbent : Theoretical and experimental studies 2025;170. <https://doi.org/10.1016/j.jtice.2025.106011>.
- [71] El Bourachdi S, El Ouadrhiri F, Moussaoui F, Abdu E, Saleh M, El Amri A, et al. Enhancing Graphene Oxide Production and Its Efficacy in Adsorbing Crystal Violet : An In-Depth Study of Thermodynamics, Kinetics , and DFT Analysis 2024; 2024. <https://doi.org/10.1155/2024/8222314>.

- [72] Khezami L, Elamin N, Modwi A, Taha KK, Amer MS, Bououdina M. Mesoporous Sn@TiO<sub>2</sub> nanostructures as excellent adsorbent for Ba ions in aqueous solution. *Ceram Int* 2022;48:5805–13. <https://doi.org/10.1016/j.ceramint.2021.11.128>.
- [73] Lechheb M, Essifi K, El Bourachdi S, Ouallah H, El Ouali M, Essafraoui B, et al. Optimisation of mechanical and thermal properties of clay bricks from Rissani-Morocco using Box-Behnken experimental design. *Eur J Environ Civ Eng* 2025;0: 1–21. <https://doi.org/10.1080/19648189.2025.2458282>.
- [74] El Ouadrhiri F, Adachi A, Mehdaoui I, Moussaoui F, Fouad K, Lhassani A, et al. Optimization of hydrochar production from almond shells using response surface methodology, artificial neural network, support vector machine and XGBoost. *Desalin Water Treat* 2024;317:100154. <https://doi.org/10.1016/j.dwt.2024.100154>.
- [75] Hamidallah K, Zourif A, Kouniba S, Safi Z, Bensalah J, Benbiyi A, et al. Insights of the adsorption mechanism of Bemacid Red using coagulation-flocculation sludge: Optimisation using BBD-RSM and DFT calculations. *J Mol Liq* 2024;409:125540. <https://doi.org/10.1016/j.molliq.2024.125540>.
- [76] Bhatuwalwa R, Bagban M, Mansuri A, Modi H. Successive approach of medium optimization using one-factor-at-a-time and response surface methodology for improved β-mannanase production from *Streptomyces* sp. *Bioresour Technol Reports* 2022;18:101087. <https://doi.org/10.1016/j.biteb.2022.101087>.
- [77] Wang L, Guo Y, Zou B, Rong C, Ma X, Qu Y, et al. High surface area porous carbons prepared from hydrochars by phosphoric acid activation. *Bioresour Technol* 2011;102:1947–50. <https://doi.org/10.1016/j.biortech.2010.08.100>.
- [78] Bergna D, Varila T, Romar H, Lassi U. Comparison of the Properties of Activated Carbons Produced in One-Stage and Two-Stage Processes. *C (Basel)* 2018;4:41. <https://doi.org/10.3390/c4030041>.
- [79] BENATIA A, GOUITAA N, dine LAMCHARFI T, ABDI F, HADDAD M. Effect of calcination temperature and duration on structural and dielectric properties of CaFeO<sub>3-δ</sub>. *Arab J Chem* 2024;17:105407. <https://doi.org/10.1016/j.arabjch.2023.105407>.
- [80] Mchich Z, Aziz K, Kjidaa B, Saffaj N, Saffaj T, Mamouni R. Eco-friendly engineering of micro composite-based hydroxyapatite bio crystal and polyaniline for high removal of OG dye from wastewater: Adsorption mechanism and RSM@BBD optimization. *Environ Res* 2024;257:119289. <https://doi.org/10.1016/j.envres.2024.119289>.
- [81] Wardighi Z, EL Amri A, Kadiri L, Jebli A, Bouhassane FZ, Rifi EH, et al. Ecological study of elimination of the organic pollutant (violet crystal) using natural fibers of *Rubia tinctorum*: Optimization of adsorption processes by BBD-RSM modeling and DFT approaches. *Inorg Chem Commun* 2023;155:111014. <https://doi.org/10.1016/j.inoche.2023.111014>.
- [82] Aliyu A. Synthesis, electron microscopy properties and adsorption studies of Zinc (II) ions (Zn<sup>2+</sup>) onto as-prepared Carbon Nanotubes (CNTs) using Box-Behnken Design (BBD). *Sci African* 2019;3:e00069. <https://doi.org/10.1016/j.sciaf.2019.e00069>.
- [83] Hamidallah K, El Rharib M, Elseny M, De Gisi S, Anouar A. Biogenic synthesis of MgO nanoparticles using *Arbutus Unedo* leaf extract for removal of Bemacid Red from wastewater: Optimizing using BBD-RSM and ANN approach. *J Water Process Eng* 2024;66:106008. <https://doi.org/10.1016/j.jwpe.2024.106008>.
- [84] El Ouadrhiri F, Elyemmi M, Lahkimi A, Lhassani A, Chaouch M, Taleb M. Mesoporous Carbon from Optimized Date Stone Hydrochar by Catalytic Hydrothermal Carbonization Using Response Surface Methodology: Application to Dyes Adsorption. *Int J Chem Eng* 2021;2021. <https://doi.org/10.1155/2021/5555406>.
- [85] Adachi A, Soujoud R, El Ouadrhiri F, Tarik M, Hmamou A, Eloutassi N, et al. Cactus and Holm Oak Acorn for Efficient Textile Wastewater Treatment by Coagulation-Flocculation Process Optimization Using Box-Behnken Design. *J Ecol Eng* 2023;24:315–28. <https://doi.org/10.12911/22998993/162784>.
- [86] Pravina R, Uthayakumar H, Sivasamy A. Hybrid approach based on response surface methodology and artificial neural networks coupled with genetic algorithm (RSM-GA-ANN) for the Prediction and optimization for the Photodegradation of dye using nano ZnO anchored glass fiber under solar light irradiation. *J Taiwan Inst Chem Eng* 2023;153. <https://doi.org/10.1016/j.jtice.2023.105248>.
- [87] El S, Moussaoui F, El A, El F, Adachi A, Bendaoud A, et al. DFT theoretical analysis, experimental approach, and RSM process to understand the congo red adsorption mechanism on Chitosan @ Graphene oxide beads. *J Mol Struct* 2025; 1321:140090. <https://doi.org/10.1016/j.molstruc.2024.140090>.
- [88] Jebli A, El Amri A, Hsissou R, Lebikiri A, Zarrik B, Bouhassane FZ, et al. Synthesis of a chitosan@hydroxyapatite composite hybrid using a new approach for high-performance removal of crystal violet dye in aqueous solution, equilibrium isotherms and process optimization. *J Taiwan Inst Chem Eng* 2023;149:105006. <https://doi.org/10.1016/j.jtice.2023.105006>.
- [89] Adachi A, El Ouadrhiri F, Abdu Musad Saleh E, Moussaoui F, Althomali RH, El Bourachdi S, et al. Enhancing hydrogen peroxide activation in heterogeneous Fenton reaction by codoping hydrochar with iron and Copper. *Arab J Chem* 2024; 17:105862. <https://doi.org/10.1016/j.arabjch.2024.105862>.
- [90] Al-Hazmi GAAM, Alayyafi AAA, El-Desouky MG, El-Bindary AA. Guava seed activated carbon loaded calcium alginate aerogel for the adsorption of diclofenac sodium: Characterization, isotherm, kinetics, and optimization via Box-Behnken design. *Int J Biol Macromol* 2024;262:129995. <https://doi.org/10.1016/j.ijbiomac.2024.129995>.
- [91] Ghubayra R, Mousa I, Madkhali MMM, Alaghash ANMA, Elsayed NH, El-Bindary AA. Synthesis and characterization of a novel TiO<sub>2</sub>@chitosan/alginate nanocomposite sponge for highly efficient removal of As(V) ions from aqueous solutions: Adsorption isotherm, kinetics, experiment and adsorption mechanism optimization using Box-Behnken desi. *Int J Biol Macromol* 2024;275:133513. <https://doi.org/10.1016/j.ijbiomac.2024.133513>.
- [92] Alshammari NAH, Alnawmasi JS, Alotaibi AM, Alshammari OAO, Abomuti MA, Elsayed NH, et al. Efficient adsorption of fluorescein dye from aqueous solutions by Al/Th-MOF bimetal-organic frameworks: Adsorption isotherm, kinetics, DFT computation, and optimization via Box-Behnken design. *Process Saf Environ Prot* 2024;190:353–71. <https://doi.org/10.1016/j.psep.2024.08.037>.
- [93] Yan C, Peng D, Chen X, Zhang Y, Liu H, Xu H. Journal of the Taiwan Institute of Chemical Engineers Recovery of phosphate and removal of Cr (VI) from water by calcium-modified panda manure biochar : Synergistic effect of adsorption and reduction. *J Taiwan Inst Chem Eng* 2025;170:106015. <https://doi.org/10.1016/j.jtice.2025.106015>.
- [94] Revellame ED, Fortela DL, Sharp W, Hernandez R, Zappi ME. Adsorption kinetic modeling using pseudo-first order and pseudo-second order rate laws: a review. *Clean Eng Technol* 2020;1:100032. <https://doi.org/10.1016/j.clet.2020.100032>.
- [95] Wang N, Zhu F, Liu M, Zhou J, Zhang Y, Ge Y, et al. Synthesis, adsorption and theoretical calculation study of the two polar-modified hyper-cross-linked resins for efficient removal of o-toluidine from aqueous solution. *J Taiwan Inst Chem Eng* 2024;161:105523. <https://doi.org/10.1016/j.jtice.2024.105523>.
- [96] Koopal L, Tan W, Avena M. Mixed ad/desorption kinetics unraveled with the equilibrium adsorption isotherm. *Colloids Surfaces A Physicochem Eng Asp* 2019; 577:709–22. <https://doi.org/10.1016/j.colsurfa.2019.06.033>.
- [97] Adachi A, El Ouadrhiri F, El Manssouri I, Moussaoui F, El Bourachdi S, Lahkimi A. Removal of Dyes by Adsorption Process Using Date Pits as Material Environmentally Friendly. *Ecol Eng Environ Technol* 2023;24:181–93. <https://doi.org/10.12912/27197050/171494>.
- [98] Qurat-Ul-Ain Khatoun J, Shah MR, Malik MI, Khan IAT, Khurshid S, et al. Convenient pH-responsive removal of Acid Black 1 by green l-histidine/iron oxide magnetic nanoadsorbent from water: Performance and mechanistic studies. *RSC Adv* 2019;9:2978–96. <https://doi.org/10.1039/C8RA09279F>.
- [99] Pegade U, Jethave G, Attarde S, Kolate S, Inamuddin Althali T, et al. Statistical Physics Model of EBT Adsorption on Pb(II) doped Zinc Oxide Nanoparticles: Kinetics, Isotherm and Reuse Study. *Int J Environ Anal Chem* 2023;103:3309–23. <https://doi.org/10.1080/03067319.2021.1907358>.
- [100] Shaban M, Abukhadra MR, Khan AAP, Jibali BM. Removal of Congo red, methylene blue and Cr(VI) ions from water using natural serpentine. *J Taiwan Inst Chem Eng* 2018;82:102–16. <https://doi.org/10.1016/j.jtice.2017.10.023>.
- [101] Gómez-Serrano V, Adame-Pereira M, Alexandre-Franco M, Fernández-González C. Adsorption of bisphenol A by activated carbon developed from PET waste by KOH activation. *Environ Sci Pollut Res* 2021;28:24342–54. <https://doi.org/10.1007/S11356-020-08428-6>.
- [102] Hassani EMS, Mehdaoui I, Azzouni D, Mahmoud R, Taleb A, Wondmie GF, et al. Elaboration of an innovative plant biomaterial for its valorization in the treatment of wastewater. *Bioresour Bioprocess* 2024;11. <https://doi.org/10.1186/s40643-024-00774-4>.
- [103] Prajapati AK, Mondal MK. Novel green strategy for CuO–ZnO–C nanocomposites fabrication using marigold (*Tagetes* spp.) flower petals extract with and without CTAB treatment for adsorption of Cr(VI) and Congo red dye. *J Environ Manage* 2021;290. <https://doi.org/10.1016/j.jenvman.2021.112615>.
- [104] Koujalagi PS, Divekar SV, Kulkarni RM, Nagarekar RK. Kinetics, thermodynamic, and adsorption studies on removal of chromium(VI) using Tulsion A-27(MP) resin. *Desalin Water Treat* 2013;51:3273–83. <https://doi.org/10.1080/19443994.2012.749049>.
- [105] Kaya T, Selçuki C, Acar N. A DFT and TDDFT investigation of interactions between 1-hydroxypyrene and aromatic amino acids. *Comput Theor Chem* 2015; 1073:9–19. <https://doi.org/10.1016/j.comptc.2015.09.009>.
- [106] Bouzzine SM, Bouzakraoui S, Bouachrine M, Hamidi M. Density functional theory (B3LYP/6-31G\*) study of oligothiophenes in their aromatic and polaronic states. *J Mol Struct THEOCHEM* 2005;726:271–6. <https://doi.org/10.1016/j.theochem.2005.04.023>.
- [107] Pandey AK, Dwivedi A, Mishra AK, Tiwari SN, Vuai SAH, Singh V. Quantum chemical study of effect on adsorption properties of antituberculosis drug N-Cyclopentylidene pyridine-4-carbohydrazide interaction with CNT(C56H16). *J Indian Chem Soc* 2023;100:100851. <https://doi.org/10.1016/j.jics.2022.100851>.
- [108] Chatterjee S, Afzal M, Mandal PC, Modak R, Guin M, Konar S. Exploration of supramolecular interactions, Hirshfeld surface, FMO, molecular electrostatic potential (MEP) analyses of pyrazole based Zn(II) complex. *J Indian Chem Soc* 2024;101:101275. <https://doi.org/10.1016/J.JICS.2024.101275>.
- [109] Gigli V, Capecchi E, Tortolini C, Isidori A, Antiochia R, Saladino R. Tuning the Effect of Chitosan on the Electrochemical Responsiveness of Lignin Nanoparticles. *ACS Biomater Sci Eng* 2023;9:3597–605. <https://doi.org/10.1021/acsbiomaterials.2c01494>.
- [110] Mardani HR, Ravari F, Kalaki A, Hokmabadi L. New Schiff-Base's Modified Chitosan: Synthesis, Characterization, Computational, Thermal Study and Comparison on Adsorption of Copper(II) and Nickel(II) Metal Ions in Aqueous. *J Polym Environ* 2020;28:2523–38. <https://doi.org/10.1007/s10924-020-01788-7>.
- [111] Kumar G, Kumar H, Sharma R, Kumari R, Dhayal A, Yadav A, et al. Synergistic performance of epoxy modified cellulose/polyaniline/ternary metal oxide nanocomposites. *Next Mater* 2024;2:100141. <https://doi.org/10.1016/j.nxmater.2024.100141>.
- [112] Celina MC, Linde E, Martinez E. Carbonyl Identification and Quantification Uncertainties for Oxidative Polymer Degradation. *Polym Degrad Stab* 2021;188: 109550. <https://doi.org/10.1016/j.polymdegradstab.2021.109550>.

- [113] Md Salim R, Asik J, Sarjadi MS. Chemical functional groups of extractives, cellulose and lignin extracted from native *Leucaena leucocephala* bark. *Wood Sci Technol* 2021;55:295–313. <https://doi.org/10.1007/s00226-020-01258-2>.
- [114] Raspolli Galletti AM, D'Alessio A, Licursi D, Antonetti C, Valentini G, Galia A, et al. Midinfrared FT-IR as a tool for monitoring herbaceous biomass composition and its conversion to furfural. *J Spectrosc* 2015;2015. <https://doi.org/10.1155/2015/719042>.
- [115] Islam MS, Ang BC, Gharehkhani S, Affi ABM. Adsorption capability of activated carbon synthesized from coconut shell. *Carbon Lett* 2016;20:1–9. <https://doi.org/10.5714/CL.2016.20.001>.
- [116] Zhao C, Ge L, Mai L, Chen S, Li Q, Yao L, et al. Preparation and performance of coal-based activated carbon based on an orthogonal experimental study. *Energy* 2023;274:127353. <https://doi.org/10.1016/j.energy.2023.127353>.
- [117] AlSalem HS, Alatawi RAS, Bukhari AAH, Alnawmisi JS, Zghab I, El-Desouky MG, et al. Adsorption and removal of Pb (II) via layer double hydroxide encapsulated with chitosan; synthesis, characterization adsorption isotherms, kinetics, thermodynamics, & optimization via Box-Behnken design. *Int J Biol Macromol* 2024;283. <https://doi.org/10.1016/j.ijbiomac.2024.137517>.
- [118] da Silva, Alves DC, Healy B, Pinto LA dA, Cadaval TRS, Breslin CB. Recent developments in Chitosan-based adsorbents for the removal of pollutants from aqueous environments. *Molecules* 2021;26. <https://doi.org/10.3390/molecules26030594>.
- [119] Hu H, Song H, Cheng Z, Wang Y, Zhang Q, Hu H, et al. Preparation of Composites Derived from Modified Loess/Chitosan and Its Adsorption Performance for Methyl Orange. *Molecules* 2024;29. <https://doi.org/10.3390/molecules29215052>.
- [120] Kumar S, Koh J. Physicochemical, optical and biological activity of chitosan-chromone derivative for biomedical applications. *Int J Mol Sci* 2012;13:6102–16. <https://doi.org/10.3390/ijms13056102>.
- [121] Saka CBET, TG-DTG FTIR, SEM, iodine number analysis and preparation of activated carbon from acorn shell by chemical activation with ZnCl<sub>2</sub>. *J Anal Appl Pyrolysis* 2012;95:21–4. <https://doi.org/10.1016/j.jaap.2011.12.020>.
- [122] Sumi K, Supraja KS, Aashika RC, Arivanandhan M. Biomass-derived activated carbon/cerium oxide nanocomposite as adsorptive photocatalyst for effective removal of carcinogenic dye. *Mater Res Bull* 2025;183:113212. <https://doi.org/10.1016/j.materresbull.2024.113212>.
- [123] Lester E, Hilal N, Henderson J. Porosity in ancient glass from Syria (c. 800 AD) using gas adsorption and atomic force microscopy. *Surf Interface Anal* 2004;36:1323–9. <https://doi.org/10.1002/sia.1911>.
- [124] Yan J, Xu J, Ai S, Zhang K, Yang F, Huang Y. Degradation of chitosan with self-resonating cavitation. *Arab J Chem* 2020;13:5776–87. <https://doi.org/10.1016/j.arabjc.2020.04.015>.
- [125] Ardekani PS, Karimi H, Ghaedi M, Asfaram A, Purkait MK. Ultrasonic assisted removal of methylene blue on ultrasonically synthesized zinc hydroxide nanoparticles on activated carbon prepared from wood of cherry tree: Experimental design methodology and artificial neural network. *J Mol Liq* 2017;229:114–24. <https://doi.org/10.1016/j.molliq.2016.12.028>.
- [126] Aziz K, Mamouni R, Azrrar A, Kjidaa B, Saffaj N, Aziz F. Enhanced biosorption of bisphenol A from wastewater using hydroxyapatite elaborated from fish scales and camel bone meal: a RSM/BBDO optimization approach. *Ceram Int* 2022;48:15811–23. <https://doi.org/10.1016/j.ceramint.2022.02.119>.
- [127] El Ouadrhiri F, Abdu Musad Saleh E, Husain K, Adachi A, Hmamou A, Hassan I, et al. Acid assisted-hydrothermal carbonization of solid waste from essential oils industry: Optimization using I-optimal experimental design and removal dye application. *Arab J Chem* 2023;16. <https://doi.org/10.1016/J.ARABJC.2023.104872>.
- [128] Adebayo MA, Adebomi JI, Abe TO, Aro FI. Removal of aqueous Congo red and malachite green using ackee apple seed–bentonite composite. *Colloids Interface Sci Commun* 2020;38. <https://doi.org/10.1016/j.colcom.2020.100311>.
- [129] El Khomri M, El Messaoudi N, Dbik A, Bentahar S, Lacherai A. Efficient adsorbent derived from *Argania spinosa* for the adsorption of cationic dye: Kinetics, mechanism, isotherm and thermodynamic study. *Surf Interfaces* 2020;20:100601. <https://doi.org/10.1016/j.surfin.2020.100601>.
- [130] Abbas M, Trari M. Mass transfer process in the removal of Congo Red (CR) onto Natural Clay (NC): Kinetic, isotherm modeling, and thermodynamic study. *J Water Clim Chang* 2023;14:2755–72. <https://doi.org/10.2166/WCC.2023.103>.
- [131] Ullah F, Ul Haq Khan Z, Sabahat S, Aftab M, Sun J, Samad Shah N, et al. Synergistic degradation of toxic azo dyes using Mn-CuO@Biochar: An efficient adsorptive and photocatalytic approach for wastewater treatment. *Chem Eng Sci* 2025;302:120844. <https://doi.org/10.1016/J.CES.2024.120844>.
- [132] Mall ID, Srivastava VC, Agarwal NK, Mishra IM. Removal of congo red from aqueous solution by bagasse fly ash and activated carbon: Kinetic study and equilibrium isotherm analyses. *Chemosphere* 2005;61:492–501. <https://doi.org/10.1016/j.chemosphere.2005.03.065>.
- [133] Mahmood G, Dabagh A, El-Habacha M, Lagdali S, Assouani A, Soulaïman I, et al. Preparation and characterization of biomaterial for phosphate ion removal: Kinetics, isotherms and thermodynamics studies. *Desalin Water Treat* 2024;317:100062. <https://doi.org/10.1016/j.dwt.2024.100062>.
- [134] Banerjee S, Chattopadhyaya MC. Adsorption characteristics for the removal of a toxic dye, tartrazine from aqueous solutions by a low cost agricultural by-product. *Arab J Chem* 2017;10:S1629–38. <https://doi.org/10.1016/j.arabjc.2013.06.005>.
- [135] Naushad M, Vasudevan S, Sharma G, Kumar A, Alothman ZA. Adsorption kinetics, isotherms, and thermodynamic studies for Hg<sup>2+</sup> adsorption from aqueous medium using alizarin red-S-loaded amberlite IRA-400 resin. *Desalin Water Treat* 2016;57:18551–9. <https://doi.org/10.1080/19443994.2015.1090914>.
- [136] Ahmad R, Ansari K. Fabrication of alginate@silver nanoparticles (Alg@AgNPs) bionanocomposite for the sequestration of crystal violet dye from aqueous solution. *Int J Biol Macromol* 2022;218:157–67. <https://doi.org/10.1016/j.ijbiomac.2022.07.092>.
- [137] Guo X, Wu Z, Wang Z, Lin F, Li P, Liu J. Preparation of Chitosan-Modified Bentonite and Its Adsorption Performance on Tetracycline. *ACS Omega* 2023;8:19455–63. <https://doi.org/10.1021/acsomega.3c00745>.
- [138] Al-Ghamdi AA, Galhoum AA, Alshahrie A, Al-Turki YA, Al-Amri AM, Wageh S. Superparamagnetic Multifunctionalized Chitosan Nanohybrids Stability, and Mechanism Insights. *Polymers (Basel)* 2023;15:1157.
- [139] Samia N, Usman M, Osman AI, Khan KI, Saeed F, Zeng Y, et al. Enhanced visible-light photocatalytic degradation of organic pollutants using fibrous silica titania and Ti3AlC<sub>2</sub> catalysts for sustainable wastewater treatment. *New J Chem* 2024:17500–15. <https://doi.org/10.1039/d4nj03277b>.
- [140] Duan Y, Stinespring CD, Chorpeng B. Electronic Structures, Bonding Configurations, and Band-Gap-Opening Properties of Graphene Binding with Low-Concentration Fluorine. *ChemistryOpen* 2015;4:642–50. <https://doi.org/10.1002/open.201500074>.
- [141] Tran VQ, Nguyen TN, Nguyen TH, Tran VS. Adsorption of Arsenate from Water by Iron-Chitosan Modified Fly Ash. *IOP Conf Ser Earth Environ Sci* 2024:1383. <https://doi.org/10.1088/1755-1315/1383/1/012010>.
- [142] Xiao M, Yue HD, Feng XJ, Wang YT, He MY, Chen Q, et al. A double-layered neutral cadmium-organic framework for selective adsorption of cationic organic dyes through electrostatic affinity. *J Solid State Chem* 2020;288:121376. <https://doi.org/10.1016/j.jssc.2020.121376>.
- [143] Khnifira M, Boumya W, Attarki J, Mahsouna A, Abdennouri M, Sadiq M, et al. Elucidating the adsorption mechanisms of anionic dyes on chitosan (110) surface in aqueous medium by quantum chemical and molecular dynamics. *Mater Today Commun* 2022;33. <https://doi.org/10.1016/j.mtcomm.2022.104488>.
- [144] Nie W, Ruan M, Guo D, Liu X. Design of flexible hydrophobic photocatalytic sheets on polydimethylsiloxane substrates based on carrier migration of Si-O-Ti hybrid bonds for photodegradation of dye molecules. *Appl Surf Sci* 2023;616:156415. <https://doi.org/10.1016/j.apsusc.2023.156415>.
- [145] Rojas JC, Bruchey AK, Gonzalez-Lima F. Neurometabolic mechanisms for memory enhancement and neuroprotection of methylene blue. *Prog Neurobiol* 2012;96:32–45. <https://doi.org/10.1016/j.pneurobio.2011.10.007>.
- [146] Nurfatihayati Azis Y, Mutamima A, Herman S, Alfariis CD, Ikrima H. Isotherms studies of equilibrium sorption of Cu<sup>2+</sup> onto hydrochloric acid modified shrimp shell waste. *Mater Today Proc* 2022;63:S496–500. <https://doi.org/10.1016/j.matpr.2022.04.533>.
- [147] Othman NH, Alias NH, Shahruddin MZ, Abu Bakar NF, Nik Him NR, Lau WJ. Adsorption kinetics of methylene blue dyes onto magnetic graphene oxide. *J Environ Chem Eng* 2018;6:2803–11. <https://doi.org/10.1016/j.jece.2018.04.024>.
- [148] Mushahary N, Sarkar A, Das B, Rokhum SL, Basumatary S. A facile and green synthesis of corn cob-based graphene oxide and its modification with corn cob-K<sub>2</sub>CO<sub>3</sub> for efficient removal of methylene blue dye: Adsorption mechanism, isotherm, and kinetic studies. *J Indian Chem Soc* 2024;101:101409. <https://doi.org/10.1016/J.JICS.2024.101409>.
- [149] Amadou Kiari MN, Konan ATS, Sanda Mamane O, Ouattara LY, Ibrahim Grema MH, Siragi Dounounou Boukari M, et al. Adsorption kinetics, thermodynamics, modeling and optimization of bisphenol A on activated carbon based on Hyphaene Thebaica shells. *Case Stud Chem Environ Eng* 2024;10:100903. <https://doi.org/10.1016/J.CSCEE.2024.100903>.
- [150] Hidayat E, Harada H, Mitoma Y, Yonemura S, Halem HIA. Rapid Removal of Acid Red 88 by Zeolite/Chitosan Hydrogel in Aqueous Solution. *Polymers (Basel)* 2022;14. <https://doi.org/10.3390/POLYM14050893>.
- [151] Wei M, Marrakchi F, Yuan C, Cheng X, Jiang D, Zafar FF, et al. Adsorption modeling, thermodynamics, and DFT simulation of tetracycline onto mesoporous and high-surface-area NaOH-activated macroalgae carbon. *J Hazard Mater* 2022;425:127887. <https://doi.org/10.1016/J.JHAZMAT.2021.127887>.
- [152] Geggel Ü, Özcan G., Gürpınar G.C. Removal of Methylene Blue from Aqueous Solution by Activated Carbon Prepared from Pea Shells ( *Pisum sativum* ) 2013; 2013. <https://doi.org/10.1155/2013/614083>.
- [153] Sukmana H., Tomb E. Comparative Study of Adsorption of Methylene Blue and Basic Red 9 Using Rice Husks of Different Origins 2023;1–20.
- [154] Macedo J.D.S., Bezerra N., Almeida L.E., Fragoso E., Cestari A.R., Gimenez I.D.F., et al. Kinetic and calorimetric study of the adsorption of dyes on mesoporous activated carbon prepared from coconut coir dust 2006;298:515–22. <https://doi.org/10.1016/j.jcis.2006.01.021>.
- [155] Waisi BI, Al-Furaiji MH, McCutcheon JR. Activated carbon nanofibers nonwoven flat sheet for methylene blue dye adsorption: batch and flow-through systems. *Desalin Water Treat* 2023;289:228–37. <https://doi.org/10.5004/DWT.2023.29449>.
- [156] Hmamouchi S, Abbud Y, El Yacoubi A, Boulouiz A, Sallek B, El Idrissi BC. Optimization study of methylene blue dye adsorption on *Chamaerops humilis* fibers biosorption using a central composite design. *Desalin Water Treat* 2024;320:100824. <https://doi.org/10.1016/J.DWT.2024.100824>.
- [157] Gebre Meskel A, Kwikima MM, Meshesha BT, Habtu NG, Naik SVCS, Vellanki BP. Malachite green and methylene blue dye removal using modified bagasse fly ash: Adsorption optimization studies. *Environ Challenges* 2024;14:100829. <https://doi.org/10.1016/J.ENVC.2023.100829>.
- [158] Abbou B, Lebkiiri I, Ouaddari H, Kadiri L, Ouass A, Elamri A, et al. Study of the Adsorption Performance of a Cationic Dye onto a Moroccan Clay. *J Chem Heal Risks* 2022;12:563–74. <https://doi.org/10.22034/jchr.2021.1922221.1252>.

- [159] Mantovani D, Quesada HB, Antônio R de S, Cusioli LF, Nishi L, Diório A, et al. Adsorption of methylene blue from effluent using golden mussel (*Limnoperna fortunei*) shell as a low-cost material. *Desalin Water Treat* 2020;188:232–8. <https://doi.org/10.5004/dwt.2020.25245>.
- [160] Marrakchi F, Khanday WA, Asif M, Hameed BH. Cross-linked chitosan/sepiolite composite for the adsorption of methylene blue and reactive orange 16. *Int J Biol Macromol* 2016;93:1231–9. <https://doi.org/10.1016/j.ijbiomac.2016.09.069>.
- [161] Samadi Kazemi M, Sobhani A. CuMn2O4/chitosan micro/nanocomposite: Green synthesis, methylene blue removal, and study of kinetic adsorption, adsorption isotherm experiments, mechanism and adsorbent capacity. *Arab J Chem* 2023;16:104754. <https://doi.org/10.1016/j.arabjc.2023.104754>.
- [162] Auta M, Hameed BH. Chitosan-clay composite as highly effective and low-cost adsorbent for batch and fixed-bed adsorption of methylene blue. *Chem Eng J* 2014;237:352–61. <https://doi.org/10.1016/j.cej.2013.09.066>.
- [163] Ozudogru Yeliz, Tekne Ecem. Adsorption of Methylene Blue from Aqueous Solution Using Spent Coffee/Chitosan Composite. *J Water Chem Technol* 2023; 45:234–45. <https://doi.org/10.3103/s1063455x23030086>.
- [164] Parlayıcı Ş, Pehlivan E. Methylene blue removal using nano-TiO<sub>2</sub>/MWCNT/Chitosan hydrogel composite beads in aqueous medium. *Chemosphere* 2024;365. <https://doi.org/10.1016/j.chemosphere.2024.143244>.